

Dissertation

Genetic Algorithms in Condensed Matter Theory

ausgeführt zum Zwecke der Erlangung des akademischen
Grades eines Doktors der technischen Wissenschaften unter der
Leitung von

Univ.Doiz. Ass.Prof. Dipl.-Ing. Dr.techn. Gerhard Kahl
E136
Institut für Theoretische Physik

eingereicht an der Technischen Universität Wien
Fakultät für Technische Naturwissenschaften und Informatik

von

Dipl.-Ing. Dieter Gottwald
9325732
Murlingengasse 17/418, 1120 Wien

Wien, am 25. Mai 2005

Any sufficiently advanced technology is indistinguishable from magic.
Arthur C. Clarke *Profiles of The Future*

Kurzfassung

In dieser Arbeit wurde ein neuer Ansatz zur Vorhersage von stabilen Kristallstrukturen, die beim Gefrieren auftreten, untersucht. Diese Methode basiert auf der Verwendung von genetischen Algorithmen, die eine Suche nach dem globalen Minimum der freien Energie ermöglichen.

Mit Hilfe dieser Methode war es möglich, das aus der Literatur bekannte Phasendiagramm von neutralen Sternpolymeren zu verbessern und das Phasendiagramm für ionische Mikrogele neu zu berechnen, das ungewöhnliche Kristallstrukturen wie hexagonale und trigonale Gitter enthält. Zusätzlich wurden parallel geschichtete zweidimensionale Gitter, sowie Systeme, die bei hohen Dichten sog. *cluster* bilden, studiert.

Das neue Verfahren erwies sich als effizient und flexibel und könnte mit entsprechenden Modifikationen für eine Vielzahl von ähnlichen Problemen in der Theorie der kondensierten Materie verwendet werden.

Abstract

In this work a new concept to predict equilibrium crystal structures in freezing processes has been introduced. This approach is based on a genetic algorithm that allows an unbiased search through the parameter space of all possible crystal lattices.

It was possible to improve the already published phase diagram of neutral star polymers, and to calculate the phase diagram of ionic microgels that includes unusual structures such as hexagonal and trigonal lattices. Additionally, layers of two-dimensional lattices and system that freeze into clustered crystals were studied.

The new method proved its versatility and power for all cases it was applied to and could be used for numerous similar problems in condensed matter physics.

Contents

Introduction	5
1 Genetic Algorithms	9
1.1 Basic Concepts	10
1.1.1 Individual	11
1.1.2 Initialization	11
1.1.3 Evaluation and Fitness Function	12
1.1.4 Selection	12
1.1.5 Recombination	13
1.1.6 Mutation	14
1.1.7 Schemata and Building Blocks	15
1.2 Comparison to other Optimization Strategies	17
1.2.1 Hill climbing Strategies	17
1.2.2 Random Search	17
1.2.3 Simulated Annealing	18
1.3 Application of the GA to the Freezing Transition	19
1.3.1 Parametrization of Lattices	20
1.3.2 Lattice Unification	24
1.3.3 Fitness Function	27
1.3.4 Hill Climbing Method	27
1.4 Numerical Details	28
1.4.1 Values of the Parameters	28
1.5 Comparison to other Implementations	28
2 Statistical Mechanics	29
2.1 Solid State	29
2.1.1 Lattice Sums	29
2.1.2 Einstein Model	30
2.2 Liquid State	32
2.2.1 Integral Equation Theory	33
2.2.2 Thermodynamic Inconsistency	34
2.2.3 Numerical Algorithms	35
2.2.4 Calculation of the Free Energy	37

2.2.5	Phase Transitions	38
3	Systems	41
3.1	Ionic Microgels	41
3.2	Star Polymers	47
3.3	The Gaussian Core Model and its Generalization	47
4	Results	51
4.1	Freezing	51
4.1.1	Star Polymers	51
4.1.2	Microgels	57
4.2	Layer Transition	73
4.2.1	Layer transition for $\rho\sigma^3 = 0.1$	79
4.2.2	Layer transition for $\rho\sigma^3 = 0.2$	84
4.2.3	Layer transition for $\rho\sigma^3 = 0.5$	88
4.2.4	Summary	92
4.3	Clustering	94
	Conclusions	107
A	Three-Dimensional Bravais Lattices and Crystal Structures	109
A.1	Cubic Lattices	110
A.2	Hexagonal Lattice	111
A.3	Tetragonal Lattices	112
A.4	Trigonal Lattice	113
A.5	Orthorhombic Lattices	114
A.6	Monoclinic Lattices	115
A.7	Triclinic Lattice	116
A.8	Diamond Structure	116
A.9	Hexagonal Close Packed	117
A.10	A15-Structure	117
B	Two-Dimensional Bravais Lattices	119
B.1	Hexagonal Lattice	119
B.2	Square Lattice	119
B.3	Rectangular Lattices	119
B.4	Oblique Lattice	120
C	Lattice Identification	121

Introduction

Changes in the thermodynamic state of a system, like the increase of temperature or pressure, can lead to the transformation of one phase into another. A phase transition occurs when a thermodynamic potential, such as the free energy, or one of its derivatives has a singularity and it is accompanied by a sudden change in some of the properties of the substance. These phase transitions are ubiquitous in everyday life and range from transitions between the vapor, liquid, and solid phases, transitions between the isotropic and nematic phases in liquid crystals, transitions between the ferromagnetic and the paramagnetic phases of magnetic substances, to transitions to a superconducting state below a certain temperature. If one or more of the first derivatives of the thermodynamic potential have a finite discontinuity the transition is called *discontinuous* or *first order transition*. If the first derivatives are continuous and second derivatives are discontinuous or infinite the transition is called *continuous*, *critical*, or *higher order transition*.

The study of phase transitions started in the 1870s with the theories of van der Waals. His model predicted the critical point, which is described by a critical temperature and a critical pressure, on a qualitative level. Below the critical temperature, the transition between the liquid and the vapor phase is discontinuous but above the critical temperature, the liquid phase can be continuously transformed into the vapor phase. At the critical point a critical phase transition occurs.

Nearly all substances arrange themselves in periodic structures upon sufficient cooling. This liquid-solid transition is accompanied by a drastic change in the symmetry properties of the substance. The isotropic liquid with an infinite number of symmetry transformations is replaced by a solid that has only a finite number of symmetry transformations, depending on the crystal lattice. This universal, symmetry breaking phenomenon is a very interesting field of study. In the 1950s it was possible to show that a system of hard spheres freezes into an ordered solid at packing fractions $\eta \gtrsim 0.5$ with the help of computer simulations [1, 2]. This finding suggested that the freezing transition is in general mainly driven by entropy as the free energy of hard spheres is purely entropic. It has become a common belief that a repulsive part in the interaction potential is needed for the stabilization of the solid and attractive forces of sufficient range are required for a liquid-gas transition.

Due to considerable progress during the last years, the thermodynamic properties of crystalline solids can be calculated very accurately. A host of different theories is available for the calculation of the free energy of the solid phase that includes simple lattice sums [3], cell models [4, 5, 6, 7], harmonic solid theories [8, 9], and density functional approaches [10, 11, 12, 13, 14]. Together with the free energy of the liquid, which can be calculated via theories, like integral equation theories or perturbation theories [15, 16], the full liquid-solid phase diagram can be determined on a qualitative level, sometimes even on a quantitative level. However, it still remains an unsolved problem to predict a priori the stable crystal structures of the solid phase by theoretical means. In the conventional approach, a set of possible candidate structures - relying on experience, intuition, or plausible arguments - is selected and the respective free energies are calculated and compared. The structure with the lowest free energy for a given point of state is the stable structure and phase boundaries can be calculated via a double tangent construction.

The choice of these candidates is rather obvious for systems of particles that have a harshly repulsive interaction potential (e.g. atoms) where packing effects play a dominant role. Typically, one takes fcc, bcc, and hcp into account. This preselection process bears the additional risk that further equilibrium crystal structures are not among the candidates and therefore will never appear in the phase diagram. However, if soft matter (see below) is considered, where the interaction potential of the particles diverges weakly near the origin or even remains finite at full overlap of the particles, the crystal structures that these systems can freeze in can be difficult to predict and their phase behavior is much more diversified than expected. For instance, simulations predict stable bcc and diamond structures for a system of neutral star polymers even though the effective interaction is radially symmetric [17]. Even simulations tend to favor crystal structures with cuboidal primitive cells if the simulation box is, as usual, cubic.

The aim of this thesis is the study of an alternate approach to optimize the search for stable crystal structures of a given substance at a certain thermodynamic state. The central tool in this new approach is a genetic algorithm that tries to mimic natural evolutionary processes. Genetic algorithms were developed in the 1970s by J.H. Holland [18] to abstract and explain the adaptive processes of natural systems and to design artificial systems that retain the important mechanisms of natural systems. The theory of genetic algorithms has been steadily improved ever since [19, 20]. While they are used quite frequently in a large variety of different optimization problems, like the traveling salesman problem, or electronic circuit design, their use in physics has been rather limited. They were used to optimize molecular geometry [21, 22], and to optimize laser pulses to control molecules [23]. In this application, genetic algorithms offer the possibility to search the parameter space of all possible crystal structures in an unbiased way and to predict stable crystal structures without having to resort to preselect candidate structures. It turned out that the new approach is an improvement

over the conventional method but still has some shortcomings like the erratic behavior of the algorithm close to phase transitions.

The systems that are investigated in this work belong to the class of *soft matter*. These materials are composed of mesoscopic particles (typical size 1nm–1 μ m) that are dispersed in a solvent whose constituent particles are much smaller in size. These systems are also known under the names *complex fluids* or *colloidal dispersions*. Examples include biological substances like proteins and viruses; industrial products like paints, inks, polishes, cosmetics, detergents, and drilling muds; micelles and vesicles formed of surfactant molecules; and synthetic polymeric particles. These substances are called *soft* because their rigidity against mechanical deformations is many orders of magnitude smaller than that of atomic systems and they can be deformed by humans without the use of tools. Soft matter is of great diversity, for a general overview see [24, 25, 26]. An intriguing property of these substances is the fact that the resolution of modern optic devices is so high that the trajectories of single colloids can be analyzed [27], whereas one had to solely rely on scattering experiments in atomic liquids. Therefore soft matter serves as an ideal model system to study phenomena and theoretical predictions in a detailed way. Another attractive feature of soft matter is that, unlike systems consisting of atoms or small molecules, the interaction between the particles can be easily altered by changing the properties of the solvent (e.g. by adding salt), or by changing the chemical structure of the mesoscopic particles directly (e.g. by using different monomers or side groups for polymer chains, changing the cross-linking density, or changing the length of the polymer chains). Research on these substances has revealed a large number of interesting phenomena, like re-entrant melting, where the liquid freezes upon compression but becomes liquid again upon further compression.

There are two reasons why soft systems were chosen in this work: Firstly, due to their immense richness their phase behavior still holds many secrets while systems with a hard core have already been studied in great detail by theory, simulations, and experiments; and secondly, soft systems can freeze in rather unusual crystal structures [3, 17, 28, 29], which could serve as benchmarks for this new approach.

The genetic algorithm was first used to predict three-dimensional crystal structures of star polymers and ionic microgels and proved its power and versatility by correcting previous results [30, 31]. After this success, it was also applied to study the structure of layered two-dimensional lattices and the formation of clustered crystals.

This thesis is dedicated to show that this new approach is superior to the conventional method and that the world of crystalline soft matter comprises exciting and unexpected phenomena that this work could help to uncover.

This thesis is organized as follows:

- Chapter 1 gives an overview of genetic algorithms and compares them to other optimization strategies like hill climbing, simulated annealing, and random search. Furthermore, the implementation of a genetic algorithm to predict crystal structures is explained.
- Chapter 2 covers the statistical mechanical foundations and the different methods that were used to calculate the thermodynamic properties of the solid and liquid phases of the systems that were considered in this work.
- Chapter 3 specifies the systems that were investigated, namely star polymers, ionic microgels, and the Gaussian core model and its generalization.
- The results are presented in chapter 4: Freezing of star polymers and ionic microgels, the formation of layered structures of polymer solutions, and freezing of clustered crystals in the generalized Gaussian core model are studied.
- The appendix contains information about three- and two-dimensional Bravais lattices and their identification by means of analysis of symmetry properties.

Chapter 1

Genetic Algorithms

After the development of integral and differential calculus by Leibnitz and Newton in the 18th century the problem of finding maxima and minima of functions became solvable for the first time in an analytic way by looking for a zero of the gradient of the function. With this tool at hand the search for the best solution of a problem (*optimization*) could also be solved analytically if the problem had a simple enough structure. The lack of a universal method of optimization for the more complex problems occurring in reality led to the development of an enormous amount of different optimization strategies both driven by advances in mathematics and the increased power of modern computers. These new algorithms included both deterministic methods like *hill climbing*, or the *simplex method*, and heuristic methods like *evolutionary algorithms*, or *simulated annealing*.

Genetic algorithms (GAs) form a subset of evolutionary algorithms and are adaptive, heuristic search algorithms that mimic natural evolution first described by Darwin [32] by including features such as natural selection, survival of the fittest individual, sexual recombination, and mutation. They were introduced by Holland in the 1970s [18] and later improved by Goldberg [19] and Michalewicz [20]. GAs are aiming at the global optimum instead of the next local one and they do not impose any restrictions on the function to be optimized, like continuity, the existence of derivatives, or dimensionality. They are best suited for problems in a large, complex search space where the enumeration of all possible solutions (*random search*) is not possible. An attractive feature of GAs is that the implementation and parallelization is easy and efficient. Another notable difference to other optimization concepts is the fact that GAs do not use the parameters to be optimized themselves but an encoded version of the parameters. They were applied successfully to a tremendous number of different fields that range from molecular structure optimization, protein folding, container loading optimization, game theory, timetabling problems, electronic circuit design, the traveling salesman problem, criminal identification, economics, to forecasting stock market prices and foreign exchange.

1.1 Basic Concepts

Since natural evolution works on the level of chromosomes rather than on the biological entities themselves, a possible solution is represented by an encoded version of the parameters (*genotype*) instead of the value of the parameters (*phenotype*) in a genetic algorithm. This representation is realized as linear string of genes and called *individual*. The prescription that maps the genotype to the corresponding phenotype depends entirely on the structure of the problem and has to be adapted by the user. According to nature one does not use a single individual but a set of them, the *population* $P(t)$. After initialization of the first population a number is assigned to each individual that determines the fitness for survival. Two individuals are chosen with probabilities proportional to the relative position in the current population and mated to produce new individuals. This step is repeated until enough individuals are created to form the next population. These new individuals can be modified again by mutation which occurs with a fixed but small probability. Afterwards this new population is evaluated and subsequent populations are created until a termination condition is met. A canonical genetic algorithm in pseudocode could read:

```
begin
   $t=0$ 
  initialize( $P(t)$ )
  evaluate( $P(t)$ )
  while (not termination-condition) do
     $t=t+1$ 
     $Q(t)=\text{select}(P(t-1))$ 
     $R(t)=\text{recombine}(Q(t))$ 
     $P(t)=\text{mutate}(R(t))$ 
  done
end
```

The average fitness of the population will increase with the number of new populations but it usually reaches a threshold and oscillates around that value (see figure 1.1).

Due to the randomness involved in the creation of each new population genetic algorithms do not belong to the class of convergent algorithms that fulfill the condition

$$\|x_{k+1} - x^*\| \leq C \|x_k - x^*\|^p,$$

where x^* is the exact solution of the problem, x_i the approximate solution in the i -th iteration step, with $C > 0$ and $p > 0$.

For most problems where genetic algorithms are typically applied there are no convergent algorithms available.

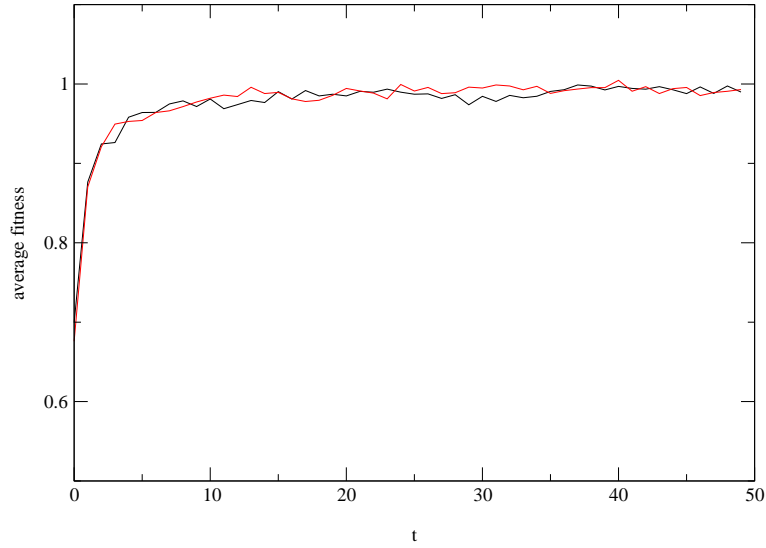


Figure 1.1: *Progression of the average fitness for two typical runs of the GA.*

1.1.1 Individual

The individual \mathcal{I} is a linear string of genes with fixed length l and each of its genes can take values of a certain alphabet $\mathcal{A} = \{a_1, \dots, a_k\}$. The set of binary numbers is the most frequently used alphabet with $\mathcal{A}^{binary} = \{0, 1\}$. In this case the search space consists of 2^l possible solutions. This discrete representation is on the one hand very useful for problems that have discrete variables like combinatorial problems but on the other hand it imposes implicitly lower and upper bounds on continuous variables of the solution.

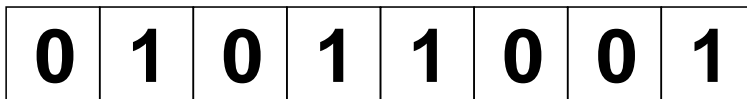


Figure 1.2: *Schematic representation of an individual with length $l = 8$ using the binary alphabet.*

1.1.2 Initialization

The first population is generally chosen at random by assigning each gene in every individual an element of the alphabet \mathcal{A} according to uniformly distributed random numbers.

1.1.3 Evaluation and Fitness Function

In this step a positive number called *fitness number* f is assigned to each individual that describes the quality of the encoded solution. A higher fitness number corresponds to a better and a lower one to a worse solution. To calculate this number, the individual, which is then inserted into a problem specific fitness function $f(\mathcal{I})$, has to be decoded into its phenotype first. The evaluation of the fitness function must be possible for all individuals \mathcal{I} which in turn correspond to all possible solutions in the search space.

The choice of this fitness function is not unique as any function $g(x)$ with $g(x) > 0 \quad \forall x > 0$ and $g(x + \varepsilon) \geq g(x) \quad \forall x > 0, \varepsilon > 0$ leads to another possible fitness function $f'(\mathcal{I}) = g(f(\mathcal{I}))$ that evaluates the individuals of the same problem. The functional form the fitness function determines the *selection pressure* which is defined as the ratio of the selection probability of the best individual to the average selection probability of all individuals; it represents a measure of the preference of good to bad individuals. If the selection pressure is too high, good individuals are highly preferred and propagate very fast, the diversity in the population decreases and the algorithm is very likely to converge to a local optimum. If the selection pressure is too low, good individuals are hardly preferred, bad individuals remain in the population and the GA converges very slowly or not at all; the algorithm degenerates to a random search.

When the solutions have to fulfill certain constraints, it is best to make the construction of the phenotypes in a way that all possible solutions are valid. If this is not possible, individuals that describe solutions that violate these constraints have to be assigned to a low fitness number to suppress their propagation. Experience shows that the number of invalid individuals is typically much higher than the number of valid ones therefore the GA will not converge if the same fitness number (e.g. $f = 0$) is assigned to *all* invalid ones. The decrease of the fitness value has to be linked to the seriousness of the violation of the constraint. One introduces a penalty function $\psi_i(\mathcal{I})$ and an associated weight r_i for each of the n constraints and modifies the fitness function to

$$f'(\mathcal{I}) = f(\mathcal{I}) - \sum_{i=1}^n r_i \psi_i(\mathcal{I}).$$

1.1.4 Selection

In the selection step the parents that will create the next population are selected at random but according to natural selection which states that fitter individuals will produce more offsprings than individuals with lower fitness numbers.

- **Fitness Proportional Selection**

The probability p_i that the i -th individual is chosen in the selection among

a population that consists of n individuals is

$$p_i = \frac{f(\mathcal{I}_i)}{\sum_{j=1}^n f(\mathcal{I}_j)}.$$

- **Rank Selection**

The probability that a given individual is selected does not depend on its fitness value itself but on the rank of the individual compared to other individuals. Two possible implementations of rank selection strategies are linear ranking and tournament selection:

- Linear Ranking

The number of offsprings a_{\max} for the best individual is a fixed number. The individuals in the next population are created in such a way that the number of offsprings for the second best individuals decrease linearly. Thus only the best $\sim 2n/a_{\max}$ individuals act as parents for the next generation.

- Tournament Selection

To select an individual, k individuals are selected at random from the population and the one with the highest fitness value is chosen. The value of k determines the selection pressure. This selection type is best suited for problems where individuals cannot be evaluated independently from the others, e.g. when trying to find a winning strategy for a game.

1.1.5 Recombination

In the recombination step new individuals are created from the parents that were selected in the previous step as follows:

- 1-point crossover

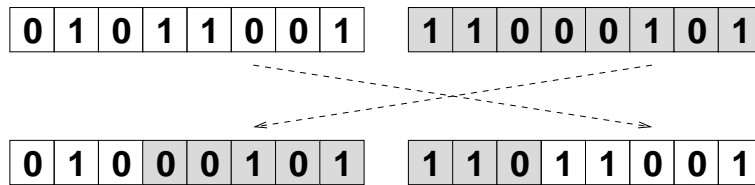


Figure 1.3: *One-point crossover in a typical recombination step.*

The crossover point is chosen randomly and the genes before and after that point are exchanged.

- 2-point crossover

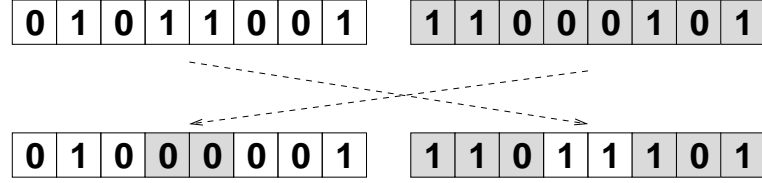


Figure 1.4: *Two-point crossover in a typical recombination step.*

Two points are chosen randomly and the genes between these points are exchanged.

- Uniform crossover

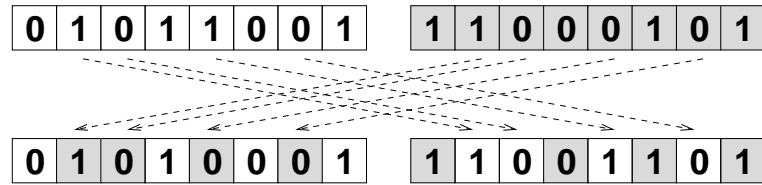


Figure 1.5: *Uniform crossover in a typical recombination step.*

Each gene is separately assigned to a gene of the offsprings at random.

1.1.6 Mutation

Mutation is needed to re-introduce lost genetic material to the population and avoid inbreeding. Mutation should occur rather rarely and at random with a fixed probability, typically $p_{\text{mutate}} \sim 0.001$. If a certain gene is mutated its value is changed to another value in the alphabet \mathcal{A} .

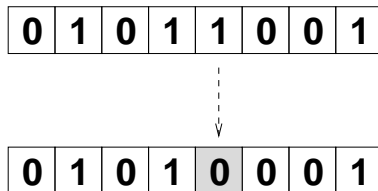


Figure 1.6: *Mutation in a typical mutation step*

1.1.7 Schemata and Building Blocks

A *schema* H is a similarity template describing a subset of individuals with similarities at certain gene positions. The alphabet is expanded by the wildcard character “ \star ”. From now on it is assumed that the population consists of n individuals with length l , which are encoded by using the alphabet of binary numbers. In that case the alphabet \mathcal{A}_+ that is used to describe schemata becomes $\mathcal{A}_+ = \{0, 1, \star\}$. To give an example, the schema $H = \star 001\star$ comprises the individuals 00010, 00011, 10010, and 10011. Each individual of length l is a member of 2^l schemata as the digit in the schema is either the one in the individual or the wildcard \star . Therefore, a population consisting of n individuals contains between 2^l (if all individuals are identical) and $n2^l$ (if all individuals are mutually different) schemata. The *schema order* $o(H)$ is defined as the number of digits unequal “ \star ” in the schema and the *defining length* $\delta(H)$ is the distance between the first and the last digit unequal “ \star ”. Some examples:

$$\begin{aligned} H = \star \star 1 \star 0 \star \star & \quad o(H) = 2 \quad \delta(H) = 2 \\ H = 1 0 \star \star 0 1 0 & \quad o(H) = 5 \quad \delta(H) = 6 \\ H = \star \star \star \star 1 \star \star & \quad o(H) = 1 \quad \delta(H) = 0 \end{aligned}$$

The fitness value of a schema $f(H, t)$ is defined as average fitness value of all individuals in the population $P(t)$ that are elements of H . The frequency of schema H in the population $P(t)$ is denoted by $m(H, P(t))$. Then

$$\begin{aligned} m(H, Q(t+1)) &= m(H, P(t)) n \frac{f(H, t)}{\sum_{i=1}^n f(i)} \\ &= m(H, P(t)) \frac{f(H, t)}{\bar{f}}, \end{aligned} \tag{1.1}$$

where \bar{f} is the average fitness of the population. In the selection step schemata that have a fitness value higher than \bar{f} will propagate while those that have a fitness value lower than \bar{f} will diminish. Assuming that H has the fitness $f(h, t) = \bar{f} + c\bar{f}$, the frequency $m(H, Q(t+1))$ becomes

$$\begin{aligned} m(H, Q(t+1)) &= m(H, P(t)) \frac{\bar{f} + c\bar{f}}{\bar{f}} \\ &= m(H, P(t)) (1 + c). \end{aligned}$$

Under the assumption that \bar{f} is constant

$$m(H, Q(t)) = m(H, P(0)) (1 + c)^t.$$

Therefore the number of schemata with a fitness value above \bar{f} will increase exponentially while the ones with a fitness value below \bar{f} decrease exponentially.

While the individuals are processed in the algorithm more schemata are processed at the same time (*implicit parallelism*). It can be shown that in general $O(n^3)$ schemata are processed in a population consisting of n individuals that use the binary alphabet [18].

The crossover creates both new schemata and destroys some of the old ones. The probability that the crossover point lies in the interval of the defining length and hence the schema is most likely destroyed is given by

$$p_{\text{destroy}} = \frac{\delta(H)}{l-1}$$

with the corresponding survival probability

$$p_{\text{survival}}^{\text{recombination}} \geq 1 - \frac{\delta(H)}{l-1}. \quad (1.2)$$

Inserting equation (1.2) in (1.1) yields

$$m(H, R(t)) \geq m(H, P(t)) \frac{f(H, P(t))}{\bar{f}} \left(1 - \frac{\delta(H)}{l-1}\right). \quad (1.3)$$

A schema is untouched by mutation if no fixed gene is mutated and the probability of survival is

$$p_{\text{survival}}^{\text{mutation}} = (1 - p_m)^{o(H)} \approx 1 - o(H)p_m. \quad (1.4)$$

Above approximation is accurate for very small mutation probabilities p_m . Combining equations (1.3) and (1.4) gives the final frequency of the schema in the new population

$$m(H, P(t+1)) \geq m(H, P(t)) \frac{f(H, P(t))}{\bar{f}} \left(1 - \frac{\delta(H)}{l-1}\right) (1 - o(H)p_m)$$

or approximately,

$$m(H, P(t+1)) \geq m(H, P(t)) \frac{f(H, P(t))}{\bar{f}} \left(1 - \frac{\delta(H)}{l-1} - o(H)p_m\right).$$

This relation leads to the **Schema Theorem**: The frequency of schemata with high fitness, small defining length, and low order increases exponentially in the population. These schemata are called *building blocks*. The genetic algorithm efficiently combines these building blocks to form better individuals from the best partial solutions of the former population. Therefore the arrangement of the genes in the individual is important and the encoding has to be appropriate for the problem.

1.2 Comparison to other Optimization Strategies

1.2.1 Hill climbing Strategies

The basic strategy in *hill climbing* is the intuitive method any wanderer would use to reach the peak of a mountain in a dense fog: always walk uphill. Hill climbing does not necessarily need derivatives of the function to be optimized and constraints can be included quite easily. An overview of different implementations can be found in [33].

The major problem with hill climbing is that the result strongly depends on the starting point of the search. It will work perfectly on functions that have only one optimum as depicted in figure 1.7. When there are more peaks as in figure 1.8 then the algorithm might find the global optimum quite often but is almost completely useless when the objective function is multimodal like the one in figure 1.9.

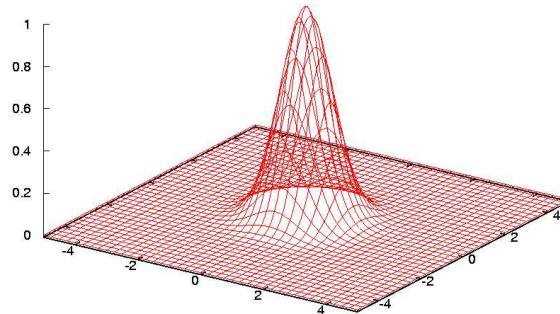


Figure 1.7: *Single-peak function*

1.2.2 Random Search

The enumeration of all possible solutions and the looking for an optimum by comparing them is called *random search*. The order of the solutions is arbitrary, accordingly the position of the global optimum in the search is random. While it guarantees the exact global optimum of the problem, the method is in general too time consuming to be useful for any problems but the most simple ones.

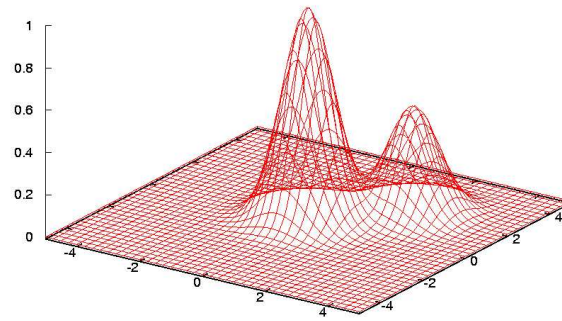


Figure 1.8: *Double-peak function*

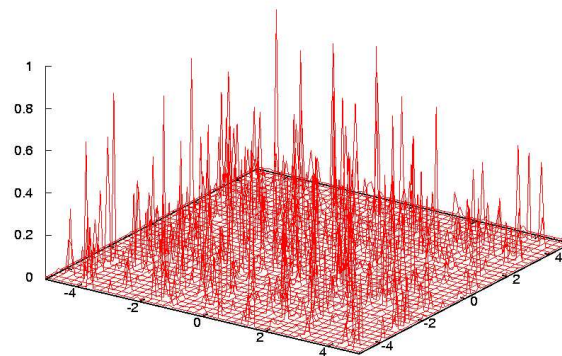


Figure 1.9: *Multimodal function with many peaks*

1.2.3 Simulated Annealing

This optimization technique was not inspired by biology but by metalworking. To harden steel, it is first heated up and then cooled down. Depending on the speed of the temperature reduction, the atoms have more or less time to arrange themselves in a crystal lattice. Fast cooling freezes the atoms in a local minimum of the free energy while slow cooling allows the atoms to reach the positions that correspond to the global minimum of the free energy. This technique is known

as annealing.

Simulated Annealing [34, 35] is based on this concept and Metropolis' Monte-Carlo simulation method. A starting solution $x^{(0,0)}$, temperature $T^{(0)}$, and variation $d^{(0)}$ are chosen. The objective function that will be minimized is denoted by $f(x)$, the actual best solution by x^* , and the actual solution by \tilde{x} which is set to $x^{(0,0)}$ at the beginning. A Monte-Carlo simulation is performed, where new solutions are created by

$$x^{(i,j)} = \tilde{x} + d^{(i)}z,$$

where z is a uniformly distributed random vector for all coordinates of the solution. If $f(x^{(i,j)}) < f(x^*)$ then x^* is set to $x^{(i,j)}$, if $f(x^{(i,j)}) < f(\tilde{x})$ or the random number $r \in [0, 1]$ is smaller than $\exp[(f(x^{(i,j)}) - f(\tilde{x}))/T^{(k)}]$ then \tilde{x} is set to $x^{(i,j)}$ and the algorithm starts by constructing a new possible solution $x^{(i,j+1)}$. If the value of the objective function has not improved within the last N steps then the temperature and possibly the displacement $d^{(i)}$ is decreased until the temperature has reached a pre-defined threshold T_{\min} and the final result of the solution is the current x^* .

While the algorithm itself is quite simple the proper choice of the parameters like the starting temperature, the initial displacement, the number N , the amount of temperature reduction, the displacement decrease, and the upper bound on the temperature T_{\min} are difficult to find. There are some rules for specific objective functions but a general one is not known. Genetic algorithms and simulated annealing share some common properties like the ability to escape local optima but there are some fundamental differences as well. Simulated annealing changes the parameters of the solutions themselves and has only one possible solution. In a GA the genetic representations of the parameters are processed and there is a large number of possible solutions in every population. A more detailed comparison can be found in [36].

1.3 Application of the GA to the Freezing Transition

The conventional approach to the freezing transition would be to choose a set of candidate structures and to calculate the free energy of each of them. The structure with the lowest free energy would be the equilibrium structure.

It is possible to use a GA to determine the crystal structure in which a given substance will freeze. In this approach the lattice is described by the primitive vectors and possibly the positions of additional basis particles of the lattice. These quantities are encoded in the individual and the fitness function is designed in such a way that a lower free energy leads to an increased propagation in the algorithm. The final result of the GA is then refined with a hill climbing algorithm and the crystal structure is identified by the symmetry transformations of the

primitive vectors.

1.3.1 Parametrization of Lattices

1.3.1.1 Three-dimensional Lattices

The three primitive vectors \mathbf{a} , \mathbf{b} , and \mathbf{c} of a three-dimensional lattice can be written as follows

$$\mathbf{a} = a \begin{pmatrix} 1 \\ 0 \\ 0 \end{pmatrix} \quad \mathbf{b} = a \begin{pmatrix} x \cos \varphi \\ x \sin \varphi \\ 0 \end{pmatrix} \quad \mathbf{c} = a \begin{pmatrix} xy \cos \psi \cos \vartheta \\ xy \sin \phi \cos \vartheta \\ xy \sin \vartheta \end{pmatrix} \quad (1.5)$$

where

$$\frac{a}{\sigma} = \left(\frac{n_b n_c}{\rho \sigma^3 x^2 y \sin \varphi \sin \vartheta} \right)^{\frac{1}{3}},$$

σ is a (problem specific) length scale, n_b is the number of basis particles of the crystal structure, n_c the cluster size ($n_c = 1$ for non-clustered lattices), and ρ the bulk number density. The five parameters x , y , ϕ , ψ , and ϑ have to satisfy the constraints

$$\begin{aligned} 0 < x &\leq 1 & 0 < \varphi &\leq \pi/2 \\ 0 < y &\leq 1 & 0 &\leq \psi < \pi \\ & & 0 < \vartheta &\leq \pi/2. \end{aligned} \quad (1.6)$$

Without loss of generality the basis vector of the first particle is

$$\mathbf{B}_1 = \begin{pmatrix} 0 \\ 0 \\ 0 \end{pmatrix}.$$

Basis vectors for possibly additional particles in the basis are represented as linear combinations of the primitive vectors and can be assumed to lie in the primitive cell.

$$\mathbf{B}_i = \alpha_i \mathbf{a} + \beta_i \mathbf{b} + \gamma_i \mathbf{c} \quad i = 2, \dots, n_b$$

with the constraints

$$0 \leq \alpha_i < 1, \quad 0 \leq \beta_i < 1, \quad 0 \leq \gamma_i < 1. \quad (1.7)$$

The total number of parameters n_p required to describe a crystal structure is thus given by $n_p = 5 + 3(n_b - 1) = 2 + 3n_b$. To encode these parameters in an individual the string of genes is divided in n_p parts, three of them with length l_a that encode the parameters φ , ψ , and ϑ and $(3n_b - 1)$ of them with length l_n that encode the remaining parameters. Each of those substrings is the binary representation of an integer number $m_\xi \in [0, \dots, 2^l - 1]$, $\xi \in \{x, y, \varphi, \psi, \vartheta, \alpha_2, \beta_2, \gamma_2, \dots, \alpha_{n_b}, \beta_{n_b}, \gamma_{n_b}\}$.

Once a quantity m_ξ has been evaluated, the corresponding parameter ξ can be determined via

$$\begin{aligned}
x &= \frac{m_x + 1}{2^{l_n}} \\
y &= \frac{m_y + 1}{2^{l_n}} \\
\varphi &= \frac{\pi}{2} \frac{m_\varphi + 1}{2^{l_a}} \\
\psi &= \pi \frac{m_\psi}{2^{l_a}} \\
\vartheta &= \frac{\pi}{2} \frac{m_\vartheta + 1}{2^{l_a}} \\
\alpha_i &= \frac{m_{\alpha_i}}{2^{l_n}} \\
\beta_i &= \frac{m_{\beta_i}}{2^{l_n}} \\
\gamma_i &= \frac{m_{\gamma_i}}{2^{l_n}}.
\end{aligned} \tag{1.8}$$

The parameters ξ obtained with these formulas fulfill the constraints (1.6) and (1.7) automatically.

The parameters l_a and l_n are covered in more detail in section 1.4.

1.3.1.2 Two-dimensional Lattices

The parametrization of two-dimensional lattices can be realized in a fashion similar to the three-dimensional one. The primitive vectors are written as

$$\mathbf{a} = a \begin{pmatrix} 1 \\ 0 \end{pmatrix} \quad \mathbf{b} = a \begin{pmatrix} x \cos \varphi \\ x \sin \varphi \end{pmatrix}$$

where

$$\frac{a}{\sigma} = \left(\frac{n_b}{\eta \sigma^2 x \sin \varphi} \right)^{\frac{1}{2}},$$

σ is a (problem specific) length scale, n_b the number of basis particles, and η the area number density. The vectors of the basis particles are written similar to the procedure in three dimensions:

$$\mathbf{B}_1 = \begin{pmatrix} 0 \\ 0 \end{pmatrix},$$

and

$$\mathbf{B}_i = \alpha_i \mathbf{a} + \beta_i \mathbf{b} \quad i = 2, \dots, n_b.$$

The constraints on the parameters encoded in the individual are analogous to the three-dimensional case.

1.3.1.3 Layered Lattices

A layered lattice consists of n_l layers of identical parallel two-dimensional lattices; their respective origins are shifted: The $(n_l - 1)$ inter-layer vectors \mathbf{c}_i connect the origin of the i -th layer to the one of the $(i + 1)$ -th level. Without loss of generality the two-dimensional lattices are assumed to lie perpendicular to the z -axis. The relation between the volume number density ρ of the system and the area number density η in each layer is

$$\eta = \frac{\rho D}{n_l},$$

where D is the distance between the first and last layer. The 2-d lattice in each layer is parameterized as in section 1.3.1.2. The \mathbf{c}_i introduced above are given by

$$\mathbf{c}_i = \alpha_i \mathbf{a} + \beta_i \mathbf{b} + h_i \begin{pmatrix} 0 \\ 0 \\ 1 \end{pmatrix} \quad i = 1, \dots, n_l - 1$$

where the vectors \mathbf{a} and \mathbf{b} are the primitive vectors of the two-dimensional lattice in each layer with zero z -component and h_i the distance of the i -th to the $(i + 1)$ -th layer. The parameters h_i have to fulfill

$$\begin{aligned} h_i &\geq 0 & i = 1, \dots, n_l - 1 \\ \sum_{i=1}^{n_l-1} h_i &= D. \end{aligned} \tag{1.9}$$

If the parameters h_i are encoded in the individual additional constraints have

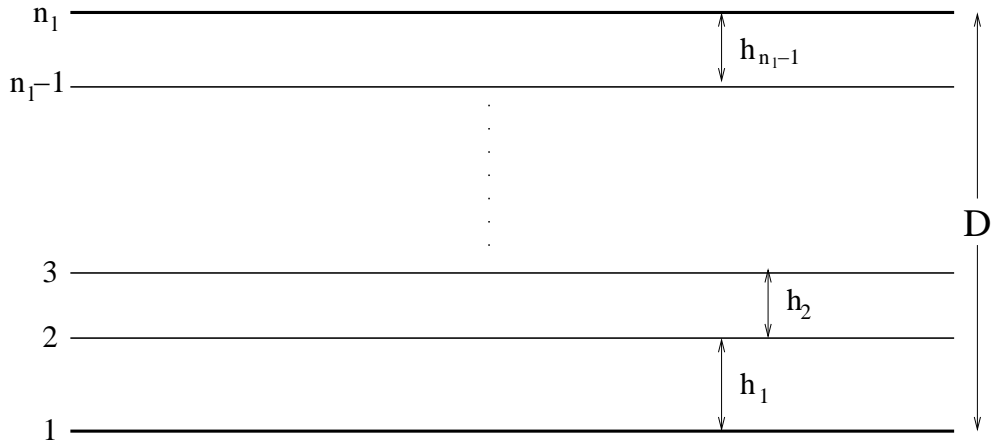


Figure 1.10: *Sketch of a layered lattice*

to be considered during the calculation. To allow a convenient implementation in the GA, the quantities $z_i \in [0, 1)$, $i = 1, \dots, n_l - 2$ are introduced, which can

easily be included in the individual without external constraints. The parameters h_i are then given by

$$\begin{aligned}
h_1 &= z_1 D \\
h_2 &= z_2 (D - h_1) \\
&\vdots \\
h_i &= z_i \left(D - \sum_{j=1}^{i-1} h_j \right) \\
&\vdots \\
h_{n_l} &= D - \sum_{j=1}^{n_l-1} h_j.
\end{aligned}$$

This parametrization, which might seem unnecessarily complicated at first sight, guarantees that the relation (1.9) is automatically satisfied.

The total number of parameters n_p that characterize the particle positions in this system is built up by $2n_b$ parameters for the two-dimensional lattice in the layers, $2(n_l - 1)$ parameters for the x - and y -components of the inter-layer vectors \mathbf{c}_i , and $n_l - 2$ parameters for their z -component. They are encoded in an individual in a similar fashion as described for the three-dimensional case.

1.3.1.4 Additional Parameters

It is possible to encode additional parameters of the system under consideration in the individual if they have to be optimized together with the lattice structure. In this work, the cluster size n_c of clustered crystals (see section 4.3) and the localization parameter α in the Einstein model (see section 2.1.2) were incorporated into the calculations.

- **Cluster Size**

A substring with length l_c is added to the individual that defines an integer number m_{n_c} . The cluster size n_c is then given by

$$n_c = 1 + \frac{m_{n_c}}{2^{l_{cp}}}.$$

The parameter $l_{cp} < l_c$ defines the resolution of n_c which lies in the interval $[1, (2^{l_c} + 2^{l_{cp}} - 1)/2^{l_{cp}}]$.

- **Localization Parameter**

A substring with length l_α is added to the individual that encodes the integer number m_α . The localization parameter α can be calculated via

$$\alpha = \alpha_{\min} + m_\alpha \alpha_{\text{inc}}.$$

The parameter α_{\min} ensures a lower limit for α because a crystal with $\alpha \lesssim 30$ can hardly be considered a solid. The parameter $\alpha_{\text{inc}} > 1$ is used to have a higher upper bound on the value of α without the need to increase the length of the substring.

The values of the parameters l_c , l_{cp} , α_{\min} , and α_{inc} that were chosen for the calculations in this work are detailed in section 1.4.

1.3.2 Lattice Unification

The choice of the primitive vectors for a given lattice is not unique and this fact poses a serious problem for any optimization method due to the infinite number of different primitive vectors that describe exactly the same lattice. On top of that, there is an additional ambiguity in the choice of the basis vectors if the number of basis particles is greater than one.

To ensure the use of a uniquely defined set of primitive vectors and basis vectors for every crystal structure, the following strategy was utilized when decoding the information contained in the individual:

- Decode the primitive vectors and basis vectors from the individual.
- Modify the primitive vectors.
- Rotate the primitive and basis vectors to have the form as in equation (1.5).
- Modify the basis vectors.
- Calculate the projection of the vectors in the discrete space imposed by the binary accuracy.
- Re-encode the primitive and basis vectors in the individual.
- Calculate the fitness value of the new lattice.

These steps are described in the following paragraphs where on the assumption that a three-dimensional lattice is considered. For the other two cases discussed above the algorithm follows similar lines.

1.3.2.1 Unified description of the lattice

The primitive vectors were chosen in such a way as to minimize the surface of the cell spanned by the three vectors. To that end the following iterative algorithm was applied: Starting with three primitive vectors $(\mathbf{a}^*, \mathbf{b}^*, \mathbf{c}^*)$, the quantity

$$\Sigma^* = |\mathbf{a}^* \times \mathbf{b}^*| + |\mathbf{a}^* \times \mathbf{c}^*| + |\mathbf{b}^* \times \mathbf{c}^*|$$

which represents half of the surface of the primitive cell is evaluated. Then the corresponding Σ^* -value of the primitive cells spanned by the following twelve linear combinations of the primitive vectors are calculated:

$$\begin{array}{ll} (\mathbf{a}^* \pm \mathbf{b}^*, \mathbf{b}^*, \mathbf{c}^*) & (\mathbf{a}^* \pm \mathbf{c}^*, \mathbf{b}^*, \mathbf{c}^*) \\ (\mathbf{a}^*, \mathbf{b}^* \pm \mathbf{c}^*, \mathbf{c}^*) & (\mathbf{a}^*, \mathbf{b}^* \pm \mathbf{a}^*, \mathbf{c}^*) \\ (\mathbf{a}^*, \mathbf{b}^*, \mathbf{c}^* \pm \mathbf{a}^*) & (\mathbf{a}^*, \mathbf{c}^*, \mathbf{c}^* \pm \mathbf{b}^*). \end{array}$$

and the smallest of these values is denoted by $\tilde{\Sigma}$. If $\tilde{\Sigma}$ is smaller than Σ^* the corresponding combination represents the new primitive vectors and the algorithm starts again. If $\tilde{\Sigma}$ is greater than Σ^* the algorithm is finished.

1.3.2.2 Rotation of the Vectors

The three primitive vectors are ordered by their magnitude so that \mathbf{a} is the longest, \mathbf{b} the second-longest, and \mathbf{c} the shortest vector. Then the vectors are rotated so that \mathbf{a} is parallel to the x -axis and \mathbf{b} lies in the x - y -plane. Via additional inversion of the vectors and/or coordinate axes one arrives at the representation (1.5) that fulfills the constraints (1.6).

1.3.2.3 Modification of the Basis Vectors

The lattice remains invariant under the following transformations of the basis vectors $\{\mathbf{B}_i\}$: Firstly, the set $\{\mathbf{B}_i + \mathbf{v}_{jklm}\}$ with

$$\mathbf{v}_{jklm} = -\mathbf{B}_j + k\mathbf{a} + l\mathbf{b} + m\mathbf{c}, \quad j = 1, \dots, n_b \quad k, l, m \in \mathbb{Z}$$

describes the same lattice. Secondly, the indices of the basis vectors $\{\mathbf{B}_i\}$ can be permuted without changing the lattice.

To arrive at a uniquely defined set of basis vectors these ambiguities have to be removed by imposing certain constraints on the basis vectors. In this work the following algorithm was used:

1. Create the sets $\{\tilde{\mathbf{B}}_i^{(j)}\} = \{\mathbf{B}_i - \mathbf{B}_j\}$, $j = 1, \dots, n_b$.
2. Solve the equations

$$\bar{\alpha}_i^{(j)} \mathbf{a} + \bar{\beta}_i^{(j)} \mathbf{b} + \bar{\gamma}_i^{(j)} \mathbf{c} = \tilde{\mathbf{B}}_i^{(j)}$$

3. Calculate

$$\begin{aligned} \alpha_i^{(j)} &= \bar{\alpha}_i^{(j)} - [\bar{\alpha}_i^{(j)}] \\ \beta_i^{(j)} &= \bar{\beta}_i^{(j)} - [\bar{\beta}_i^{(j)}] \\ \gamma_i^{(j)} &= \bar{\gamma}_i^{(j)} - [\bar{\gamma}_i^{(j)}], \end{aligned}$$

where $[x]$ denotes the largest integer smaller or equal x . The resulting values of $\alpha_i^{(j)}$, $\beta_i^{(j)}$, and $\gamma_i^{(j)}$ lie in the interval $[0, 1)$.

4. Calculate $\Upsilon^{(j)}$ via

$$\Upsilon^{(j)} = \sum_{i=1}^{n_b} (\alpha_i^{(j)} + \beta_i^{(j)} + \gamma_i^{(j)})$$

and find $\Upsilon^{(j^*)} = \min\{\Upsilon^{(j)}\}$.

5. Sort in ascending order by $\alpha_i^{(j^*)}$, then by $\beta_i^{(j^*)}$, and then by $\gamma_i^{(j^*)}$. This ensures that the vector $(0, 0, 0)$ will always be first.

6. Calculate the uniquely defined set of basis vectors via

$$\mathbf{B}_i = \alpha_i^{(j^*)} \mathbf{a} + \beta_i^{(j^*)} \mathbf{b} + \gamma_i^{(j^*)} \mathbf{c}, \quad i = 1, \dots, n_b.$$

1.3.2.4 Projection into the Search Space

The binary representation of the vectors in the individual creates a discrete search space. In general, the vectors $\mathbf{a}, \mathbf{b}, \mathbf{c}, \{\mathbf{B}_i\}$ that have been obtained by the modifications outlined above are not an element of that space. The primitive vectors and the basis vectors have to be projected to the appropriate element of the search space so that the vectors can be stored in the individual.

First the parameters $x, y, \varphi, \psi, \vartheta$ are calculated from the primitive vectors:

$$\begin{aligned} x &= \frac{b}{a} \\ y &= \frac{b}{c} \\ \varphi &= \arctan \frac{b_y}{b_x} \\ \psi &= \arctan \frac{c_y}{c_x} \\ \vartheta &= \arctan \frac{c_z \sin \psi}{c_y}, \end{aligned}$$

where v denotes the magnitude of the vector \mathbf{v} and v_ξ , $\xi \in \{x, y, z\}$, is the ξ -component of the vector \mathbf{v} . Then the corresponding integer number m_c is computed by inverting the appropriate equation in (1.8) and rounding to the nearest integer. The binary representation of these numbers is then stored in the individual.

The basis vectors also have to be transformed and to that end the primitive vectors \mathbf{a}', \mathbf{b}' , and \mathbf{c}' that are now encoded in the individual are calculated first. The parameters α_i, β_i , and γ_i are obtained by solving the equations

$$\alpha_i \mathbf{a}' + \beta_i \mathbf{b}' + \gamma_i \mathbf{c}' = \mathbf{B}_i \quad i = 2, \dots, n_b.$$

Again, the appropriate relations (1.8) are inverted and the numbers $m_{\alpha_2}, \dots, m_{\gamma_{n_b}}$ are obtained as outlined above and their binary representation is stored in the individual.

1.3.3 Fitness Function

To find the crystal structure with the lowest free energy F , solutions with a low free energy have to be preferred over ones with a higher free energy. Therefore the positive definite fitness function should increase with decreasing free energy. In addition it has to be taken into account that the free energy can take both positive and negative values. The following two forms for the fitness functions were used for the calculations in this thesis. The first one reads

$$f(\mathcal{I}) = \exp \left(1 - \frac{F(\mathcal{I})}{F_{\text{fcc}}} \right) \quad (1.10)$$

and the second one

$$f(\mathcal{I}) = \exp \left(1 - \left(\frac{F(\mathcal{I})}{F_{\text{fcc}}} \right)^{g(i)} \right), \quad (1.11)$$

where $F(\mathcal{I})$ is the free energy for the crystal structure that is described by the individual \mathcal{I} , F_{fcc} is the free energy of a fcc structure, and $g(i)$ a scalar function that depends on the number of the population i in the algorithm. The different concepts to calculate the free energy are detailed in section 2.1.

1.3.4 Hill Climbing Method

During the run of the genetic algorithm the individual \mathcal{I}^* that encodes the crystal structure with the lowest free energy is saved. As a consequence of the limited accuracy due to the binary representation of the parameters with a finite number of digits this solution is refined with a hill climbing algorithm. The n_p parameters $x, y, \varphi, \psi, \vartheta, \alpha_2, \dots, \gamma_{n_b}$ are decoded from the individual \mathcal{I}^* and define the starting point of the search, the n_p -dimensional vector \mathbf{q}

$$\mathbf{q} = (x, y, \varphi, \psi, \vartheta, \alpha_2, \dots, \gamma_{n_b}).$$

The initial step size δ is set to

$$\delta = \left(\frac{1}{2} \right)^{\min\{l_n, l_a\}}.$$

The vector \mathbf{e}_ξ , $\xi \in \{x, y, \varphi, \psi, \vartheta, \alpha_2, \dots, \gamma_{n_b}\}$ represents the unit vector in ξ -direction. Then $F(\mathbf{q})$, the free energy of the crystal structure that corresponds to the parameters in \mathbf{q} , is calculated. The free energy of the vectors $\mathbf{q}_i \in \{\mathbf{q} \pm \delta \mathbf{e}_\xi\}$ is computed and if the free energy $F(\mathbf{q}^*) = \min\{F(\mathbf{q}_i)\}$ is lower than $F(\mathbf{q})$ then \mathbf{q} is set to \mathbf{q}^* . If not, then δ is decreased, typically $\delta \rightarrow \delta/3$. Once δ is lower than some threshold δ_{thresh} then the algorithm is terminated and the final crystal structure is calculated from \mathbf{q}^* . The typical number of steps required for a lattice with one basis particle is ~ 150 .

1.4 Numerical Details

1.4.1 Values of the Parameters

Most of the calculations in this thesis were carried out with the following values for the parameters

Parameter	Value
l_n	12
l_a	6
l_c	8
l_{cp}	3
α_{\min}	30
α_{inc}	5
l_α	10
p_{mutate}	0.005
number of individuals n	1000
maximum number of new populations	100
δ_{thresh}	1×10^{-10}

1.5 Comparison to other Implementations

Evolutionary algorithms have been used before to calculate the equilibrium configuration of molecular clusters [21, 22]. Even though the method used there is called “genetic algorithm” this terminology is not correct as the parameters themselves were optimized and not their genetically encoded version.

In this contribution, a possible solution was characterized by its coordinates and it was assigned to a fitness value. As in the GA, parents were selected and offsprings were produced that formed the next generation of solutions. However, in this implementation the algorithm that creates a child from the parents did not happen on the genetic level but on a geometric level. A plane was selected at random that separated each parent and the two parts were cross-combined. Then the cluster was possibly mutated by displacing the particles in the cluster in a random fashion.

Chapter 2

Statistical Mechanics

To calculate the fitness function for all possible candidate structures one must be able to compute the free energy of crystal structures. In this work two approximations were used: lattice sums and the Einstein model which are described in section 2.1.

The calculation of the free energy of the liquid state which is important to determine the complete phase diagram is covered in section 2.2.

2.1 Solid State

2.1.1 Lattice Sums

The lattice sum L of a crystal structure gives the exact free energy at zero temperature and neglects the influence of entropy on the free energy. The free energy per particle F/N (which is now identical with the internal energy) for simple lattices, i.e. lattice with just one basis particle, is

$$\frac{F_{\text{latticesum}}}{N} = \frac{1}{2} \sum'_{\{\mathbf{R}_i\}} \Phi(R_i) \quad (2.1)$$

where the set $\{\mathbf{R}_i\}$ consists of all lattice positions and $\Phi(r)$ is the pair potential between the particles of the lattice and the prime denotes the omission of the $(0, 0, 0)$ -term. If the three primitive vectors \mathbf{a} , \mathbf{b} , and \mathbf{c} of the lattice are known F/N can be written as

$$\frac{F_{\text{latticesum}}}{N} = \frac{1}{2} \sum'_{ijk} \Phi(|i\mathbf{a} + j\mathbf{b} + k\mathbf{c}|) = \frac{1}{2} \sum'_{ijk} \Phi(|\mathbf{v}_{ijk}|).$$

If the lattice has a basis, then not all points in the lattice are indistinguishable. Therefore the lattice sum has to be averaged over the positions of the basis

particles. The final result is

$$\frac{F_{\text{latticesum}}}{N} = \frac{1}{2} \sum'_{ijk} \Phi(|\mathbf{v}_{ijk}|) + \frac{1}{n_b} \sum_{ijk} \sum_{l>m} \Phi(|\mathbf{v}_{ijk} + \mathbf{B}_m - \mathbf{B}_l|). \quad (2.2)$$

Note that the $(0, 0, 0)$ -term is included in the second summation.

2.1.2 Einstein Model

The Gibbs-Bogoliubov inequality [15]

$$F \leq F_0 + \langle \mathcal{H} - \mathcal{H}_0 \rangle_0 \quad (2.3)$$

relates the free energy F of a system with the Hamiltonian \mathcal{H} to the free energy F_0 of a reference system with the Hamiltonian \mathcal{H}_0 . The expression $\langle \cdot \rangle_0$ denotes an ensemble average in the reference system. If the reference system is “close enough” to the system under consideration, both F_0 and the ensemble average $\langle \mathcal{H} - \mathcal{H}_0 \rangle_0$ can be calculated easily. If the Hamiltonian \mathcal{H}_0 has one or more variational parameters then the r.h.s. of equation (2.3) can be minimized with respect to these parameters to obtain an upper bound of the free energy of the system of interest that can be used as an approximation for the same.

In the Einstein model each particle at position \mathbf{r}_i is assumed to be attached to a lattice site \mathbf{R}_i by a spring with spring constant k . The Hamiltonian of the reference system is then

$$\mathcal{H}_0 = \sum_{i=1}^N \left(\frac{\mathbf{p}_i^2}{2m} + \frac{k}{2} (\mathbf{r}_i - \mathbf{R}_i)^2 \right), \quad (2.4)$$

where N is the number of particles, m the mass of each particle, and \mathbf{p}_i the momentum of particle i . The parameter k will be used as the variational parameter. The Hamiltonian \mathcal{H} of the system under consideration is given by

$$\mathcal{H} = \sum_{i=1}^N \frac{\mathbf{p}_i^2}{2m} + \frac{1}{2} \sum_{i \neq j}^N \Phi(|\mathbf{r}_i - \mathbf{r}_j|). \quad (2.5)$$

The kinetic contributions to the ensemble average in equation (2.3) cancel and this relation becomes

$$F \leq F_0 + \langle V \rangle_0 - \langle V_0 \rangle_0.$$

To calculate the free energy of the reference system, the partition function

$$Q_N^0 = \frac{1}{h^{3N}} \int d\mathbf{r}^N \int d\mathbf{p}^N e^{-\beta \mathcal{H}_0(\mathbf{r}, \mathbf{p})} \quad (2.6)$$

is evaluated first. Note that the usual pre-factor $1/N!$ is missing since the particles are distinguishable by the lattice site they are attached to. Due to the functional

form of \mathcal{H}_0 , all the integrals in (2.6) are Gaussian which can be solved analytically to yield

$$Q_N^0 = \left(\frac{\Lambda}{\sigma}\right)^{-3N} \left(\frac{\alpha}{\pi}\right)^{-3N/2},$$

where $\alpha = \beta k \sigma^2 / 2$ is the dimensionless spring constant, σ a length scale, and $\Lambda = \sqrt{2\pi\beta\hbar^2/m}$ the thermal de Broglie wavelength.

The free energy F_0 is then given by

$$F_0 = -k_B T \log Q_N^0 = 3Nk_B T \log \left(\frac{\Lambda}{\sigma}\right) + \frac{3}{2}Nk_B T \log \left(\frac{\alpha}{\pi}\right). \quad (2.7)$$

As a consequence of the equipartition theorem the internal energy $\langle V_0 \rangle_0$ is given by

$$\langle V_0 \rangle_0 = 3Nk_B T / 2. \quad (2.8)$$

The ensemble average in the reference system of the potential energy of the system, $\langle V \rangle_0$, can be obtained via

$$\langle V \rangle_0 = \frac{1}{2} \int d\mathbf{r}' \int d\mathbf{r}'' \Phi(|\mathbf{r}' - \mathbf{r}''|) \rho_0^{(2)}(\mathbf{r}', \mathbf{r}''; \{\mathbf{R}_i\}) \quad (2.9)$$

with the two-particle density $\rho_0^{(2)}(\mathbf{r}', \mathbf{r}''; \{\mathbf{R}_i\})$. The one-particle density is proportional to the Boltzmann factor of the harmonic potential:

$$\rho_0^{(1)}(\mathbf{r}; \{\mathbf{R}_i\}) = \left(\frac{\alpha}{\pi}\right)^{\frac{3}{2}} \sum_{\{\mathbf{R}_i\}} e^{-\alpha(\mathbf{r}-\mathbf{R}_i)^2} \quad (2.10)$$

and the two-particle density can then be approximated by

$$\rho_0^{(2)}(\mathbf{r}', \mathbf{r}''; \{\mathbf{R}_i\}) = \rho_0^{(1)}(\mathbf{r}'; \{\mathbf{R}_i\}) \rho_0^{(1)}(\mathbf{r}''; \{\mathbf{R}_i\}).$$

Inserting this expression in the integral (2.9) yields

$$\begin{aligned} \langle V \rangle_0 = & \frac{N}{2} \sqrt{\frac{\alpha}{2\pi}} \left[2\alpha \int_0^\infty dx x^2 e^{-\frac{\alpha}{2}x^2} \Phi(x) + \right. \\ & \left. \sum_{\{\mathbf{R}_i\}}' \frac{1}{R_i} \int_0^\infty dx x \Phi(x) \left(e^{-\frac{\alpha}{2}(x-R_i)^2} - e^{-\frac{\alpha}{2}(x+R_i)^2} \right) \right] \end{aligned}$$

which can be rewritten as

$$\frac{\beta \langle V \rangle_0}{N} = \beta \Phi_E(0; \alpha) + \frac{1}{2} \sum_{\{\mathbf{R}_i\}}' \beta \Phi_E(R_i; \alpha) \quad (2.11)$$

which is equivalent to the lattice sum with the Einstein potential $\Phi_E(r; \alpha)$

$$\Phi_E(r; \alpha) = \begin{cases} \sqrt{\frac{\alpha^3}{2\pi}} \int_0^\infty dx x^2 e^{-\frac{\alpha}{2}x^2} \Phi(x) & r = 0 \\ \sqrt{\frac{\alpha}{2\pi}} \frac{1}{r} \int_0^\infty dx x \Phi(x) \left(e^{-\frac{\alpha}{2}(x-r)^2} - e^{-\frac{\alpha}{2}(x+r)^2} \right) & r > 0 \end{cases}$$

When crystals with single site occupancy are considered, the first term in equation (2.11) is neglected because it corresponds to the potential energy of the particle at the origin. If clustered crystals are considered, the average of the potential energy becomes

$$\frac{\beta \langle V \rangle_0}{N} = (n_c - 1) \beta \Phi_E(0; \alpha) + \frac{n_c}{2} \sum'_{\{\mathbf{R}_i\}} \beta \Phi_E(R_i; \alpha), \quad (2.12)$$

with the cluster size n_c which reduces to the correct expression for $n_c = 1$.

Inserting equations (2.11), (2.8), and (2.7) into the Gibbs-Bogoliubov inequality yields (for $n_c = 1$)

$$\frac{\beta F}{N} \leq 3 \log \left(\frac{\Lambda}{\sigma} \right) + \frac{3}{2} \log \left(\frac{\alpha}{\pi} \right) - \frac{3}{2} + \frac{1}{2} \sum'_{\{\mathbf{R}_i\}} \beta \Phi_E(R_i; \alpha). \quad (2.13)$$

To allow comparison to other free energy values calculated with different theories the first term is, as usual, dropped in practice because it is possible to choose the mass so that $\log(\Lambda/\sigma)$ vanishes. To minimize the remaining terms of equation (2.13) the contribution proportional to $\log \alpha$ favors $\alpha \rightarrow 0$ while the last one favors $\alpha \rightarrow \infty$. The interplay of these two terms can lead to a local minimum at $\alpha > 0$. The free energy of the solid according to the Einstein model is then

$$\frac{\beta F_{\text{einstein}}}{N} = \min_{\alpha} \left(\frac{3}{2} \log \left(\frac{\alpha}{\pi} \right) - \frac{3}{2} + \frac{1}{2} \sum'_{\{\mathbf{R}_i\}} \beta \Phi_E(R_i; \alpha) \right). \quad (2.14)$$

It can be shown that the Einstein model is equivalent to a density-functional theory where a mean-field form for the functional for the excess free energy and a Gaussian shaped one-particle density is used [37].

2.2 Liquid State

The thermodynamic properties of a liquid in equilibrium are described by the *total correlation function* $h(r)$ and the *direct correlation function* $c(r)$. These two functions are related via the Ornstein-Zernike (OZ) equation [15] which reads for a spatially homogeneous and isotropic liquid

$$h(r) = c(r) + \rho \int d\mathbf{r}' c(|\mathbf{r} - \mathbf{r}'|) h(r'), \quad (2.15)$$

where the number density is denoted by ρ . The OZ equation can formally be solved for $h(r)$ by repeatedly inserting it into itself

$$h(r) = c(r) + \rho \int d\mathbf{r}' c(|\mathbf{r} - \mathbf{r}'|) c(r') + \rho^2 \int d\mathbf{r}'' \int d\mathbf{r}' c(|\mathbf{r} - \mathbf{r}'|) c(|\mathbf{r}' - \mathbf{r}''|) c(r'') + \dots$$

This equation can be interpreted in the following way: The total correlation between two particles is equal to the sum of the direct correlation plus the indirect correlation mediated by an increasing number of other particles.

The Fourier transform of the OZ equation becomes the algebraic equation

$$\tilde{h}(k) = \tilde{c}(k) + \rho \tilde{h}(k) \tilde{c}(k) \quad (2.16)$$

and the Fourier transformed correlation functions which are denoted by the tilde, are related to the static structure factor $S(k)$ through

$$S(k) = 1 + \rho \tilde{h}(k) = \frac{1}{1 - \rho \tilde{c}(k)}.$$

The static structure factor can be measured by scattering experiments and represents a very important link to compare theory and experiments.

The total correlation function is related to the *radial distribution function* $g(r)$ that is defined for a homogeneous system as

$$g(\mathbf{r}) = \frac{1}{4\pi r^2 \rho N} \left\langle \sum_{i \neq j} \delta(\mathbf{r} - \mathbf{r}_{ij}) \right\rangle$$

via

$$h(r) = g(r) - 1.$$

2.2.1 Integral Equation Theory

In general $h(r)$ and $c(r)$ are not known and the OZ equation alone is not sufficient for determining both correlation functions. Another relation between $h(r)$, $c(r)$, and the potential $\Phi(r)$ is required. Such a relation, $F[c, h, \Phi; r] = 0$, is called *closure relation*. The knowledge of the exact closure relation is equivalent to knowing the partition function of the system which is only possible for simple systems like the ideal gas. Various levels of simplification can be used to derive closures from exact results of statistical mechanics.

In this work three closures were used to calculate the thermodynamic properties of the liquid state: the *mean spherical approximation* (MSA), the *hypernetted chain approximation* (HNC), and the *Rogers-Young closure* (RY) [38].

- **MSA Closure:** The closure reads

$$\begin{aligned} g(r) &= 0 & r < \sigma \\ c(r) &= -\beta \Phi(r) & r \geq \sigma, \end{aligned} \quad (2.17)$$

for a hard core system with hard core diameter σ . If there is no hard core then the MSA closure becomes

$$c(r) = -\beta\Phi(r) \quad \forall r. \quad (2.18)$$

In that case $c(r)$ is explicitly known and $h(r)$ can be calculated by Fourier transforming $c(r)$ to $\tilde{c}(k)$, inserting it in equation (2.16) and transforming $\tilde{h}(k)$ back to $h(r)$.

- **HNC Closure:** The HNC closure has the form

$$h(r) = e^{-\beta\Phi(r)+h(r)-c(r)} - 1. \quad (2.19)$$

- **PY Closure:** The Percus-Yevick closure (PY) reads

$$c(r) = (e^{-\beta\Phi(r)} - 1) (h(r) - c(r) + 1).$$

- **RY Closure:** The RY closure interpolates between the PY closure relation and the HNC closure to achieve thermodynamic consistency between two thermodynamic routes (see below). The functional form of this closure reads

$$c(r) = e^{-\beta\Phi(r)} \left(1 + \frac{e^{(h(r)-c(r))f(r)} - 1}{f(r)} \right) - h(r) + c(r) - 1 \quad (2.20)$$

and the mixing function $f(r)$ is usually chosen to be

$$f(r) = 1 - e^{-\alpha r} \quad \alpha \in [0, \infty).$$

In the limit $\alpha \rightarrow \infty$ the RY closure becomes the HNC closure and in the limit $\alpha \rightarrow 0$ the PY closure is obtained. Independently of α the RY closure shows PY-like behavior for small distances and HNC-like behavior for large distances. The mixing parameter is chosen so that the compressibility calculated via two different thermodynamic routes coincide (for more details see sections 2.2.2 and 2.2.3).

2.2.2 Thermodynamic Inconsistency

The thermodynamic properties of the fluid can be calculated from the correlation functions via three different routes: the virial, the compressibility, and the energy route. If the exact correlation functions were known, the results of all three routes would coincide. If the correlation functions are obtained with closure relations that contain approximations, then the results differ. This phenomenon is known as *thermodynamic inconsistency*.

From statistical mechanics one can derive the following three equations of state:

- **Virial Route:** The pressure P^v can be calculated with the virial equation

$$\frac{\beta P^v}{\rho} = 1 - \frac{2\pi}{3}\rho \int_0^\infty dr r^3 g(r) \frac{d\beta\Phi(r)}{dr}.$$

- **Energy Route:** A thermodynamic quantity can be considered the sum of an ideal part (“id”) that corresponds to the thermodynamic property of an ideal system which can be calculated analytically, and an excess part (“ex”) that stems from the pair interactions and usually has to be calculated numerically. The excess internal energy U^{ex} is obtained from the energy equation

$$\frac{U^{\text{ex}}}{N} = 2\pi\rho \int_0^\infty dr r^2 g(r) \Phi(r).$$

The excess free energy F^{ex} can then be calculated with

$$\frac{\beta F^{\text{ex}}}{N} = \int_0^\beta d\beta' U^{\text{ex}}(\beta').$$

From this expression the excess pressure is obtained via

$$P^{e,\text{ex}} = - \left(\frac{\partial F^{\text{ex}}}{\partial V} \right)_T.$$

- **Compressibility Route:** The isothermal compressibility κ_T can be calculated by the compressibility equation

$$\rho k_B T \kappa_T = 1 + \rho \int d\mathbf{r} (g(r) - 1) = 1 + \rho \tilde{h}(k=0)$$

where

$$\kappa_T = -\frac{1}{V} \left(\frac{dV}{dP^c} \right)_T$$

is the isothermal compressibility. Integration of this relation with respect to the volume leads to the pressure P^c .

2.2.3 Numerical Algorithms

2.2.3.1 Broyles’ Algorithm

There are several algorithms that are used to solve the OZ equation along with a closure relation for the correlation functions. In this work the *Broyles’ algorithm* was used [39].

Instead of the pair of correlation functions $c(r)$ and $h(r)$ rather $c(r)$ and the indirect correlation function $\gamma(r) = h(r) - c(r)$ are used in this algorithm. The Fourier transform of the OZ equation reads in terms of those functions

$$\tilde{\gamma}(k) = \frac{\rho \tilde{c}^2(k)}{1 - \rho \tilde{c}(k)} \quad (2.21)$$

and the closure relation is solved for $c(r)$:

$$c(r) = G[\gamma(r), \Phi(r)]. \quad (2.22)$$

The iterative algorithm works as follows:

1. Set the iteration index i to 0 and make an initial guess for $c^{(i)}(r)$. Usually, either a previous solution for $c(r)$ or the MSA expression is used.
2. Fourier transform $c^{(i)}(r)$ to obtain $\tilde{c}^{(i)}(k)$.
3. Use equation (2.21) to obtain $\tilde{\gamma}^{(i)}(k)$.
4. Make an inverse Fourier transform to obtain $\gamma^{(i)}(r)$.
5. Use equation (2.22) to obtain $c^{(i+\frac{1}{2})}(r)$.
6. Obtain $c^{(i+1)}(r)$ by mixing $c^{(i)}(r)$ and $c^{(i+\frac{1}{2})}(r)$:

$$c^{(i+1)}(r) = \lambda c^{(i+\frac{1}{2})}(r) + (1 - \lambda) c^{(i)}(r) \quad 0 < \lambda \leq 1$$

7. Check for convergence: If

$$\max |c^{(i+1)}(r) - c^{(i)}(r)| < \varepsilon$$

then the iteration is finished. If not, return to step 2.

The choice of the mixing parameter λ has a significant impact on the convergence behavior of the algorithm. A smaller value of λ leads to a slower yet more ensured convergence. If the correlation functions start to increase to extremely high values (i.e. $\sim 1 \times 10^6$), then a complete restart is necessary with a reduced value of λ . The parameter ε is typically of order $\varepsilon = 1 \times 10^{-8}$.

2.2.3.2 Achieving Thermodynamic Consistency with the RY Closure

Thermodynamic consistency between the virial route and the compressibility route is achieved by modifying the parameter α in the RY closure (see section 2.2.1). The function $\Delta\kappa(\alpha)$ is defined as the difference of the isothermal compressibility κ_T calculated via the two routes:

$$\Delta\kappa(\alpha) = \rho k_B T \kappa_T^v(\alpha) - \rho k_B T \kappa_T^c(\alpha),$$

with

$$\rho k_B T \kappa_T^c(\alpha) = 1 + \rho \tilde{h}(k=0; \rho, \alpha),$$

and

$$\rho k_B T \kappa_T^v(\alpha) = \frac{1}{\frac{\partial[\beta P^v(\alpha)]}{\partial \rho}}.$$

The derivative of the pressure with respect to the density can be calculated via

$$\begin{aligned} \frac{\partial[\beta P^v(\alpha)]}{\partial \rho} = & 1 - \frac{4\pi}{3} \rho \int_0^\infty dr r^3 \frac{d\beta\Phi(r)}{dr} g(r; \rho, \alpha) \\ & - \frac{2\pi}{3} \rho^2 \int_0^\infty dr r^3 \frac{d\beta\Phi(r)}{dr} \frac{\partial g(r; \rho, \alpha)}{\partial \rho} \\ & - \frac{2\pi}{3} \rho^2 \int_0^\infty dr r^3 \frac{d\beta\Phi(r)}{dr} \frac{\partial g(r; \rho, \alpha)}{\partial \alpha} \frac{d\alpha}{d\rho}. \end{aligned} \quad (2.23)$$

The last term in equation (2.23) above is usually omitted as it is much smaller than the other two terms and the neglect of the density dependence of α makes the calculations much easier. The derivative $\partial g(r; \rho, \alpha)/\partial \rho$ is calculated numerically:

$$\frac{\partial g(r; \rho, \alpha)}{\partial \rho} \cong \frac{g(r; \rho + \delta\rho, \alpha) - g(r; \rho, \alpha)}{\delta\rho}.$$

The numerical implementation of the algorithm works as follows:

1. Choose a starting value of $\alpha^{(0)}$ and set the iteration index i to 0. Usually $\alpha = 1$ or a known solution for similar system parameters is used.
2. Calculate $g(r; \rho, \alpha^{(i)})$, $g(r; \rho + \delta\rho, \alpha^{(i)})$, $g(r; \rho, \alpha^{(i)} + \epsilon)$, and $g(r; \rho + \delta\rho, \alpha^{(i)} + \epsilon)$. The value of $\delta\rho$ is typically $\delta\rho\sigma^3 \sim 1 \times 10^{-5}$.
3. Calculate $\Delta\kappa(\alpha^{(i)})$ and $\Delta\kappa(\alpha^{(i)} + \epsilon)$.
4. If $\Delta\kappa(\alpha^{(i)}) < \varsigma$ then the algorithm is finished. Typically, $\varsigma \sim 1 \times 10^{-6}$.
5. Set $\alpha^{(i+1)} = \alpha^{(i)} + \epsilon \Delta\kappa(\alpha^{(i)}) / [(\Delta\kappa(\alpha^{(i)} + \epsilon) - \Delta\kappa(\alpha^{(i)}))]$ and return to step 2.

It is possible that for no positive α -value consistency between the two routes can be achieved. In this case the RY closure cannot be used for that particular state of the liquid.

2.2.4 Calculation of the Free Energy

To calculate the full phase diagram of a system that includes both the liquid and the solid phase, one must be able to calculate the free energy of the liquid from the correlation functions. Some of the pair potentials that are considered in this

work are explicitly state-dependent and this fact has to be taken into account when calculating of the free energy $F(\rho)$ [40]. The ideal free energy per volume $f_{\text{id}}(\rho)$ is given by

$$\beta f_{\text{id}}(\rho) = \rho(\log \rho - 1) + \rho \log \Lambda^3,$$

and the excess part per volume f_{ex} is obtained by evaluating

$$\beta f_{\text{ex}}(\rho) = \frac{1}{2} \rho^2 \int d\mathbf{r} \beta \Phi(r) \int_0^1 d\lambda g^{(\lambda)}(r; \rho),$$

where $g^{(\lambda)}(r; \rho)$ represents the radial distribution function for the scaled pair potential $\lambda \Phi(r)$.

2.2.5 Phase Transitions

The coexistence of two phases is defined by thermal, mechanical, and chemical equilibrium which translates in the equality of temperature, pressure, and chemical potential. As all calculations were performed at constant temperature only the last two conditions are important. The pressure P and chemical potential μ can be calculated in the following way from the free energy per volume $F^*(\rho) = F(\rho)/V$:

$$\begin{aligned} P &= -\frac{\partial F}{\partial V} = -\frac{\partial(F^*(\rho)V)}{\partial V} \\ &= -F^*(\rho) - V \frac{\partial F^*(\rho)}{\partial \rho} \underbrace{\frac{\partial \rho}{\partial V}}_{-N/V^2} = \rho \frac{\partial F^*(\rho)}{\partial \rho} - F^*(\rho) \\ \mu &= \frac{\partial F}{\partial N} = \frac{\partial(F^*(\rho)V)}{\partial N} \\ &= V \frac{\partial F^*(\rho)}{\partial \rho} \underbrace{\frac{\partial \rho}{\partial N}}_{1/V} = \frac{\partial F^*(\rho)}{\partial \rho}. \end{aligned}$$

The equality of pressure and chemical potential between two phases 1 and 2 can be interpreted geometrically as tangent to both $F_1^*(\rho)$ and $F_2^*(\rho)$ (*double tangent construction*, see figure 2.1).

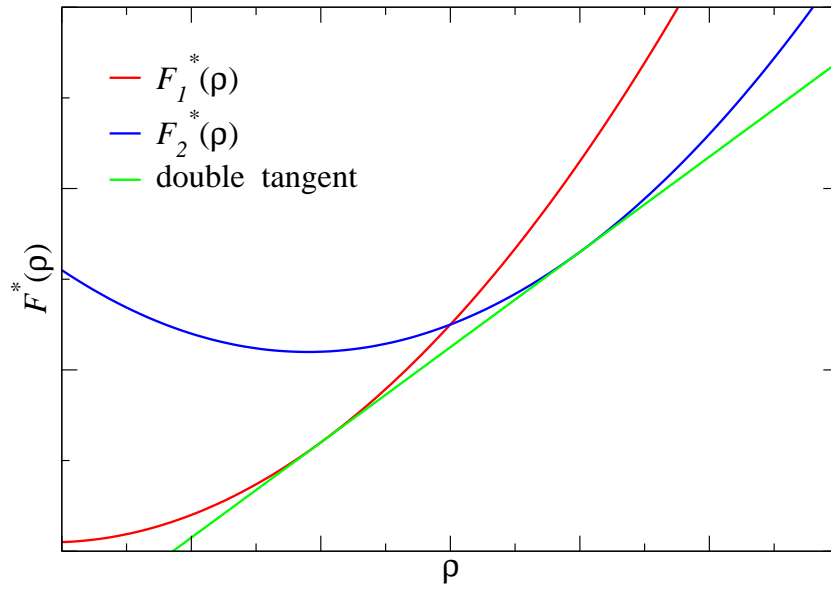


Figure 2.1: *Schematic representation of the double tangent construction close to the phase transition. The free energies of the two coexisting phases are denoted by $F_i^*(\rho)$.*

Chapter 3

Systems

The systems that were considered in this thesis belong to the class of *soft matter*. These materials are composed of mesoscopic particles (typical size 1nm–1 μ m) that are dispersed in a solvent whose constituent particles are much smaller in size. Such systems are also known as *complex fluids* or *colloidal dispersions*. These systems have a great diversity, for a general overview see [24, 25, 26].

Calculations for three different types of systems were performed in this work: Ionic microgels which are covered in more detail in section 3.1, star polymers (see section 3.2), and the Gaussian core model and its generalization (see section 3.3).

3.1 Ionic Microgels

Microgels [41] are cross-linked latex particles that are swollen by a good solvent. Depending on their monomer- and cross-linking density they can behave like hard-sphere particles [42] or soft colloids [43]. They are used as rheological control agents in automotive surface coatings and show promise in printing applications. Additionally, they might be used as drug delivery systems if they can be designed to swell in close proximity to the target sites in the body. The most common constituent polymer of microgels is poly(*N*-isopropylacrylamide) (PNIPAM) which produces microgels that swell in water (see figure 3.1). Other polymers like polyacrylic acid, polystyrene, or starch are also used. The polymers of an ionic microgel carry ionizable groups so that the microgel carries a net charge in the solution.

An *effective interaction potential* that does not depend on the less relevant degrees of freedom (like fluctuations of the macromolecules, or the coordinates and momenta of the counterions and solvent molecules) facilitates the calculations enormously for theoretical purposes. The effective Hamiltonian \mathcal{H}_{eff} has the form

$$\mathcal{H}_{\text{eff}} = \sum_{i=1}^N \frac{\mathbf{P}_i^2}{2m} + \sum_{i<j} \Phi_{\text{eff}}(|\mathbf{r}_i - \mathbf{r}_j|) + E_0,$$

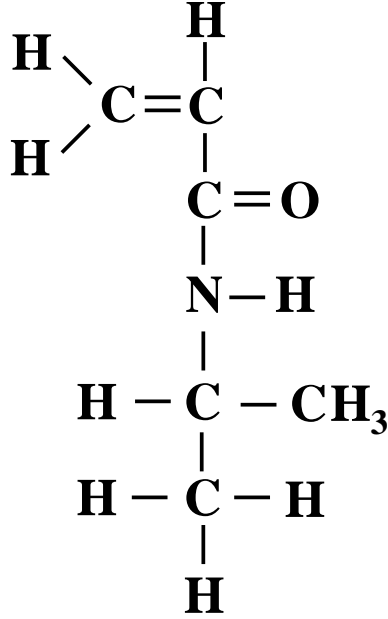


Figure 3.1: *The structural formula of Isopropylacrylamide.*

where \mathbf{P}_i denotes the momentum and \mathbf{R}_i the position of the center of the i -th microgel particle, and N is the total number of microgel particles. The term E_0 is usually called *volume term* because it does not depend on the positions or momenta of the microgels but on their number density ρ . This term will be discussed below.

The effective Hamiltonian \mathcal{H}_{eff} fulfills the relation

$$\mathcal{Z} = \langle e^{-\beta \mathcal{H}} \rangle = \langle e^{-\beta \mathcal{H}_{\text{eff}}} \rangle_m,$$

where \mathcal{H} represents the Hamiltonian of the full system, including counterions and solvent molecules, $\langle \dots \rangle$ denotes a canonical trace, and the subscript m refers to a trace with respect to the coordinates and momenta of the microgels *only*.

Within the formalism of linear response theory one can approximately calculate the effective potential (for details see [44]). It has the following functional form:

$$\beta \Phi_{\text{eff}}(r) = \begin{cases} \frac{Z^2 \lambda_B}{\sigma} \left[\frac{24}{\kappa^2 \sigma^2} - \frac{72}{\kappa^3 \sigma^3} \left(e^{-\kappa \sigma} \left(1 + \frac{2}{\kappa \sigma} \right)^2 + \left(1 - \frac{4}{\kappa^2 \sigma^2} \right) \right) \right] & r = 0 \\ \frac{Z^2 \lambda_B}{\sigma} \left[\frac{24}{\kappa^2 \sigma^2} + \frac{r}{\sigma} \left(\frac{144}{\kappa^4 \sigma^4} - \frac{36}{\kappa^2 \sigma^2} \right) + \frac{r^3}{\sigma^3} \frac{12}{\kappa^2 \sigma^2} \right. \\ \left. - \frac{72}{\kappa^4 \sigma^4} \frac{\sigma}{r} \left(e^{-\kappa \sigma} \left(1 + \frac{2}{\kappa \sigma} \right)^2 \sinh(\kappa r) + \left(1 - \frac{4}{\kappa^2 \sigma^2} \right) (1 - e^{-\kappa r}) \right) \right] & r \leq \sigma \\ \frac{Z^2 \lambda_B}{\sigma} \frac{144}{\kappa^4 \sigma^4} \left(\cosh(\kappa \sigma / 2) - \frac{2 \sinh(\kappa \sigma / 2)}{\kappa \sigma} \right)^2 \frac{\sigma}{r} e^{-\kappa r} & r > \sigma. \end{cases} \quad (3.1)$$

In this equation Z is the net charge number of the microgels (possible Manning-condensed counterions have been subtracted), σ is the diameter of a microgel

particle, κ is the inverse Debye screening length, namely,

$$\kappa = \sqrt{4\pi Z\rho\lambda_B},$$

and λ_B is the Bjerrum length that denotes the distance at which the electrostatic interaction between two elementary charges roughly equals the thermal energy:

$$\lambda_B = \frac{e^2}{\epsilon k_B T},$$

where e denotes the elementary charge and ϵ the dielectric constant of the solvent. The Bjerrum length has the value $\lambda_B = 0.714\text{nm}$ for water at room temperature and is kept fixed at that value in this work. The resulting effective potential shows an explicit density dependence through κ . It is visualized in the figures 3.2 and 3.3.

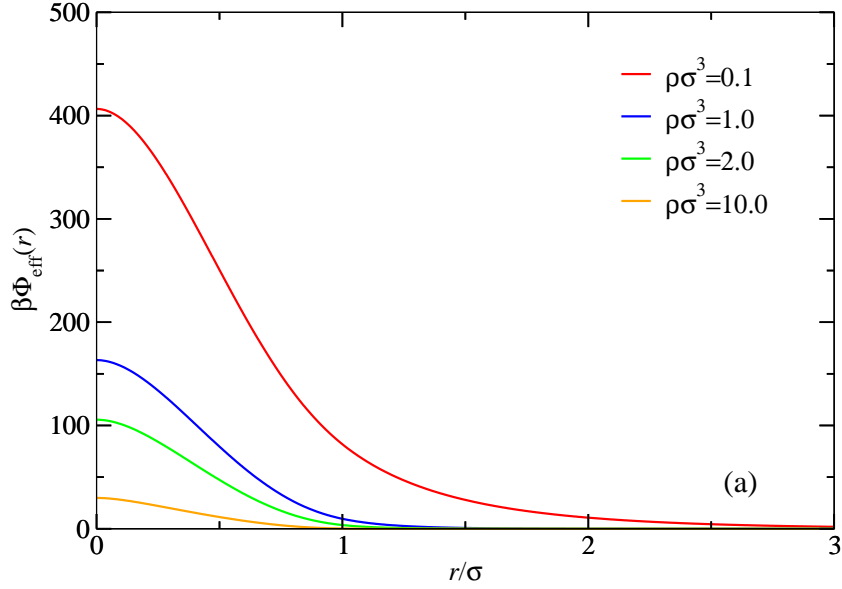


Figure 3.2: *The effective interaction potential between charged microgels for fixed charge $Z = 200$ and varying density.*

The volume term E_0 contains contributions from the counterion degrees of freedom and is given by:

$$E_0 = ZNk_B T [\ln(Z\rho\Lambda^3) - 1] - N \frac{6Z^2 e^2}{\epsilon\sigma} \left\{ \frac{1}{5} - \frac{2}{\kappa^2 \sigma^2} + \frac{6}{\kappa^3 \sigma^3} \left[1 - \frac{4}{\kappa^2 \sigma^2} + \left(1 + \frac{4}{\kappa\sigma} + \frac{4}{\kappa^2 \sigma^2} \right) e^{-\kappa\sigma} \right] \right\} - ZN \frac{k_B T}{2}, \quad (3.2)$$

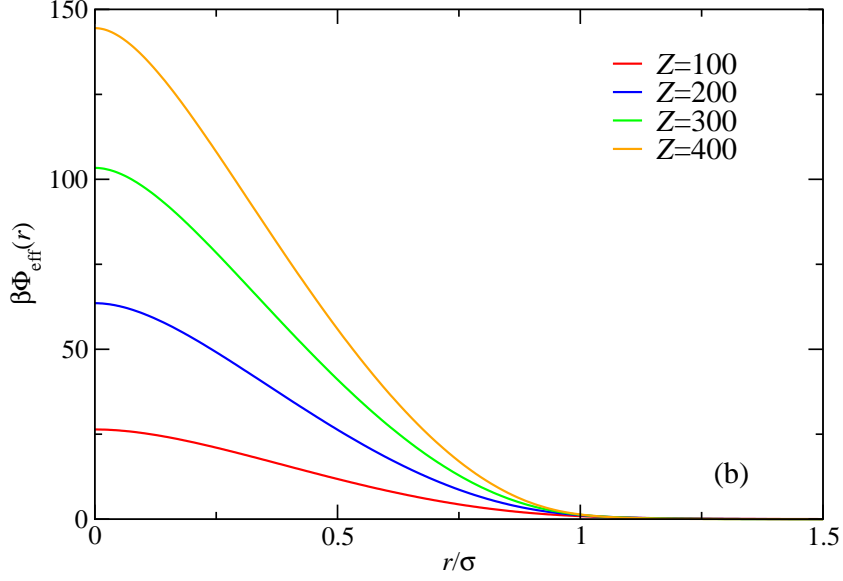


Figure 3.3: *The effective interaction potential between charged microgels for fixed density $\rho\sigma^3 = 4$ and varying Z .*

where Λ is the thermal de Broglie wavelength. Though the volume term has no influence on the correlation functions of the microgel particles it is an important contribution to the thermodynamics of the system. The dimensionless volume term $\beta\sigma^3 E_0/V$ is depicted in figure 3.4.

This model neglects the steric repulsion that stems from the overlap between the monomers of two interacting microgels. If the microgels are considered as homogeneous spheres with diameter σ and monomer volume fraction ϕ the steric free energy of a single microgel particle is given by [45]

$$F_{\text{st}}^{(1)} = \frac{V_0}{v_c} k_B T \left(\frac{1}{2} - \chi \right) \phi^2,$$

where $V_0 = \pi\sigma^3/6$ is the volume of a microgel particle, v_c is the volume of a monomer, and χ characterizes the solvent quality ($0 < \chi < 1/2$ represents a good solvent and $\chi > 1/2$ a poor one). The generalization of the Flory-Huggins theory to two overlapping microgels with a center-to-center distance $r < \sigma$ leads to [31]

$$F_{\text{st}}^{(2)}(r) = \frac{2V_0}{v_c} k_B T \left(\frac{1}{2} - \chi \right) \phi^2 \left[1 - \frac{3}{2} \left(\frac{r}{\sigma} \right) + \frac{1}{2} \left(\frac{r}{\sigma} \right)^3 \right] + 2F_{\text{st}}^{(1)}.$$

Therefore the steric interaction potential, $\Phi_{\text{st}}(r) = F_{\text{st}}^{(2)}(r) - F_{\text{st}}^{(2)}(\infty)$, reads

$$\Phi_{\text{st}}(r) = \begin{cases} \alpha \left[1 - \frac{3}{2} \left(\frac{r}{\sigma} \right) + \frac{1}{2} \left(\frac{r}{\sigma} \right)^3 \right] & r \leq \sigma \\ 0 & r > \sigma. \end{cases} \quad (3.3)$$

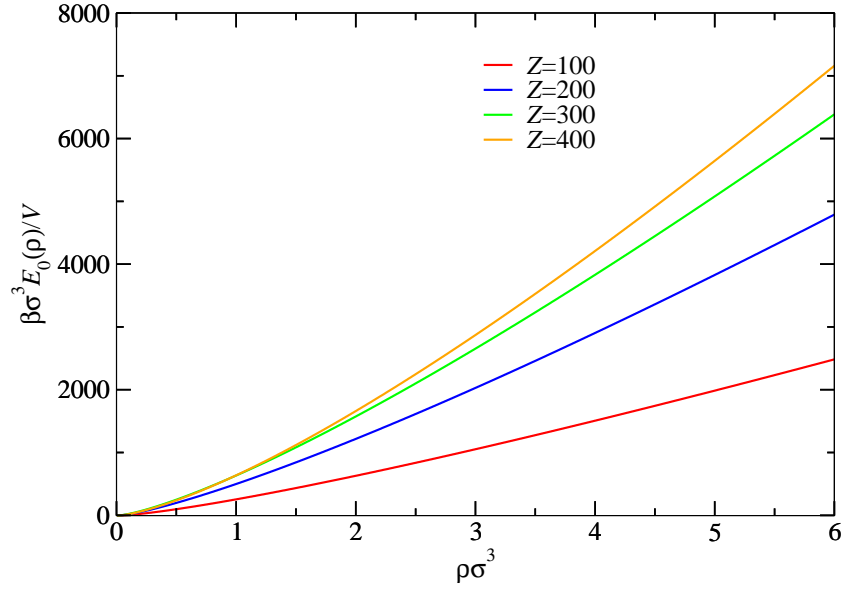


Figure 3.4: *The dimensionless volume term of charged microgels for varying Z .*

The pre-factor α is given by

$$\alpha = \frac{2V_0}{v_c} k_B T \left(\frac{1}{2} - \chi \right) \phi^2.$$

Inserting typical values for PNIPAM microgels yields an estimate for the range of α

$$\left(\frac{1}{2} - \chi \right) \lesssim \alpha \lesssim 200 \left(\frac{1}{2} - \chi \right),$$

with $0 \leq \chi \leq 1/2$. The steric interaction potential is visualized in figure 3.5.

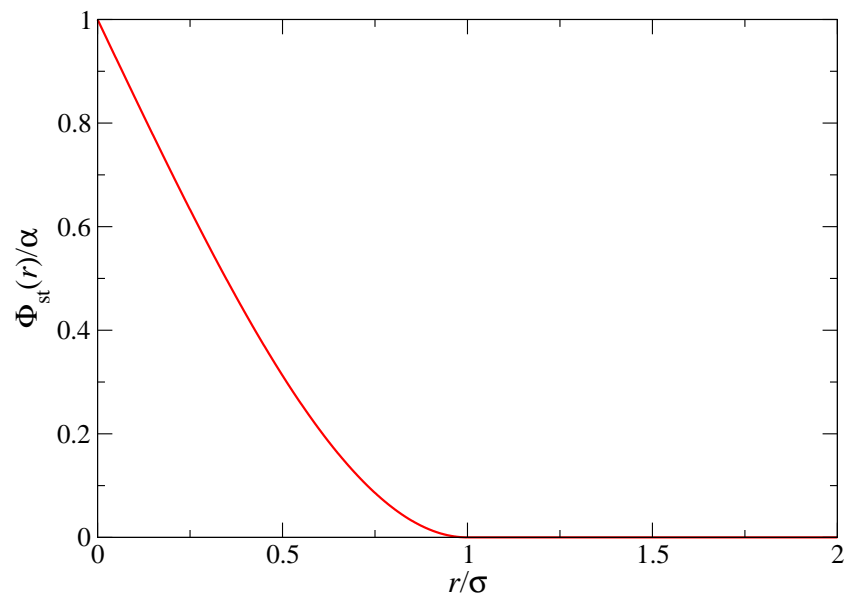


Figure 3.5: *The steric interaction potential of microgels.*

3.2 Star Polymers

Star polymers are particles of mesoscopic size, where f linear polymer chains are anchored on a common core. The number of “arms” f is called *functionality* of the star polymer. The finite size of the core can be neglected if the chains are much longer than the diameter of the core. Similar to the procedure in the above section 3.1, an effective interaction potential $\Phi_{\text{sp}}(r)$ between two star polymer particles can be obtained that depends on the distance between their centers only [46, 47]. For $f \gtrsim 10$ it is given by (see figure 3.6)

$$\beta\Phi_{\text{sp}}(r) = \frac{5}{18}f^{3/2} \begin{cases} -\log \frac{r}{\sigma} + \frac{1}{1+\sqrt{f}/2} & r \leq \sigma \\ \frac{\sigma}{r(1+\sqrt{f}/2)} e^{-\frac{\sqrt{f}}{2\sigma}(r-\sigma)} & r > \sigma, \end{cases} \quad (3.4)$$

where σ is the corona diameter. The interaction diverges only logarithmically at the origin so this system is also considered to be a soft one.

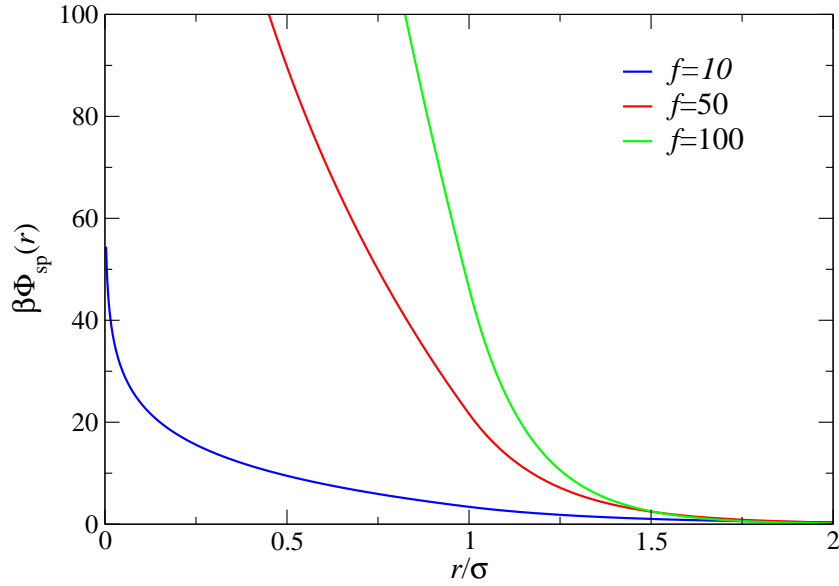


Figure 3.6: *The effective interaction potential of star polymers for varying functionality f .*

3.3 The Gaussian Core Model and its Generalization

The Gaussian core model (GCM) approximates the effective interaction between the centers of mass of two polymer chains. The Flory-Krigbaum potential [48]

that describes the exact interaction potential between polymer chains is given by

$$\beta\Phi_{\text{FK}}(r) = N^2 \frac{v_{\text{seg}}^2}{v_{\text{solv}}} \left(\frac{3}{4\pi R_g^2} \right)^{3/2} (1 - 2\chi) e^{-\frac{3r^2}{4R_g^2}},$$

where N denotes the degree of polymerization (the number of monomers of the polymer), v_{seg} is the volume of a monomer segment, v_{solv} the volume of a solvent molecule, R_g the radius of gyration of the chains, and χ characterizes the quality of the solvent. The interaction potential of the GCM reads

$$\Phi_{\text{GCM}}(r) = \varepsilon e^{-(r/\sigma)^2}, \quad (3.5)$$

with an energy scale ε and a length scale σ . The thermodynamics and the phase behavior of the GCM have already been studied [49, 50].

The *generalized Gaussian core model* (GGCM) [51] is a generalization of the GCM and is characterized by the interaction potential

$$\Phi_{\text{GGCM-}n}(r) = \varepsilon e^{-(r/\sigma)^n}, \quad (3.6)$$

where σ defines the length scale and ε the energy scale. The parameter n governs the steepness of the repulsion: $n = 2$ equals the GCM and in the limit $n \rightarrow \infty$ the interaction potential of the penetrable sphere model (PSM) is obtained:

$$\Phi_{\text{PSM}}(r) = \begin{cases} \varepsilon & r \leq \sigma \\ 0 & r > \sigma. \end{cases}$$

Figure 3.7 shows the potential of the three models.

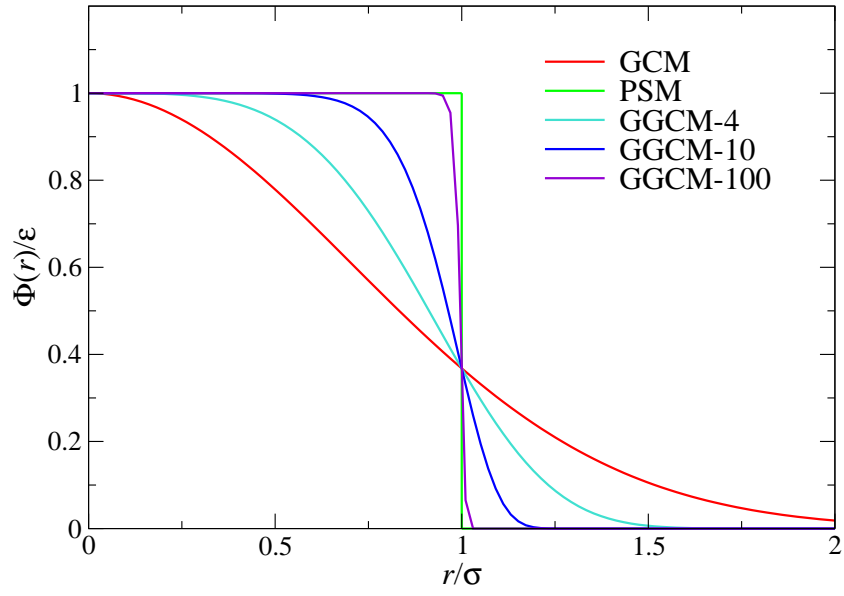


Figure 3.7: *The interaction potential of the Gaussian core model (GCM), the penetrable sphere model (PSM), and the generalized Gaussian core model (GGCM) for $n = 4, 10, 100$.*

Chapter 4

Results

4.1 Freezing

4.1.1 Star Polymers

The first test of the utility of the GA was checking the zero-temperature phase diagram of star polymer solutions that had already been published [3] (reproduced in figure 4.1). That phase diagram was determined by comparing the lattice sum of 3 different crystal structures - bco, diamond, and A15 (for details see appendix A). The first calculation with the GA was performed with 1,2, and 8 basis particles using fitness function (1.10). The GA confirmed the fcc structure for low densities and the diamond structure for $2 \lesssim \rho\sigma^3 \lesssim 2.6$ but predicted a trigonal structure instead of bco for $1.3 \lesssim \rho\sigma^3 \lesssim 1.9$. A more detailed calculation with a bco, trigonal and diamond structure as candidates showed that the trigonal structure has indeed a lower free energy than the bco one (see figure 4.2). Instead of the bco structures proposed in [3] for densities $\rho\sigma^3 \gtrsim 2.6$ the GA predicts a simple hexagonal lattice and then a hexagonal close-packed structure that both have lower free energies than the respective bco structure. The phase diagram calculated with the GA is plotted in figure 4.3.

An obvious flaw of the calculations with the GA are the problems near the phase transition. Close to the intersection of the free energy curves of the two competing structures the respective values of the fitness function are almost identical and both structures propagate in the population. As a consequence of the random elements in the algorithm the final crystal structure was either one of the two structures or a different one with a free energy value between the one of the two competing structures (see figure 4.4). This problem can easily be overcome by calculating the free energies close to the phase boundaries, using the structures predicted by the GA as candidates.

Another shortcoming is the fact that the GA does neither find any structure that has a lower free energy than the A15 structure, nor the A15 structure itself for densities $\rho\sigma^3 \gtrsim 4$ which led to the conjecture that indeed the A15 structure is

the stable crystal structure for high densities. Thus the zero-temperature phase diagram was calculated using fcc, trigonal, diamond, hexagonal, hcp, and A15 as candidate structures (see figure 4.5).

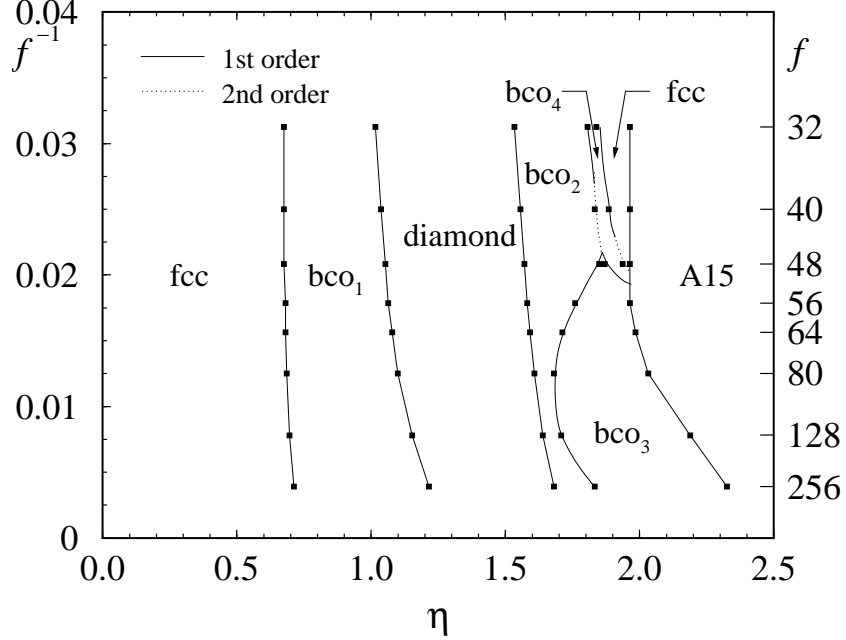


Figure 4.1: The zero-temperature phase diagram of star polymers is reproduced from [3]. The packing fraction is denoted by $\eta = \pi\rho\sigma^3/6$ and the functionality of the star polymers by f .

The inability of the GA to find the A15 structure at high densities is most likely due to the high number of local minima near the global minimum. The values of the reduced free energy become quite large in these density ranges (typically ~ 1500) and the fitness function (1.10) barely discriminates values that differ only slightly ($\sim \pm 5$). To improve the performance of the GA the fitness function (1.11) was used with different functional forms for $g(i)$:

$$g(i) = 1 + ai \quad a \in \left\{ \frac{1}{10}, \frac{2}{10}, \frac{3}{10} \right\}.$$

With this fitness function the behavior at low generation number i is almost identical to the one of (1.10) while small changes in the free energy have a more significant impact in later generations (see figure 4.6). With this enhancement the GA was able to find a structure with eight basis particles that has a lower free energy value than the one of an A15 structure (see figure 4.7). The structure in these cases is a single-face centered monoclinic lattice with eight basis particles (see figure 4.8).

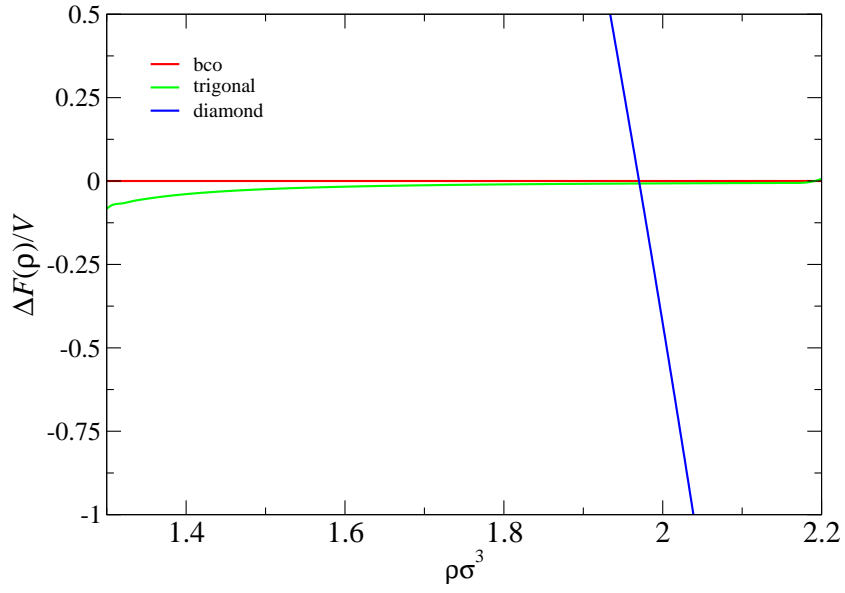


Figure 4.2: The free energy per volume as a function of density of a bco, trigonal, and diamond structure for star polymers with $f = 40$.

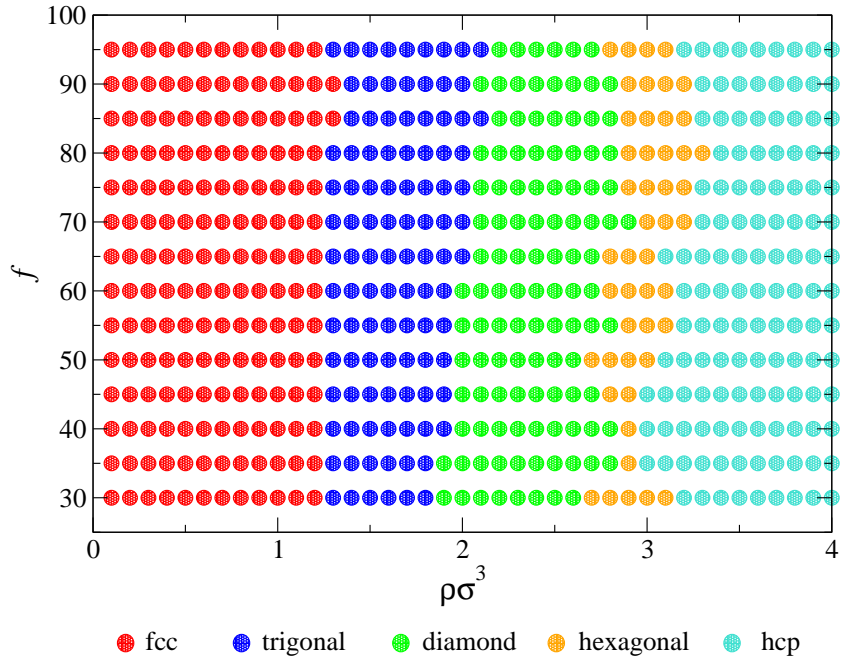


Figure 4.3: The zero-temperature phase diagram of star polymers (functionality f vs. density) calculated with the genetic algorithm. The Symbols indicate the respective stable crystal structure.

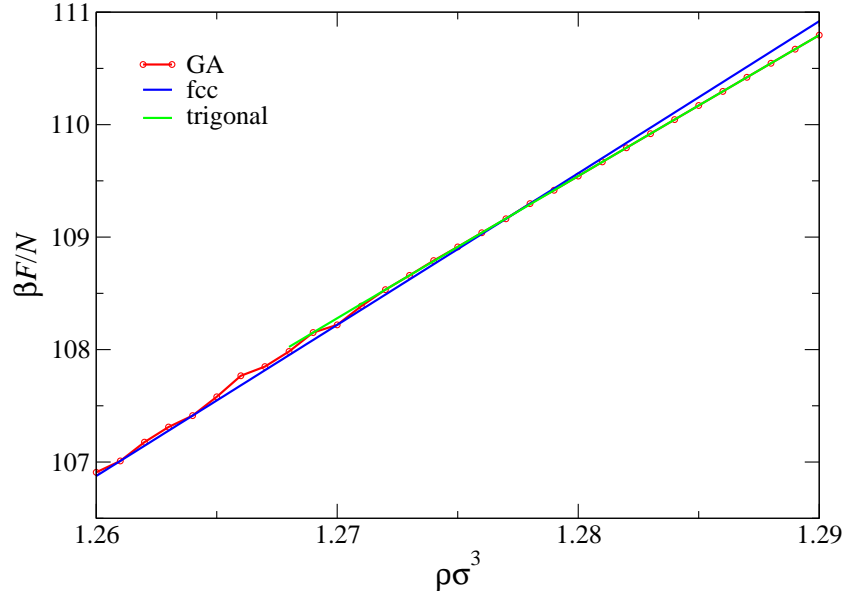


Figure 4.4: The dimensionless free energy per particle as a function of density of star polymers with $f = 40$ for a fcc structure, a trigonal structure, and calculated with the genetic algorithm close to the transition from fcc to trigonal.

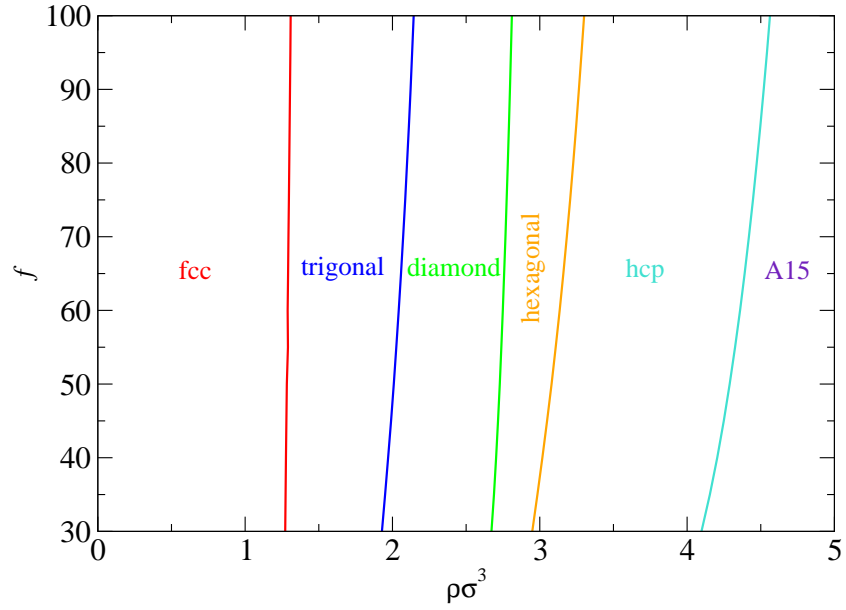


Figure 4.5: The zero-temperature phase diagram (functionality f vs. density) of star polymers calculated using fcc, trigonal, diamond, hexagonal, hcp, and A15 structures as candidates. The lines denote the points where the free energy curves intersect.

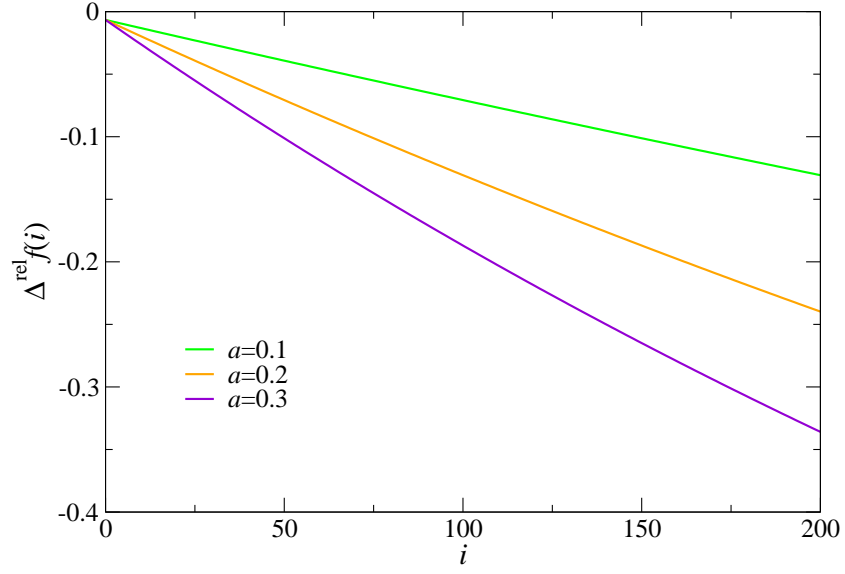


Figure 4.6: The relative difference of the fitness between a structure with $\beta F/N = 1495$ and $\beta F/N = 1505$ calculated with the fitness function (1.11) for three different values of a . The free energy of the reference structure was assumed to have a value of 1500.

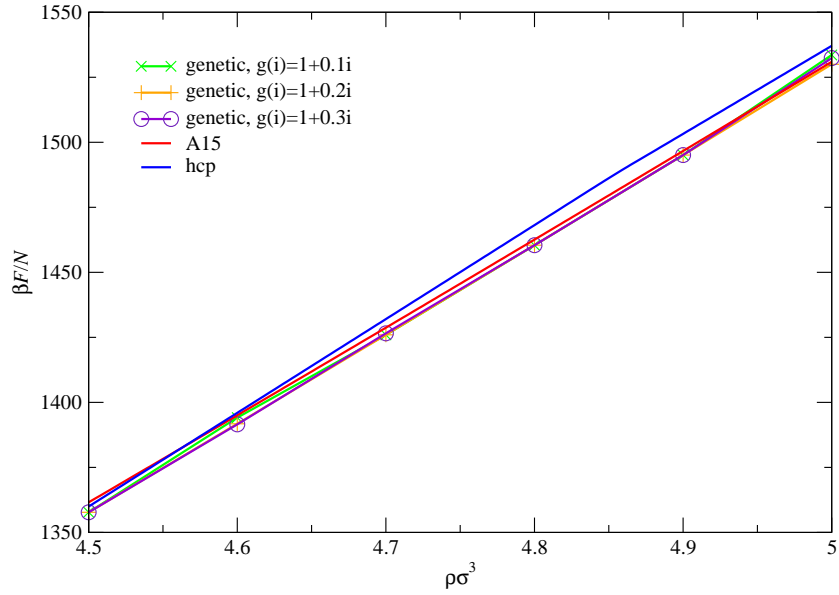


Figure 4.7: The dimensionless free energy per particle as a function of density for a hcp structure, an A15 structure, and calculated with the GA using three different fitness functions.

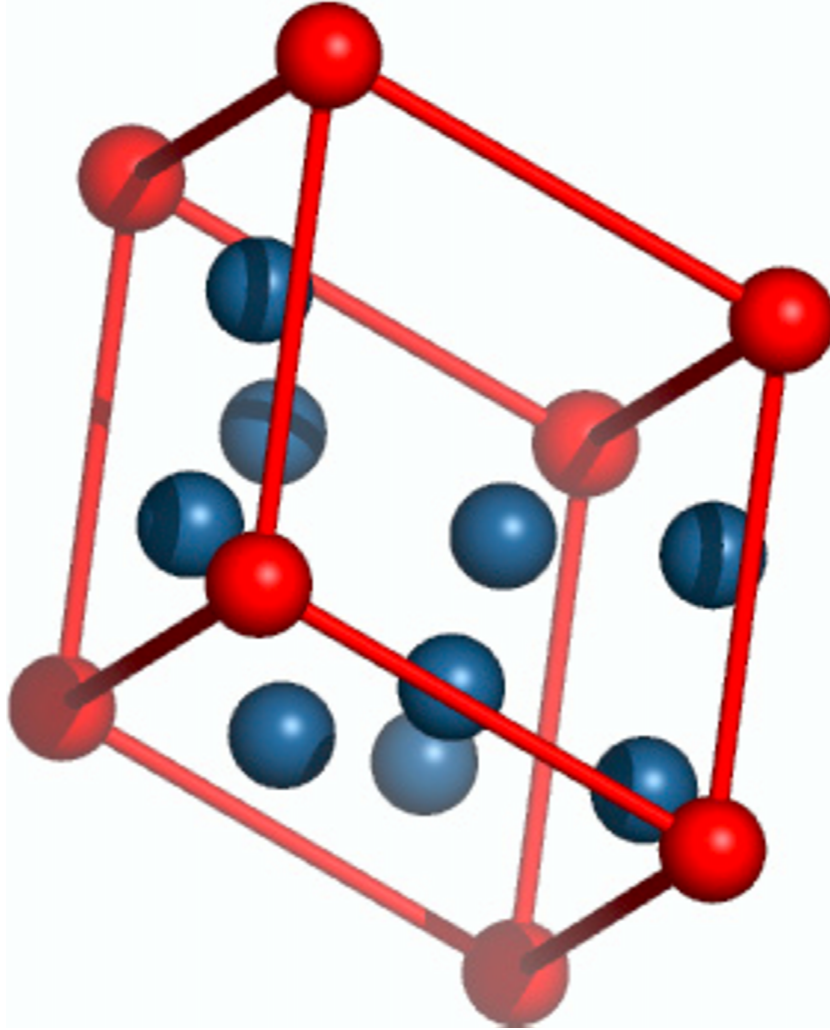


Figure 4.8: *Unit cell of the crystal structure of a star polymer with $f = 100$ and $\rho\sigma^3 = 5$ found with the GA. The underlying Bravais lattice is single-face centered monoclinic.*

4.1.2 Microgels

4.1.2.1 Predictions

The phase behavior of loosely cross-linked microgels with low monomer density, for which the interaction potential (3.1) was derived, was yet unknown, so the investigation started with the calculation of the zero-temperature phase diagram via the genetic algorithm (figure 4.9) to find the possible candidates. The free energy of the solid was calculated via lattice sums (see section 2.1.1)

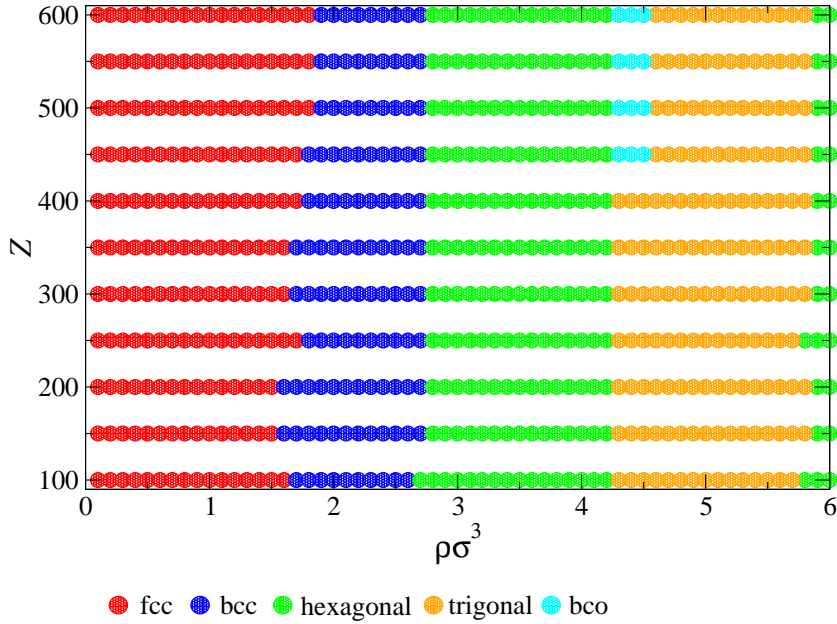


Figure 4.9: *The zero-temperature phase diagram (charge number Z vs. density) of an ionic microgel with $\sigma=100\text{nm}$ calculated with the genetic algorithm. The symbols denote the respective stable crystal structure.*

It was unclear, whether taking into account the influence of entropy on the free energy would have a significant impact on the phase diagram of the solids for $T > 0$. To investigate this phenomenon, the free energy was calculated via the Einstein model (see section 2.1.2) and the localization parameter α was included in the individual to optimize it at the same time as the lattice parameters. The calculations showed that the sequence of crystal structures as a function of density stays the same but the phase borders are slightly shifted and a narrow bco-region shows up between the bcc- and the hexagonal region (see figure 4.10).

In both cases the algorithm has problems close to the phase boundaries so in order to obtain their exact locations additional calculations using the predicted structures as candidates are required (see figures 4.12 and 4.13).

The Hansen-Verlet criterion [52] predicts a liquid-solid phase transition where

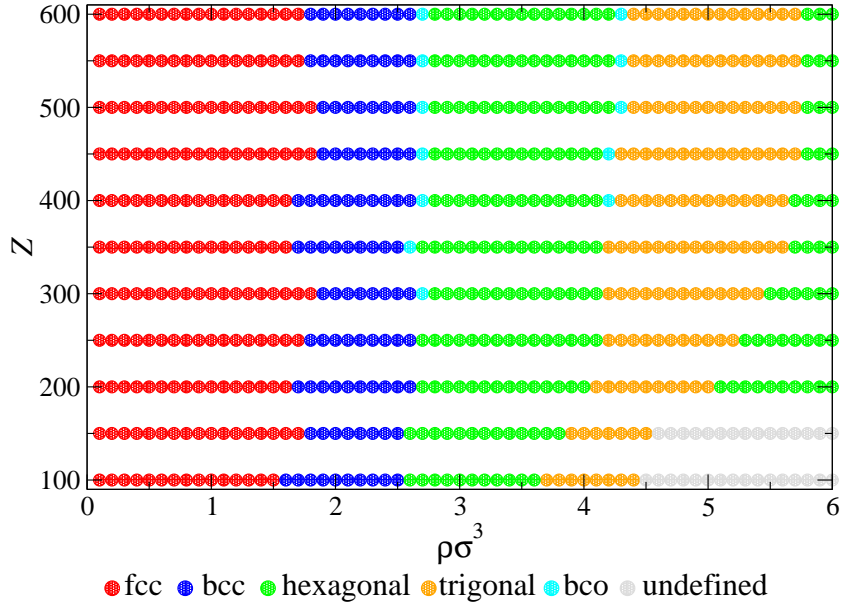


Figure 4.10: *The phase diagram of an ionic microgel (charge number Z vs. density) with $\sigma=100\text{nm}$ calculated with the genetic algorithm using the Einstein model to calculate the free energy. The crystal structures in the points labeled “undefined” vary rapidly with the density, so no single structure can be assigned to this region. This proved to be no problem since the system was liquid in this region.*

the main peak of the structure factor $S(k)$ reaches a value of ~ 2.85 . The OZ-equation was solved with the HNC closure relation (2.19) and the structure factor was calculated from the correlation functions. The value of the main peak of $S(k)$ can be seen in figure 4.11. According to this criterion a re-entrant melting transition is predicted at densities $1 \gtrsim \rho\sigma^3 \gtrsim 2.5$ and $150 \gtrsim Z \gtrsim 250$. Re-entrant melting, where the liquid freezes upon compression but becomes liquid again upon further compression, is one scenario that can happen in soft systems (for more details see section 4.3). The system should be frozen for $Z \gtrsim 300$ everywhere except for very low densities. The increase of the first peak of the structure factor upon compression is typical for all substances but the subsequent decrease only happens in soft systems and hints at a re-entrant melting process.

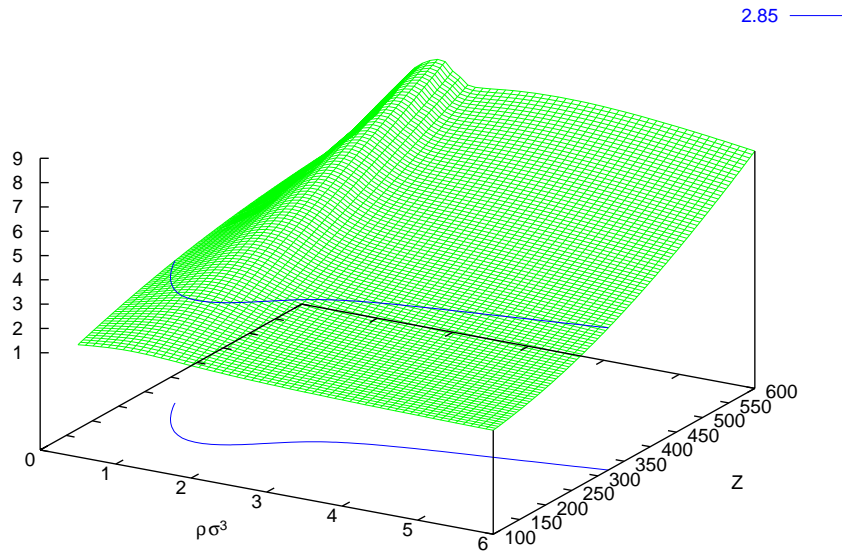


Figure 4.11: The value of the main peak of the structure factor $S(k)$ for microgels calculated with the HNC closure as a function of charge number Z and density. The blue line marks the parameter values where $S(k) = 2.85$.

4.1.2.2 Liquid-Solid Phase Diagram

The full liquid-solid phase diagram of microgels was determined by calculating the free energy of the solid structures predicted by the GA within the Einstein approximation and the free energy of the liquid using both the HNC and the RY closure. The phase diagrams calculated with the HNC closure (figure 4.12) and calculated with the RY closure (figure 4.13) look qualitatively similar. The most notable quantitative difference is the location of the liquid-fcc-bcc-liquid transition. The comparison with the prediction from the Hansen-Verlet criterion shows a good agreement for low densities but it fails to predict the double re-entrant melting at $\rho\sigma^3 \sim 3$.

The coordination number of the crystal structures decrease with increasing density from twelve (fcc), eight (bcc), to two (hexagonal, trigonal, and bco). The correlation functions of the liquid calculated close to the transitions show a precursor of these values. The number of next neighbors $n_{\text{n.n.}}$ in a liquid can be calculated via

$$n_{\text{n.n.}} = 4\pi\rho \int_0^{r_c} r^2 g(r) dr,$$

where r_c denotes the position of the first minimum of $g(r)$. The correlation functions were calculated with the HNC closure. The following state points were chosen to calculate these values:

- $\rho\sigma^3 = 0.3$, $Z = 200$, near the liquid-fcc transition (see figure 4.14). The point is marked by “(a)” in figure 4.12. The number of neighbors is approximately twelve, i.e. the number of next neighbors in a fcc lattice.
- $\rho\sigma^3 = 2.3$, $Z = 200$, near the bcc-liquid transition (see figure 4.15). The point is marked by “(b)” in figure 4.12. The number of neighbors is approximately 14, i.e. the sum of the first two next neighbors shells in a bcc lattice which are very close together (eight particles at distance $\sqrt[3]{2/\rho}\sqrt{3}/2$ and six particles at distance $\sqrt[3]{2/\rho}$).
- $\rho\sigma^3 = 3.2$, $Z = 400$, near the liquid-hexagonal transition (see figure 4.16). The point is marked by “(c)” in figure 4.12. Here the location of the first minimum is hard to find due to the shoulder in $g(r)$ but the next neighbor number of two in the hexagonal lattice is reasonably well predicted.
- $\rho\sigma^3 = 4.8$, $Z = 520$, near the trigonal-liquid transition (see figure 4.17). The point is marked by “(d)” in figure 4.12. In this case the first minimum is again pronounced and the number of neighbors in the liquid is two as in the trigonal lattice.

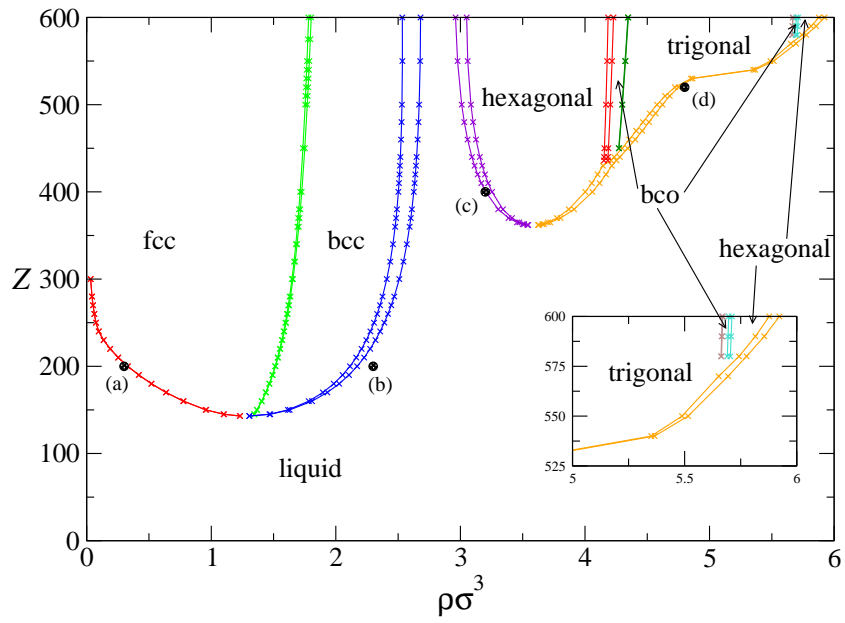


Figure 4.12: *Liquid-solid phase diagram (charge number Z vs. density) of microgels with $\sigma = 100\text{nm}$. The properties of the liquid phase were calculated with the HNC closure and the properties of the solid phase with the Einstein model. The circles mark the points where the number of next neighbors were investigated.*

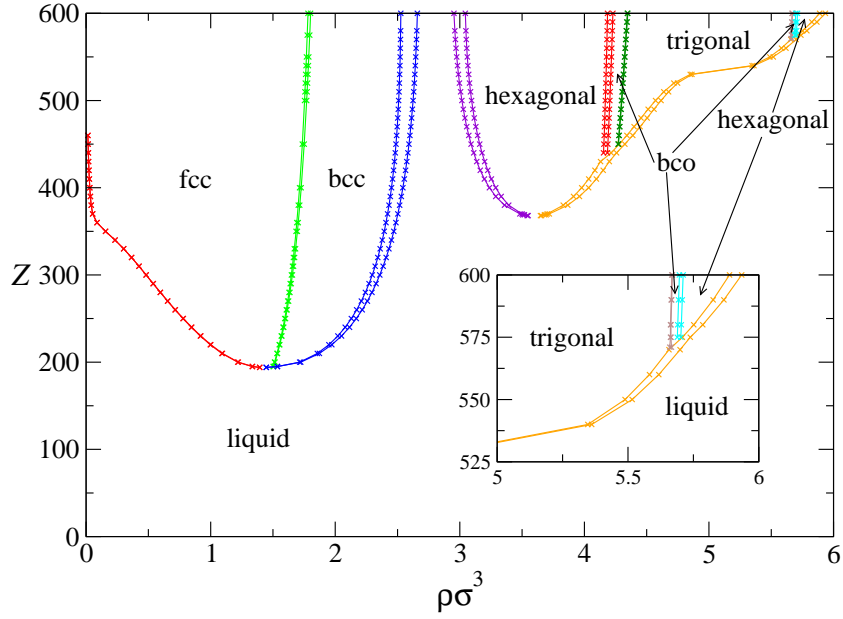


Figure 4.13: *Liquid-solid phase diagram (charge number Z vs. density) of microgels with $\sigma = 100nm$. The properties of the liquid were calculated with the RY closure and the properties of the solid phase with the Einstein model.*

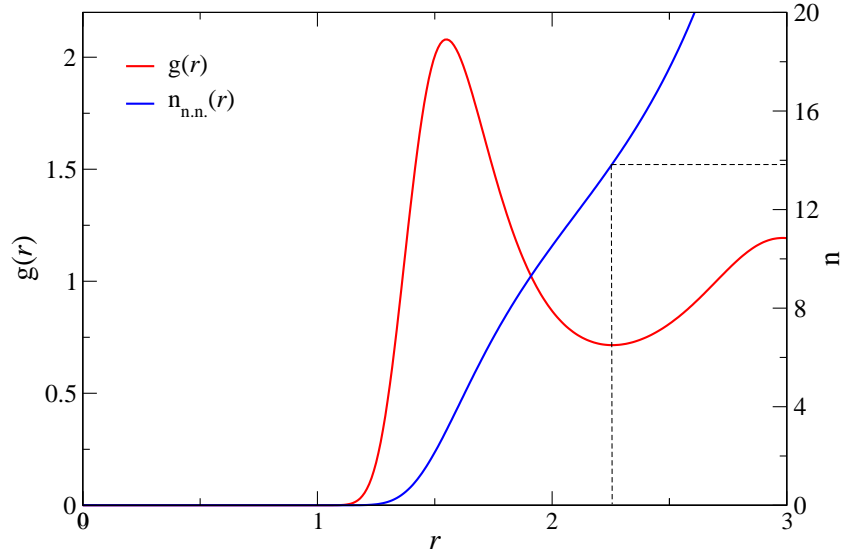


Figure 4.14: *Pair correlation function $g(r)$ and number of neighbors $n_{n.n.}(r_c)$ of a microgel with $\rho\sigma^3 = 0.3$, $Z = 200$, and $\sigma = 100nm$. The correlation functions were calculated with the HNC closure.*

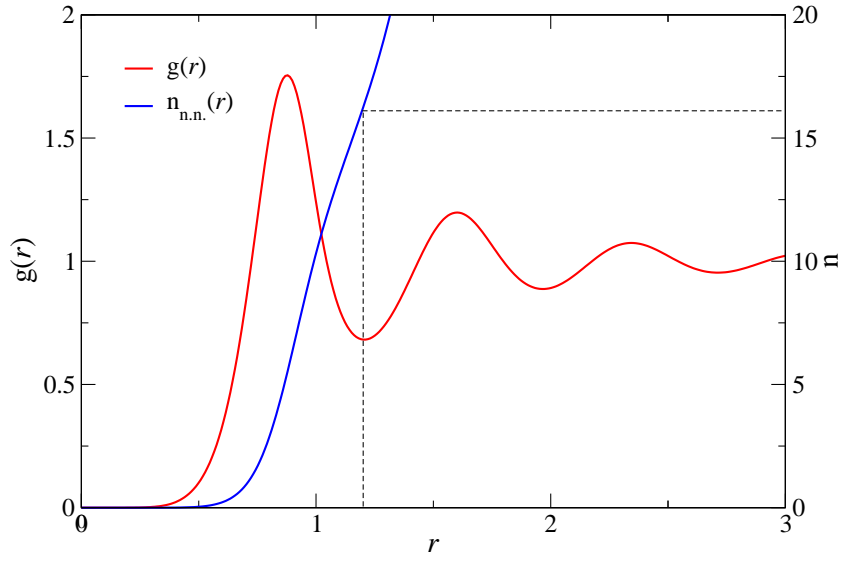


Figure 4.15: Pair correlation function $g(r)$ and number of neighbors $n_{\text{n.n.}}(r_c)$ of a microgel with $\rho\sigma^3 = 2.3$, $Z = 200$, and $\sigma = 100\text{nm}$. The correlation functions were calculated with the HNC closure.

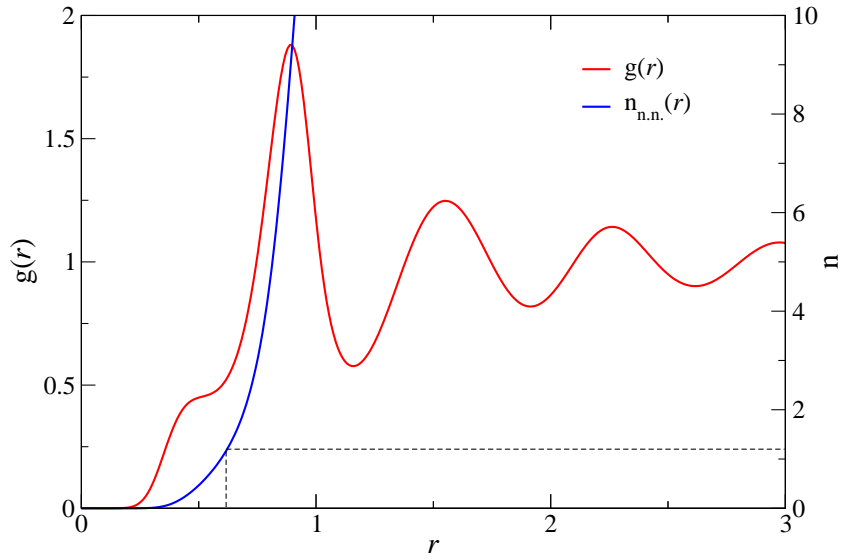


Figure 4.16: Pair correlation function $g(r)$ and number of neighbors $n_{\text{n.n.}}(r_c)$ of a microgel with $\rho\sigma^3 = 3.2$, $Z = 400$, and $\sigma = 100\text{nm}$. The correlation functions were calculated with the HNC closure.

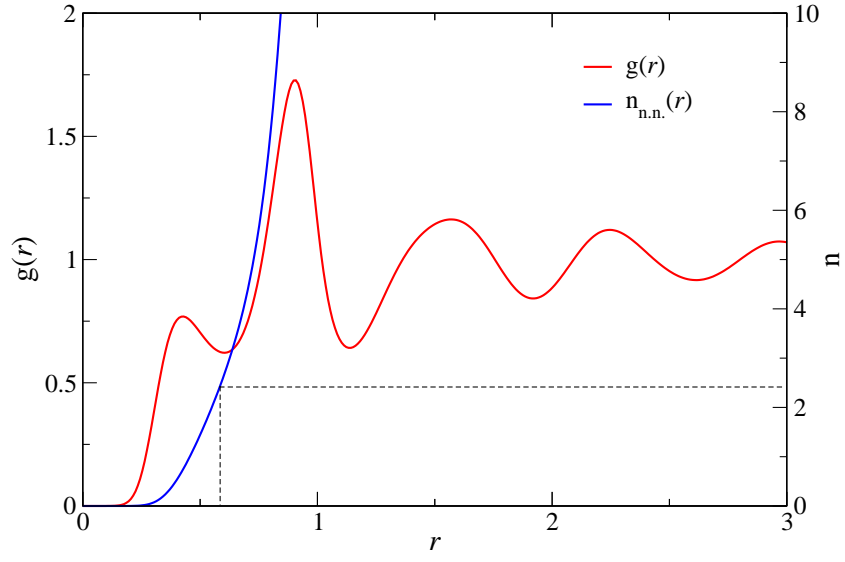


Figure 4.17: Pair correlation function $g(r)$ and number of neighbors $n_{\text{n.n.}}(r_c)$ of a microgel with $\rho\sigma^3 = 4.8$, $Z = 520$, and $\sigma = 100nm$. The correlation functions were calculated with the HNC closure.

4.1.2.3 Lindemann Ratio

The Lindemann parameter [53] L is defined as the root-mean square displacement of a particle from a lattice site, due to the harmonic oscillations, over the nearest-neighbor distance a_0 :

$$L = \frac{\sqrt{\langle r^2 \rangle_\rho}}{a_0},$$

with

$$\langle r^2 \rangle_\rho = \frac{\int d\mathbf{r} r^2 \rho(r)}{\int d\mathbf{r} \rho(r)}.$$

For the density (2.10) this expression becomes

$$\langle r^2 \rangle_\rho = \frac{3}{2\alpha}.$$

The Lindemann ratio of the crystals encountered in the phase diagrams was calculated for $Z = 300$ (figure 4.18), $Z = 350$ (figure 4.19), $Z = 400$ (figure 4.20), $Z = 450$ (figure 4.21), $Z = 500$ (figure 4.22), $Z = 550$ (figure 4.23), and $Z = 600$ (figure 4.24). The microgel diameter was fixed at $\sigma = 100\text{nm}$. Usually, a Lindemann ratio of 10 to 13% is considered an indication of a melting transition. However, this criterion was only used for systems that show a steep repulsion near overlap, accordingly its validity for soft systems is not granted.

Similar to the predictions of the Hansen-Verlet criterion the Lindemann ratios predict the first re-entrant melting but fail at the second one. The crystals are delocalized very strongly and the stable structures are not the ones with the lowest Lindemann ratio. Instead, the crystal structure that has the lowest value of L aside from fcc and bcc is the stable one.

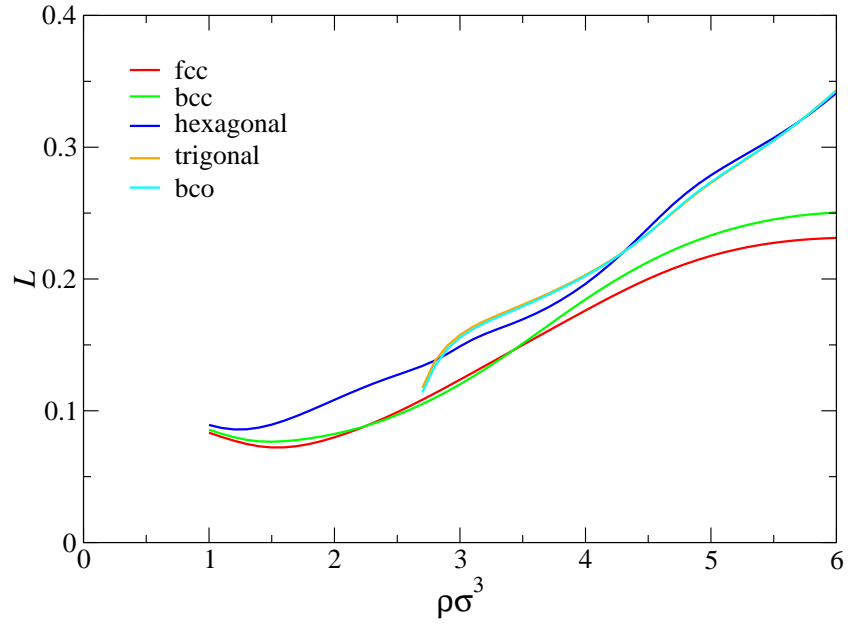


Figure 4.18: *Lindemann ratio of fcc, bcc, hexagonal, trigonal, and bco crystals of microgels with $Z = 300$ and $\sigma = 100\text{nm}$.*

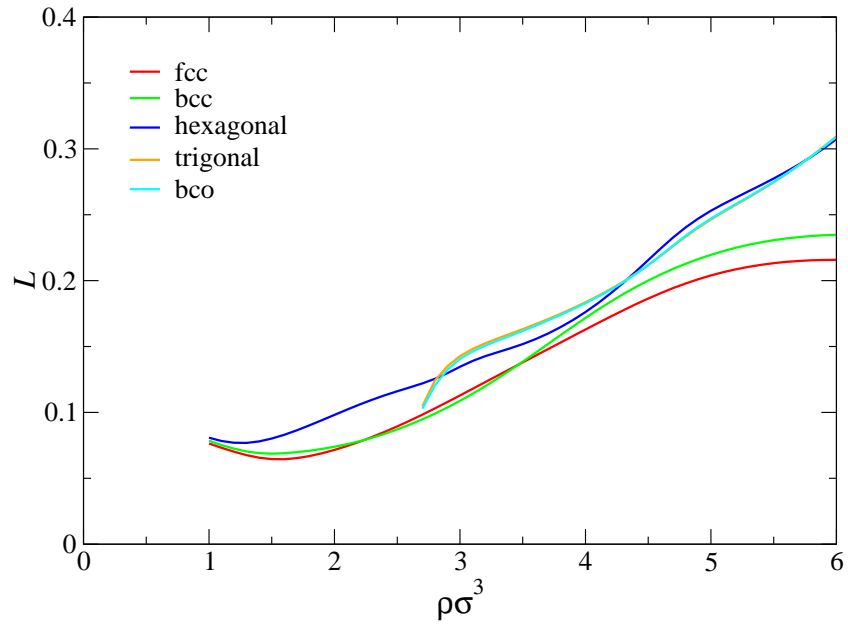


Figure 4.19: *Lindemann ratio of fcc, bcc, hexagonal, trigonal, and bco crystals of microgels with $Z = 350$ and $\sigma = 100\text{nm}$.*

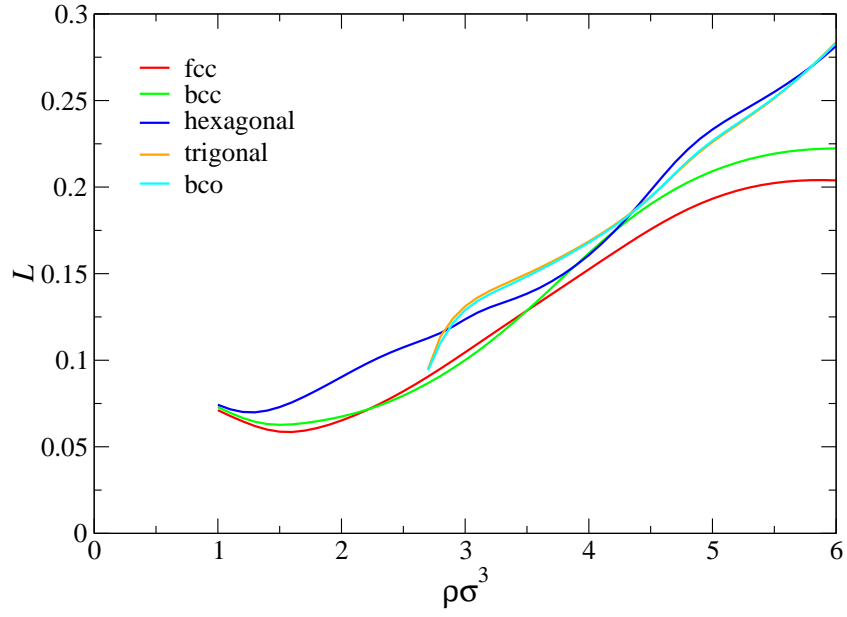


Figure 4.20: *Lindemann ratio of fcc, bcc, hexagonal, trigonal, and bco crystals of microgels with $Z = 400$ and $\sigma = 100\text{nm}$.*

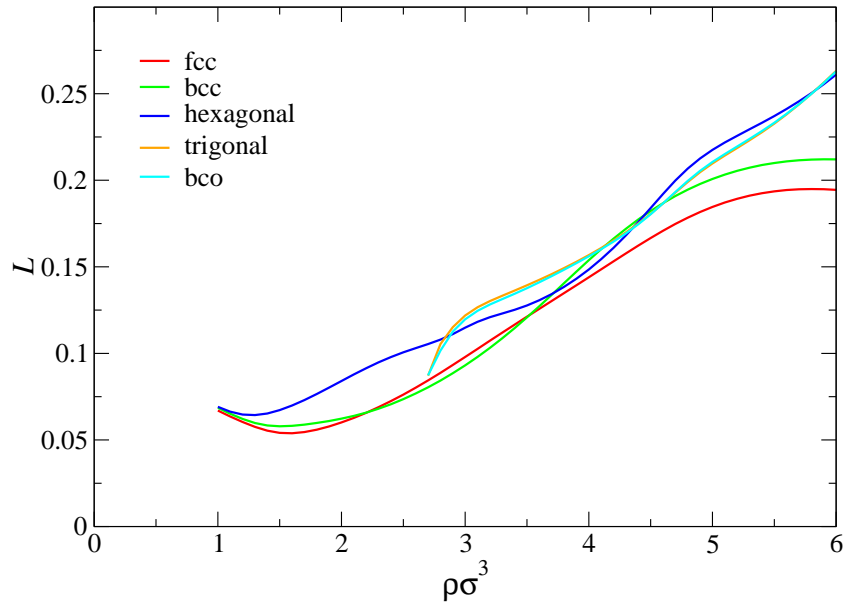


Figure 4.21: *Lindemann ratio of fcc, bcc, hexagonal, trigonal, and bco crystals of microgels with $Z = 450$ and $\sigma = 100\text{nm}$.*

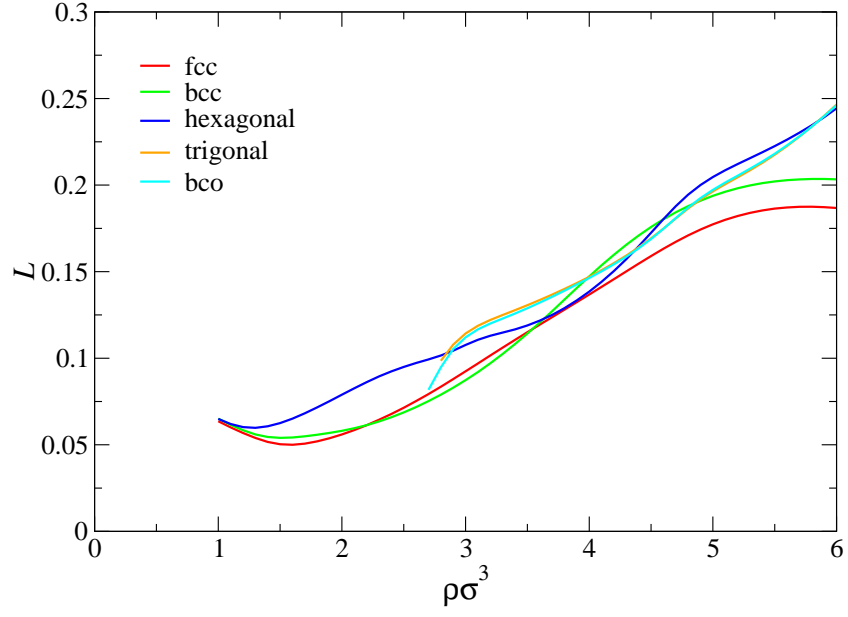


Figure 4.22: *Lindemann ratio of fcc, bcc, hexagonal, trigonal, and bco crystals of microgels with $Z = 500$ and $\sigma = 100\text{nm}$.*

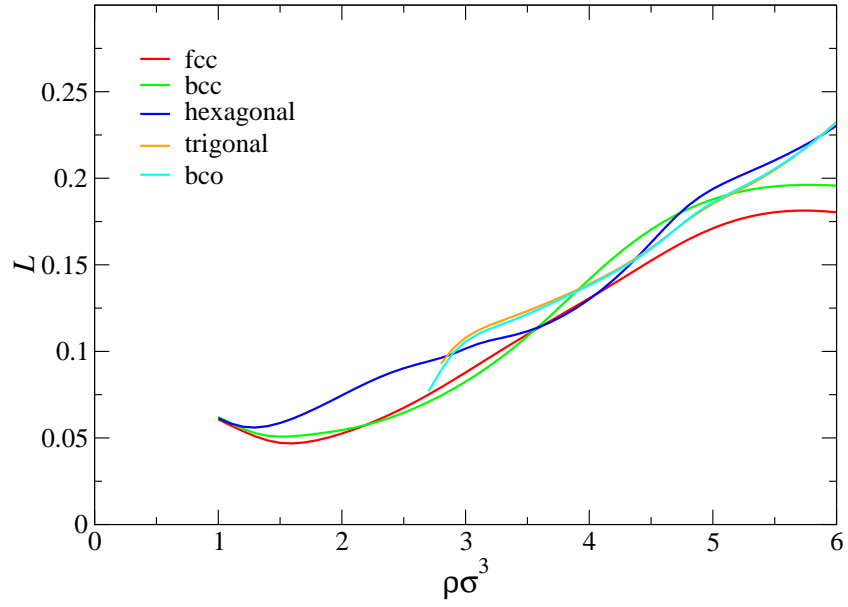


Figure 4.23: *Lindemann ratio of fcc, bcc, hexagonal, trigonal, and bco crystals of microgels with $Z = 550$ and $\sigma = 100\text{nm}$.*

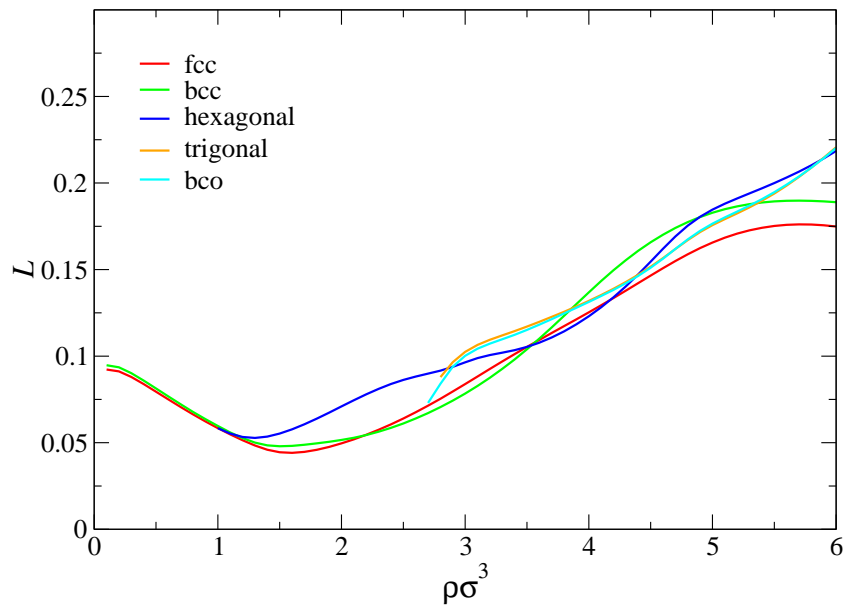


Figure 4.24: *Lindemann ratio of fcc, bcc, hexagonal, trigonal, and bco crystals of microgels with $Z = 600$ and $\sigma = 100\text{nm}$.*

4.1.2.4 Steric Interaction

The inclusion of the steric interaction (3.3) between the microgel particles will have no impact on the phase behavior for high values of Z as the interaction potential that stems from the electrostatic interactions scales with Z^2 and the maximum value of the steric interaction is limited to $\alpha \lesssim 200$. The additional repulsion from the steric interaction should stabilize the solid and decrease the value of Z where re-entrant melting occurs first. A sufficiently large value of α should lead to two separate fluid phases. The calculation of the phase diagrams shows that these effects indeed occur (see figures 4.25, 4.26, and 4.27)

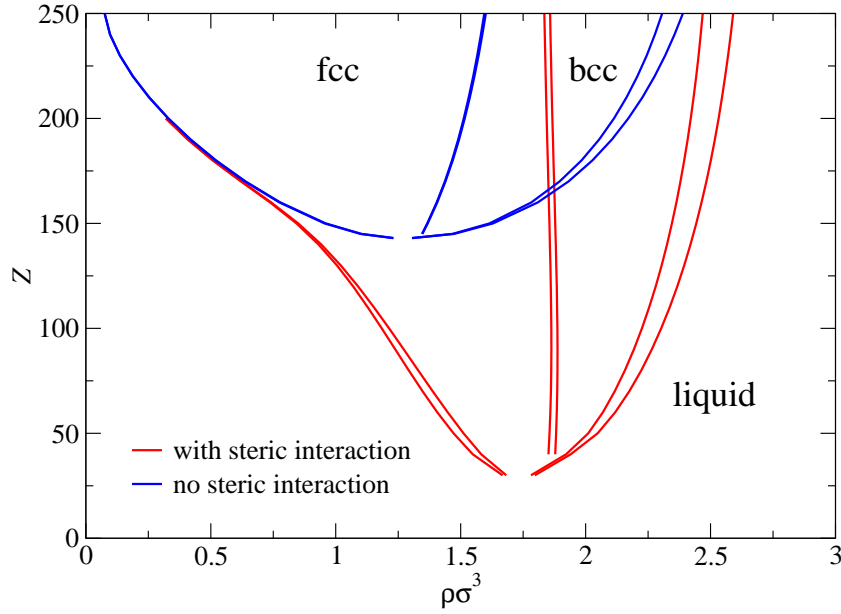


Figure 4.25: Low density part of the phase diagram of an ionic microgel (charge number Z vs. density) including steric interactions. The system parameters are $\sigma = 100nm$ and $\alpha = 50$. The properties of the liquid phase were calculated with the HNC closure.

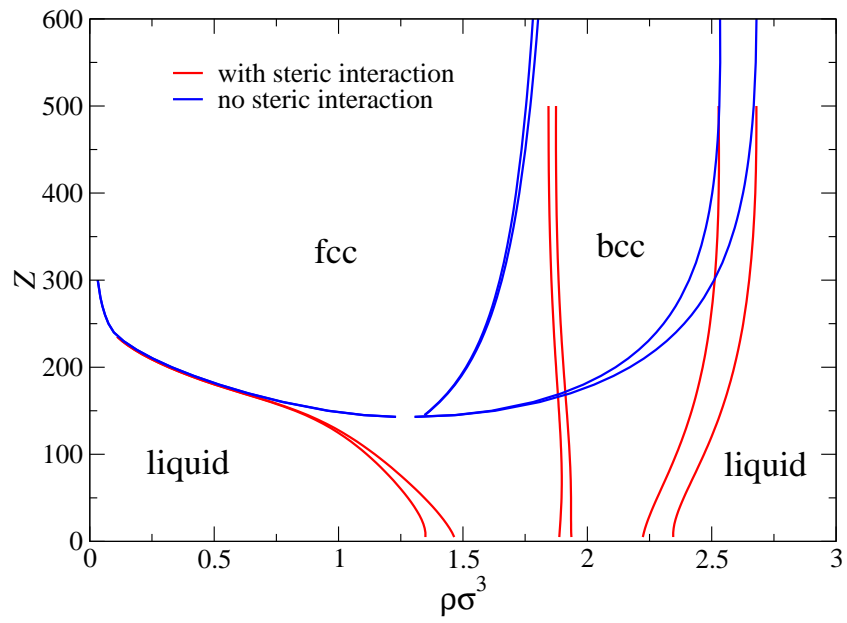


Figure 4.26: Low density part of the phase diagram of an ionic microgel (charge number Z vs. density) including steric interactions. The system parameters are $\sigma = 100\text{nm}$ and $\alpha = 70$. The properties of the liquid phase were calculated with the HNC closure.

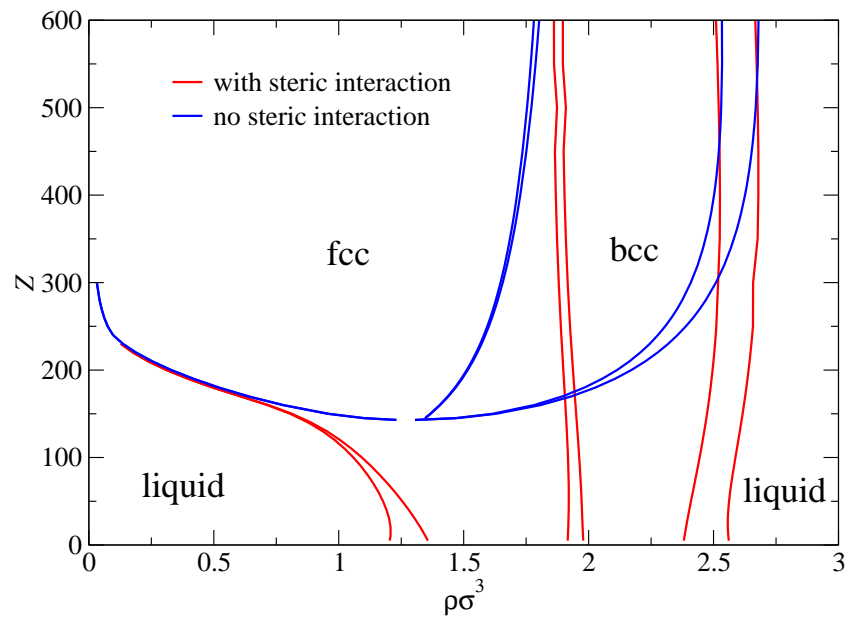


Figure 4.27: Low density part of the phase diagram of an ionic microgel (charge number Z vs. density) including steric interactions. The system parameters are $\sigma = 100nm$ and $\alpha = 100$. The properties of the liquid phase were calculated with the HNC closure.

4.2 Layer Transition

The aim of the investigations of layered systems was to study the formation of three-dimensional lattices out of a few layers as well as the transition from (n) to $(n + 1)$ layers. The constituent particles of the system were chosen to be polymers with GCM interaction potential (3.5) because the phase behavior of the bulk system is already known [49]: the stable crystal structures of the three-dimensional system are fcc and bcc. The zero-temperature solid phase diagram of the bulk system is as follows:

- fcc for $0 \leq \rho\sigma^3 < 0.1794$
- phase coexistence between fcc and bcc for $0.1794 \leq \rho\sigma^3 \leq 0.1798$
- fcc for $0.1798 < \rho\sigma^3$

Both fcc and bcc lattices can be realized as stacked two-dimensional lattices, which will be shown in the following paragraphs:

fcc lattice

- **Square:** The two-dimensional lattice is a square lattice with a lattice parameter of a and each layer is displaced by $(a/2, a/2)$. If the distance between two layers is $a/\sqrt{2}$ then the resulting three-dimensional lattice built up by an infinite number of layers is a fcc lattice with lattice constant $\sqrt{2}a$ (see figure 4.28).
- **Rectangular:** The two-dimensional lattice is a rectangular lattice with the lattice parameters a and $a/\sqrt{2}$ and each layer is displaced by half of the diagonal. If the distance between two layers is $a/\sqrt{8}$ then the resulting three-dimensional lattice built up by an infinite number of layers is a fcc lattice with lattice constant a (see figure 4.29).
- **Hexagonal:** The two-dimensional lattice is a hexagonal lattice with lattice parameter a and each layer is displaced by $(a/2, a/\sqrt{12})$. If the distance between two layers is $\sqrt{2/3}a$ then the resulting three-dimensional lattice built up by an infinite number of layers is a fcc lattice with lattice constant $\sqrt{2}a$ (see figure 4.30).

bcc lattice

- **Square:** The two-dimensional lattice is a square lattice with a lattice parameter of a and each layer is displaced by $(a/2, a/2)$. If the distance between two layers is $a/2$ then the resulting three-dimensional lattice built

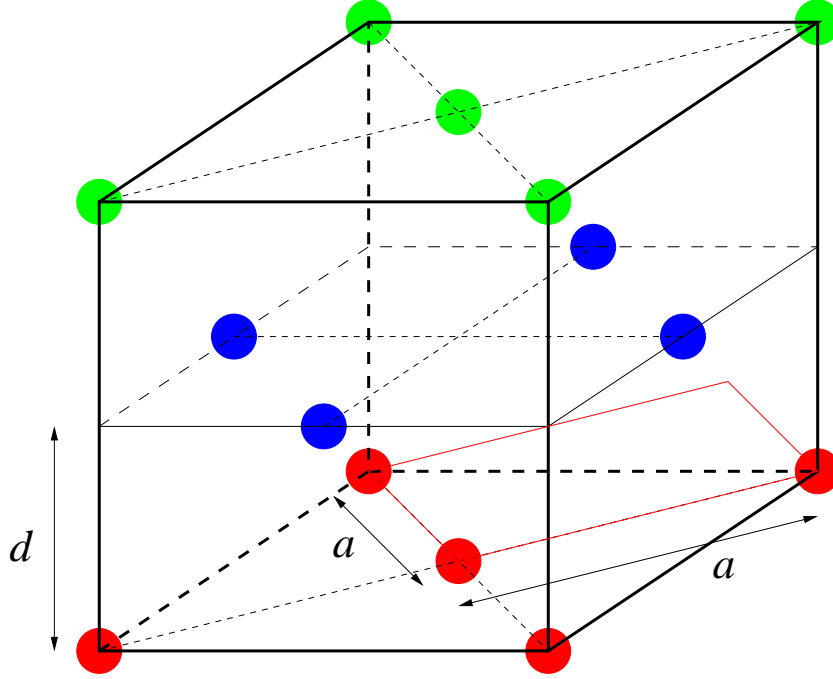


Figure 4.28: The representation of a fcc lattice by layered square lattices. The particles in different layers have different colors and the two-dimensional unit cell is drawn in red.

up by an infinite number of layers is a bcc lattice with lattice constant a (see figure 4.31).

- **Centered Rectangular:** The two-dimensional lattice is a centered rectangular lattice with lattice parameters a and $\sqrt{2}a$ and each layer is displaced by $a/\sqrt{2}$ in the direction of the longer primitive vector. If the distance between two layers is $a/\sqrt{2}$ then the resulting three-dimensional lattice built up by an infinite number of layers is a bcc lattice with lattice constant a (see figure 4.32).
- **Hexagonal:** The two-dimensional lattice is a hexagonal lattice with lattice parameter a and each layer is displaced by $(a/2, a/\sqrt{12})$. If the distance between two layers is $a/\sqrt{24}$ then the resulting three-dimensional lattice built up by an infinite number of layers is a bcc lattice with lattice constant $a/\sqrt{2}$ (see figure 4.33).

The structures that are expected are summarized in table 4.1.

The layers are assumed to be confined by hard walls which are separated by a distance D and the first and last layer are located directly in the walls (for details see 1.3.1.3). The calculations were carried out at fixed bulk number density $\rho\sigma^3$

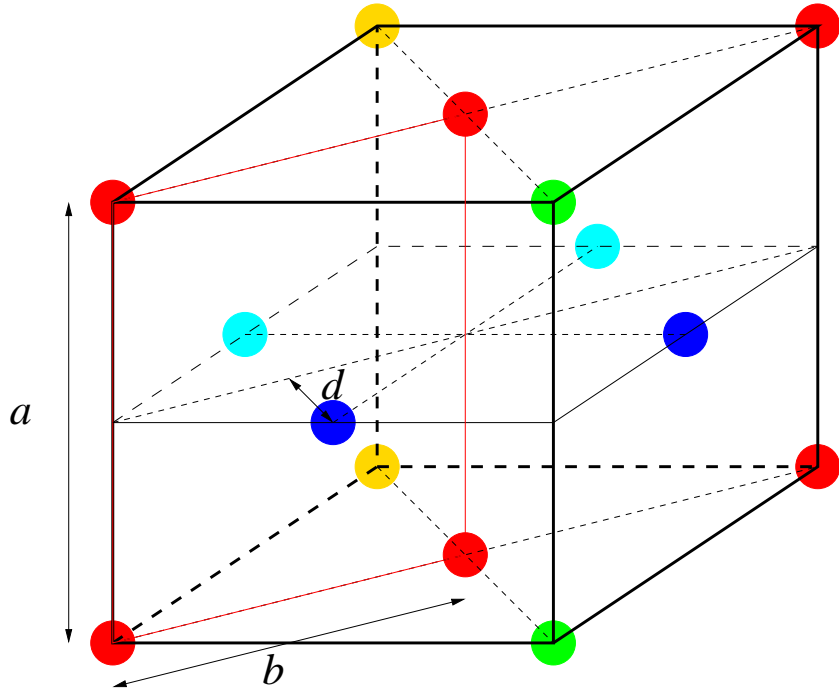


Figure 4.29: *The representation of a fcc lattice by layered rectangular lattices. The particles in different layers have different colors and the two-dimensional unit cell is drawn in red.*

and wall distance D . The wall distance was increased from σ to 10σ in intervals of $\sigma/2$. The following numbers of layers were considered: $n_l \in \{2, 3, 4, 5, 6, 7, 8\}$. The free energy was approximated via lattice sums and all results were obtained by the GA with a subsequent hill climbing search algorithm.

In the following sections the results are presented in detail for densities 0.1, 0.2, and 0.5. To identify the bulk crystal structure the layered arrangement is more similar to, the respective ratio of layer distance d to lattice constant a is calculated and compared to the values in table 4.1.

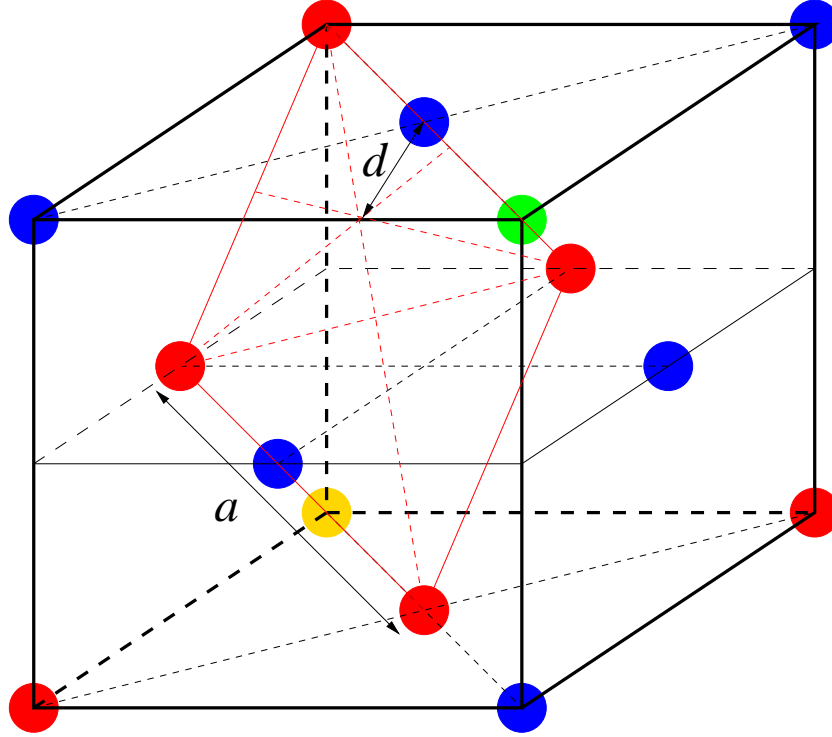


Figure 4.30: The representation of a fcc lattice by layered hexagonal lattices. The particles in different layers have different colors and the two-dimensional unit cell is drawn in red.

2-D structure	lattice parameters	layer displacement	layer distance	3-D structure
square	a	$(a/2, a/2)$	$d/a = 1/\sqrt{2} \cong 0.71$	fcc
square	a	$(a/2, a/2)$	$d/a = 1/2 = 0.5$	bcc
rectangular	$a, a/\sqrt{2}$	$(a/2, a/\sqrt{8})$	$d/a = 1/\sqrt{8} \cong 0.35$	fcc
centered rectangular	$a, \sqrt{2}a$	$(a/\sqrt{2}, 0)$	$d/a = 1/\sqrt{2} \cong 0.71$	bcc
hexagonal	a	$(a/2, a/\sqrt{12})$	$d/a = \sqrt{2/3} \cong 0.82$	fcc
hexagonal	a	$(a/2, a/\sqrt{12})$	$d/a = 1/\sqrt{24} \cong 0.20$	bcc

Table 4.1: The summary of the parameters of the expected layered arrangements.

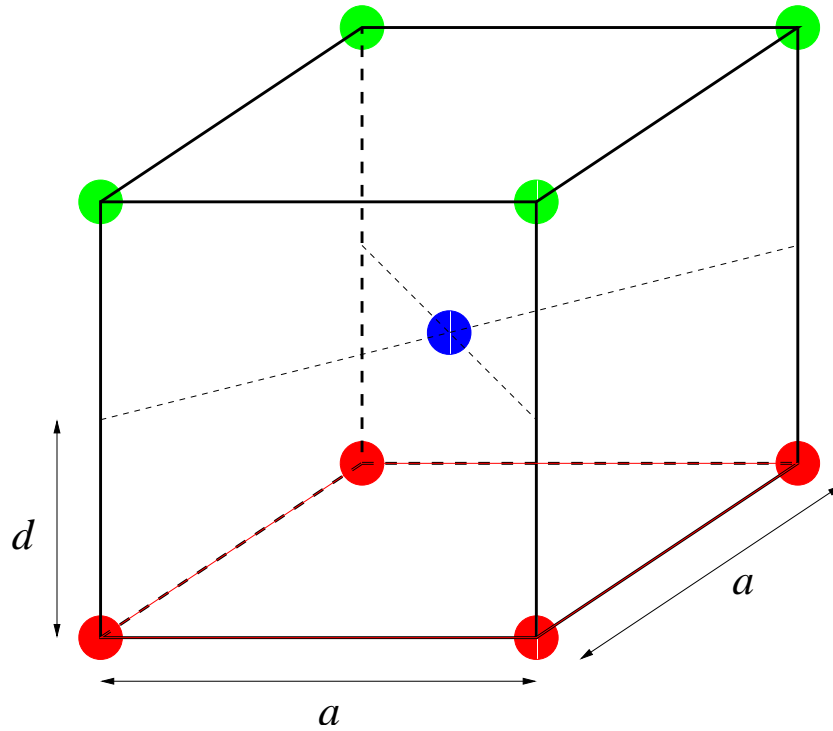


Figure 4.31: The representation of a bcc lattice by layered square lattices. The particles in different layers have different colors and the two-dimensional unit cell is drawn in red.

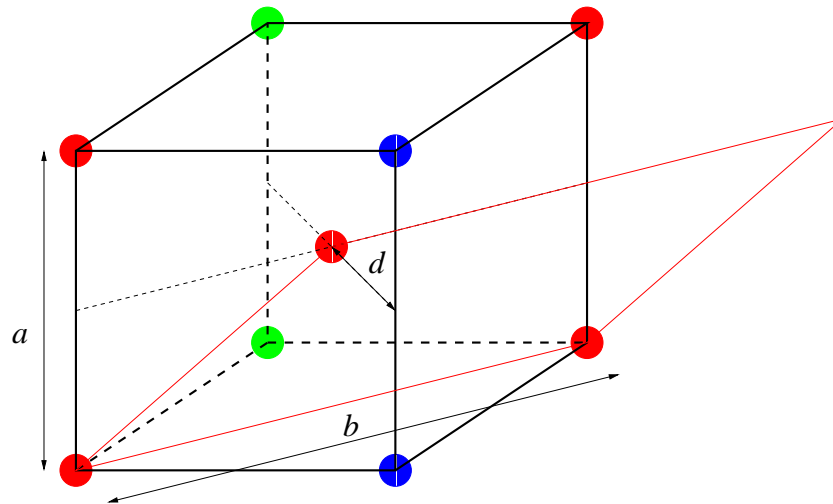


Figure 4.32: The representation of a bcc lattice by layered centered rectangular lattices. The particles in different layers have different colors and the two-dimensional unit cell is drawn in red.

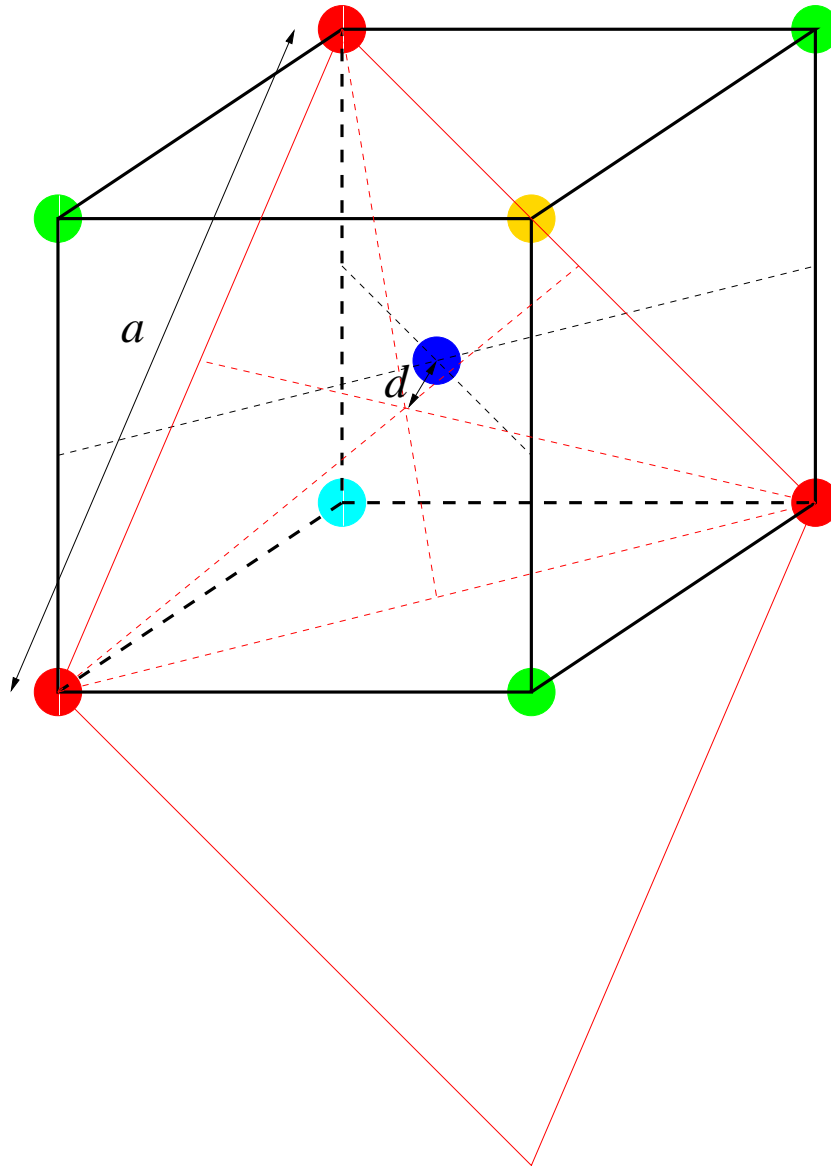


Figure 4.33: The representation of a bcc lattice by layered hexagonal lattices. The particles in different layers have different colors and the two-dimensional unit cell is drawn in red.

4.2.1 Layer transition for $\rho\sigma^3 = 0.1$

At a density of $\rho\sigma^3 = 0.1$ the bulk system freezes into a fcc lattice. The number of layers for the stable layered arrangement ranges from two (for $D = \sigma$) to six (for $D = 10\sigma$). Even though the distance between the layers are free parameters, the GA predicts that the layers are located equally spaced between the top and the bottom layer. The free energy of the layered system as a function of wall distance can be seen in figure 4.34 and the details of the layered configurations are presented in tables 4.2, 4.3, and 4.4.

At low distances $D \lesssim 3.0\sigma$ the stable layered arrangement is characterized by two layers. First the two-dimensional Bravais lattice is rectangular, which is then followed by a square lattice upon increasing wall distance. The increasing ratio of the two rectangular sides, b/a , could hint at a continuous transformation from the rectangular to the square lattice which could be verified by additional calculations. For wall distances $D \gtrsim 2.5\sigma$ the two layers are arranged in a hexagonal lattice. In all cases, the parameters of the equilibrium structures are closer to a fcc lattice than to a bcc lattice.

As the wall distance increases, the area density in the layers increases and the insertion of a new layer lowers this value. Therefore more and more layers appear in the stable arrangement. The respective stable arrangement can be seen in figure 4.34: it is the one with the lowest free energy. With two exceptions, the first two-dimensional Bravais lattice is square when the respective number is reached, then a transition to a hexagonal lattice occurs, and finally an additional layer is formed and the two-dimensional lattice is square again. The parameters of all these configurations indicate a fcc-like structure. The two exceptions are centered rectangular lattices at wall distances 6σ and 8σ . In those cases the parameters indicate a bcc-like structure.

Aside from two rogue results the layers are arranged in a fashion close to the three-dimensional lattice of the bulk system.

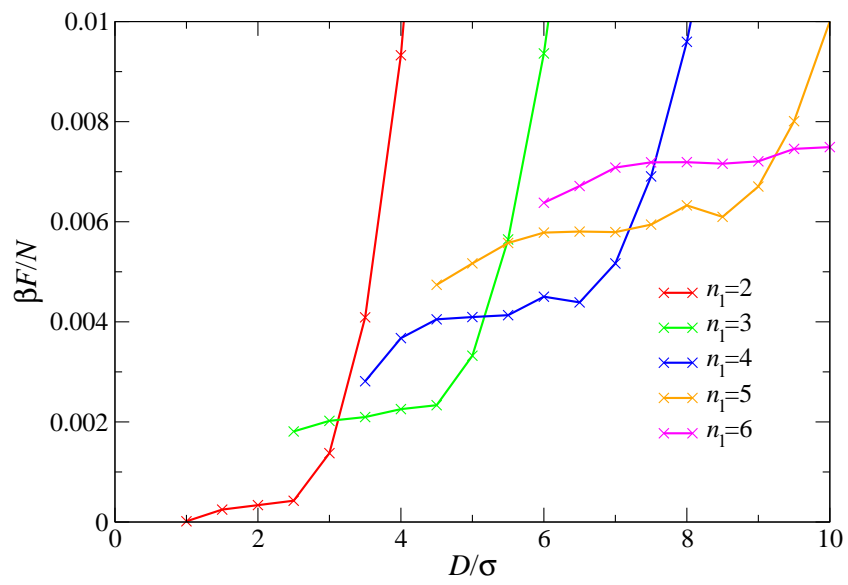


Figure 4.34: The free energy per particle $\beta F/N$ of a layered system with bulk number density $\rho\sigma^3 = 0.1$ as a function of wall distance D/σ . The different curves correspond to a different number of layers n_l . Details of the structures can be found in tables 4.2, 4.3, and 4.4.

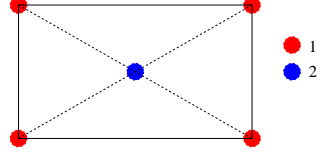
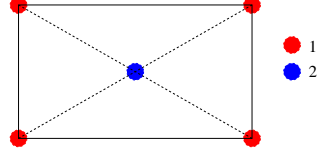
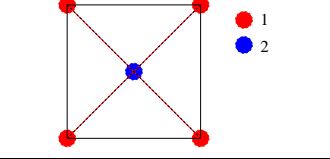
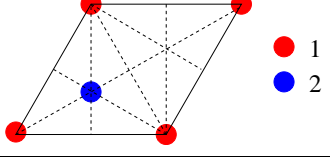
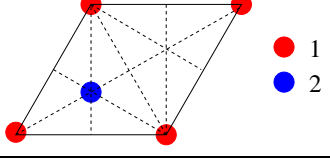
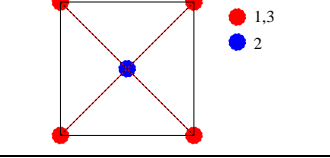
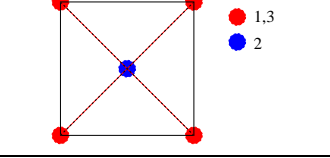
D/σ	n_l	2-D structure	layer displacement	layer distance
1.0	2	rectangular, $b/a = 0.62$		$d/a = 0.18$
1.5	2	rectangular, $b/a = 0.76$		$d/a = 0.16$
2.0	2	square, $a/\sigma = 3.16$		$d/a = 0.63$
2.5	2	hexagonal, $a/\sigma = 3.04$		$d/a = 0.82$
3.0	2	hexagonal, $a/\sigma = 2.77$		$d/a = 1.08$
3.5	3	square, $a/\sigma = 2.93$		$d/a = 0.60$
4.0	3	square, $a/\sigma = 2.74$		$d/a = 0.73$

Table 4.2: Structural details of the stable layered arrangements of a system with fixed bulk number density $\rho\sigma^3 = 0.1$. The wall distance is denoted by D , the number of layers by n_l , the distance between two layers by d , and the lattice parameters by a and b . All numerical values are rounded to two digits.

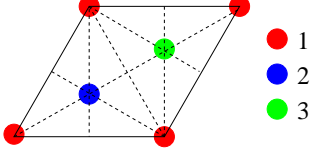
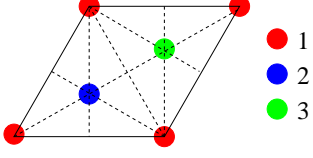
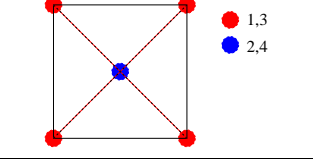
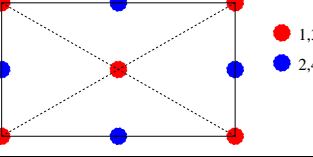
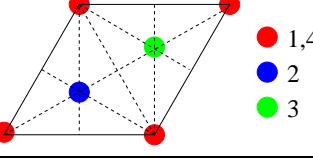
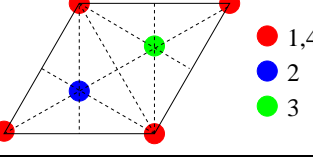
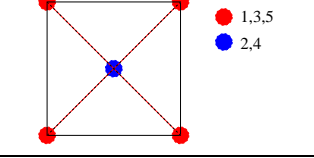
D/σ	n_l	2-D structure	layer displacement	layer distance
4.5	3	hexagonal, $a/\sigma = 2.77$		$d/a = 0.81$
5.0	3	hexagonal, $a/\sigma = 2.63$		$d/a = 0.95$
5.5	4	square, $a/\sigma = 2.70$		$d/a = 0.68$
6.0	4	centered rectangular, $b/a = 0.86$		$d/a = 0.59$
6.5	4	hexagonal, $a/\sigma = 2.67$		$d/a = 0.81$
7.0	4	hexagonal, $a/\sigma = 2.57$		$d/a = 0.91$
7.5	5	square, $a/\sigma = 2.58$		$d/a = 0.73$

Table 4.3: Structural details of the stable layered arrangements of a system with fixed bulk number density $\rho\sigma^3 = 0.1$. The wall distance is denoted by D , the number of layers by n_l , the distance between two layers by d , and the lattice parameters by a and b . All numerical values are rounded to two digits.

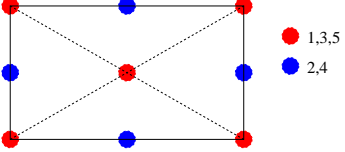
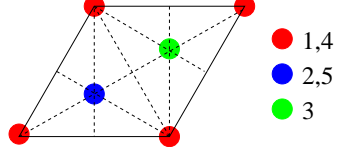
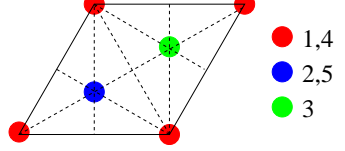
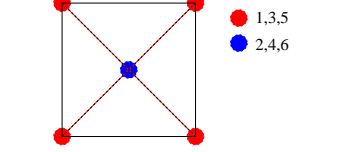
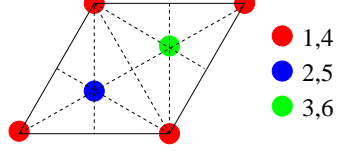
D/σ	n_l	2-D structure	layer displacement	layer distance
8.0	5	centered rectangular, $b/a = 0.75$	 <ul style="list-style-type: none"> Red: 1,3,5 Blue: 2,4 	$d/a = 0.65$
8.5	5	hexagonal, $a/\sigma = 2.61$	 <ul style="list-style-type: none"> Red: 1,4 Blue: 2,5 Green: 3 	$d/a = 0.82$
9.0	5	hexagonal, $a/\sigma = 2.53$	 <ul style="list-style-type: none"> Red: 1,4 Blue: 2,5 Green: 3 	$d/a = 0.89$
9.5	6	square, $a/\sigma = 2.51$	 <ul style="list-style-type: none"> Red: 1,3,5 Blue: 2,4,6 	$d/a = 0.76$
10.0	6	hexagonal, $a/\sigma = 2.63$	 <ul style="list-style-type: none"> Red: 1,4 Blue: 2,5 Green: 3,6 	$d/a = 0.76$

Table 4.4: *Structural details of the stable layered arrangements of a system with fixed bulk number density $\rho\sigma^3 = 0.1$. The wall distance is denoted by D , the number of layers by n_l , the distance between two layers by d , and the lattice parameters by a and b . All numerical values are rounded to two digits.*

4.2.2 Layer transition for $\rho\sigma^3 = 0.2$

The density $\rho\sigma^3 = 0.2$ represents a state that is close to the transition from fcc to bcc in the bulk system but already in the bcc region. Compared to the system at a density of $\rho\sigma^3 = 0.1$, the transitions to an increasing number of layers is shifted to a lower wall distance and at high wall distances, seven layers start to appear. Again, the GA predicts that the layers are separated by an equal distance to each other. The free energy of the layered system as a function of wall distance is depicted in figure 4.35 and the details of the layered configurations are specified in tables 4.5, 4.6, and 4.7.

The sequence of two-dimensional Bravais lattices for a fixed number of layers is similar to the behavior at $\rho\sigma^3 = 0.1$: first a stable square lattice, then a hexagonal lattice, and then a transition to a square lattice with one additional lattice. All configurations are fcc-like. The exceptions are centered rectangular lattices for $D = 6\sigma$ and 6.5σ with $n_l = 5$ which corresponds to a bcc-like arrangement.

In this case the majority of the configurations of the layers do not correspond to the crystal structure of the bulk system but the proximity to the phase transition could be responsible for this effect.

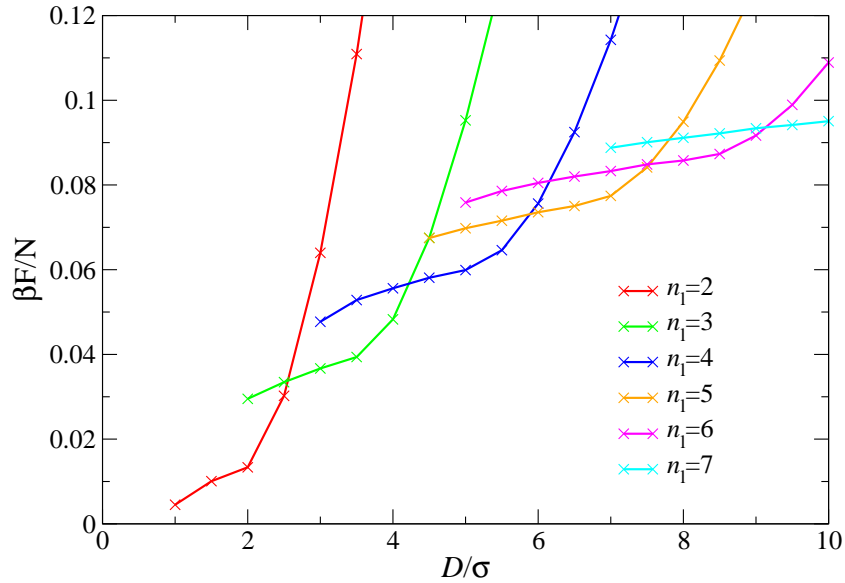


Figure 4.35: The free energy per particle $\beta F/N$ of a layered system with bulk number density $\rho\sigma^3 = 0.2$ as a function of wall distance D/σ . The different curves correspond to a different number of layers n_l . Details of the structures can be found in tables 4.5, 4.6, and 4.7.

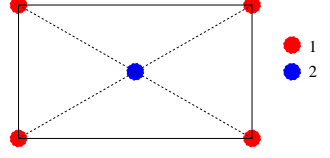
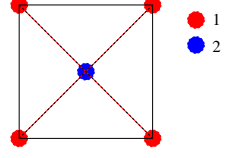
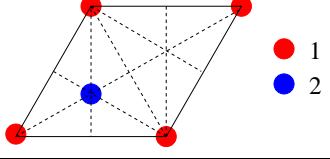
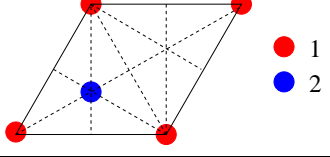
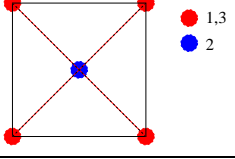
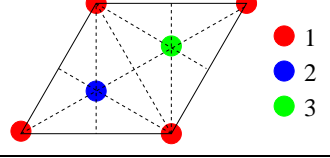
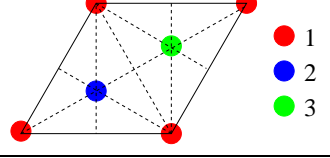
D/σ	n_l	2-D structure	layer displacement	layer distance
1.0	2	rectangular, $b/a = 0.70$		$d/a = 0.26$
1.5	2	square, $a/\sigma = 2.58$		$d/a = 0.58$
2.0	2	hexagonal, $a/\sigma = 2.40$		$d/a = 0.83$
2.5	2	hexagonal, $a/\sigma = 2.15$		$d/a = 1.16$
3.0	3	square, $a/\sigma = 2.24$		$d/a = 0.67$
3.5	3	hexagonal, $a/\sigma = 2.22$		$d/a = 0.79$
4.0	3	hexagonal, $a/\sigma = 2.08$		$d/a = 0.96$

Table 4.5: Structural details of the stable layered arrangements of a system with fixed bulk number density $\rho\sigma^3 = 0.2$. The wall distance is denoted by D , the number of layers by n_l , the distance between two layers by d , and the lattice parameters by a and b . All numerical values are rounded to two digits.

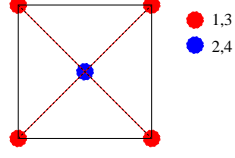
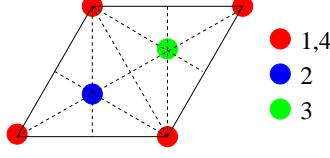
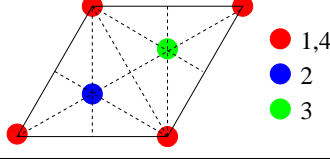
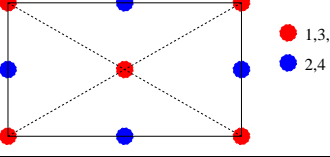
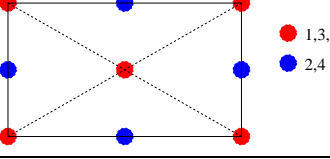
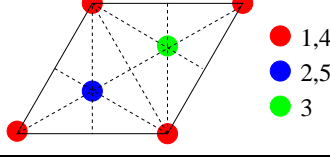
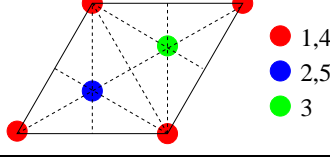
D/σ	n_l	2-D structure	layer displacement	layer distance
4.5	4	square, $a/\sigma = 2.1$		$d/a = 0.71$
5.0	4	hexagonal, $a/\sigma = 2.15$		$d/a = 0.78$
5.5	4	hexagonal, $a/\sigma = 2.05$		$d/a = 0.89$
6.0	5	centered rectangular, $b/a = 0.89$		$d/a = 0.55$
6.5	5	centered rectangular, $b/a = 0.68$		$d/a = 0.71$
7.0	5	hexagonal, $a/\sigma = 2.03$		$d/a = 0.86$
7.5	5	hexagonal, $a/\sigma = 1.96$		$d/a = 0.96$

Table 4.6: Structural details of the stable layered arrangements of a system with fixed bulk number density $\rho\sigma^3 = 0.2$. The wall distance is denoted by D , the number of layers by n_l , the distance between two layers by d , and the lattice parameters by a and b . All numerical values are rounded to two digits.

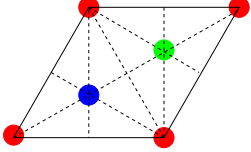
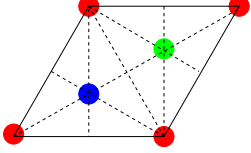
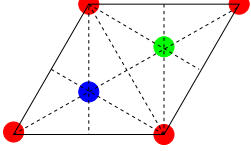
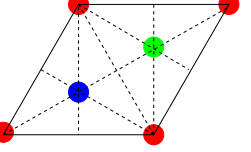
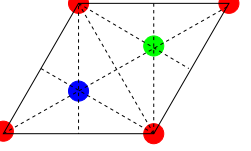
D/σ	n_l	2-D structure	layer displacement	layer distance
8.0	6	hexagonal, $a/\sigma = 2.08$	 <ul style="list-style-type: none"> ● 1,4 ● 2,5 ● 3,6 	$d/a = 0.77$
8.5	6	hexagonal, $a/\sigma = 2.02$	 <ul style="list-style-type: none"> ● 1,4 ● 2,5 ● 3,6 	$d/a = 0.84$
9.0	6	hexagonal, $a/\sigma = 1.96$	 <ul style="list-style-type: none"> ● 1,4 ● 2,5 ● 3,6 	$d/a = 0.92$
9.5	7	hexagonal, $a/\sigma = 2.06$	 <ul style="list-style-type: none"> ● 1,4,7 ● 2,5 ● 3,6 	$d/a = 0.77$
10.0	7	hexagonal, $a/\sigma = 2.01$	 <ul style="list-style-type: none"> ● 1,4,7 ● 2,5 ● 3,6 	$d/a = 0.83$

Table 4.7: Structural details of the stable layered arrangements of a system with fixed bulk number density $\rho\sigma^3 = 0.2$. The wall distance is denoted by D , the number of layers by n_l , the distance between two layers by d , and the lattice parameters by a and b . All numerical values are rounded to two digits.

4.2.3 Layer transition for $\rho\sigma^3 = 0.5$

The stable crystal structure of the bulk system is bcc at a density of $\rho\sigma^3 = 0.5$. The maximum number of layers in the stable configuration is eight which occurs at a wall distance $D \gtrsim 9.5\sigma$. The GA predicts that the layers are located evenly distributed between the top and the bottom layer as in the two previous cases. The free energy of the layered system as a function of wall distance can be seen in figure 4.36 and the details of the layered configurations are presented in tables 4.8, 4.9, and 4.10.

At a wall distance of $D = \sigma$ the two layers are arranged in a square lattice which corresponds to a bcc-like configuration. With increasing wall distance the lattice in the two layers becomes hexagonal. This arrangement resembles more a fcc lattice, similar to the two previous cases. For three layers and more, the sequence of structures is throughout as follows: (n_l) layers with a centered rectangular lattice, then (n_l) layers with a hexagonal lattice, and then a transition to $(n_l + 1)$ layers with a centered rectangular lattice. In some cases one of the two configurations is missing which is likely due to the step size of $\sigma/2$ between two subsequent cases studied, which might be too coarse in these cases. The arrangements with the square lattice and the centered rectangular lattices are bcc-like while the ones with hexagonal lattices are fcc-like.

Although the chosen density value leads to a bcc crystal in the bulk phase, the layered system is arranged both fcc- and bcc-like.

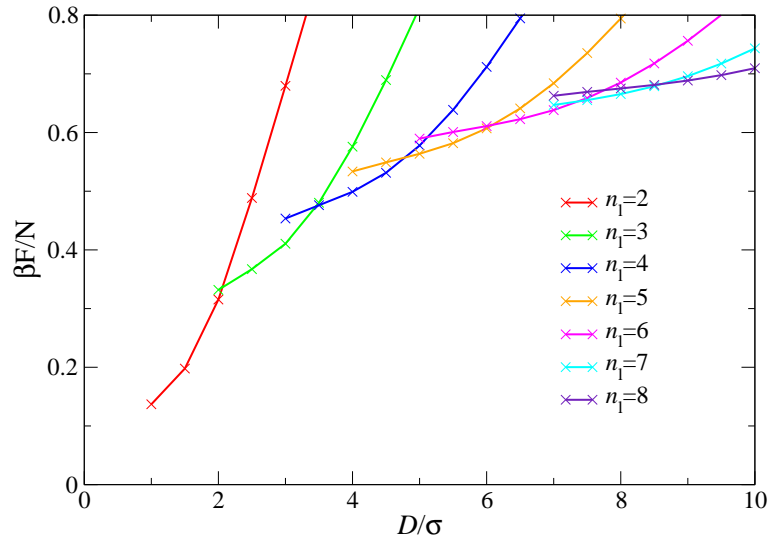


Figure 4.36: The free energy per particle $\beta F/N$ of a layered system with bulk number density $\rho\sigma^3 = 0.5$ as a function of wall distance D/σ . The different curves correspond to a different number of layers n_l . Details of the structures can be found in tables 4.8, 4.9, and 4.10.

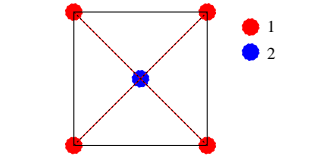
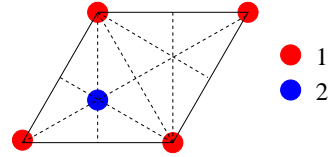
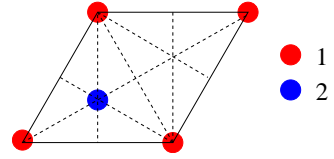
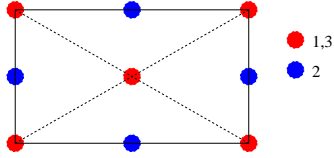
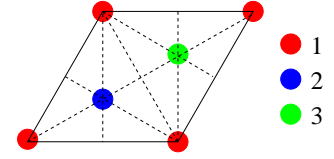
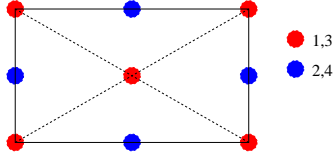
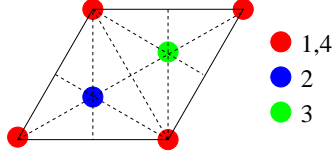
D/σ	n_l	2-D structure	layer displacement	layer distance
1.0	2	square, $a/\sigma = 2.00$		$d/a = 0.50$
1.5	2	hexagonal, $a/\sigma = 1.75$		$d/a = 0.85$
2.0	2	hexagonal, $a/\sigma = 1.52$		$d/a = 1.32$
2.5	3	centered rectangular, $b/a = 0.67$		$d/a = 0.70$
3.0	3	hexagonal, $a/\sigma = 1.52$		$d/a = 0.99$
3.5	4	centered rectangular, $b/a = 0.70$		$d/a = 0.65$
4.0	4	hexagonal, $a/\sigma = 1.52$		$d/a = 0.88$

Table 4.8: Structural details of the stable layered arrangements of a system with fixed bulk number density $\rho\sigma^3 = 0.5$. The wall distance is denoted by D , the number of layers by n_l , the distance between two layers by d , and the lattice parameters by a and b . All numerical values are rounded to two digits.

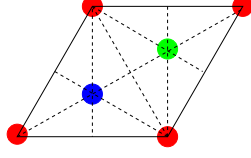
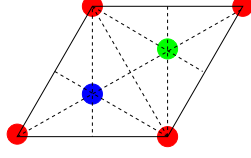
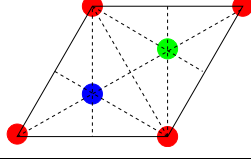
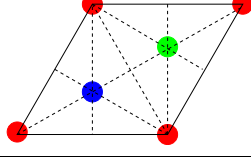
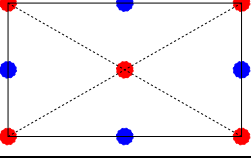
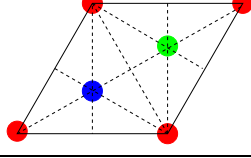
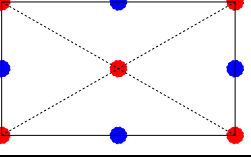
D/σ	n_l	2-D structure	layer displacement	layer distance
4.5	4	hexagonal, $a/\sigma = 1.43$	 <ul style="list-style-type: none"> ● 1,4 ● 2 ● 3 	$d/a = 1.05$
5.0	5	hexagonal, $a/\sigma = 1.52$	 <ul style="list-style-type: none"> ● 1,4 ● 2,5 ● 3 	$d/a = 0.82$
5.5	5	hexagonal, $a/\sigma = 1.45$	 <ul style="list-style-type: none"> ● 1,4 ● 2,5 ● 3 	$d/a = 0.95$
6.0	5	hexagonal, $a/\sigma = 1.39$	 <ul style="list-style-type: none"> ● 1,4 ● 2,5 ● 3 	$d/a = 1.08$
6.5	6	centered rectangular, $b/a = 0.64$	 <ul style="list-style-type: none"> ● 1,3,5 ● 2,4,6 	$d/a = 0.85$
7.0	6	hexagonal, $a/\sigma = 1.41$	 <ul style="list-style-type: none"> ● 1,4 ● 2,5 ● 3,6 	$d/a = 1.00$
7.5	7	centered rectangular, $b/a = 0.65$	 <ul style="list-style-type: none"> ● 1,3,5,7 ● 2,4,6 	$d/a = 0.80$

Table 4.9: Structural details of the stable layered arrangements of a system with fixed bulk number density $\rho\sigma^3 = 0.5$. The wall distance is denoted by D , the number of layers by n_l , the distance between two layers by d , and the lattice parameters by a and b . All numerical values are rounded to two digits.

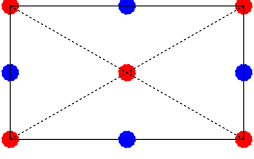
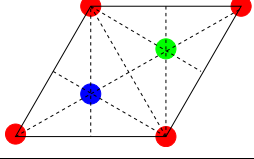
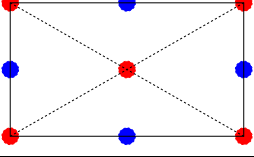
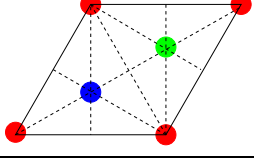
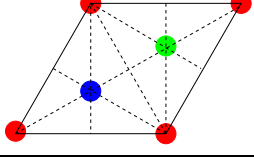
D/σ	n_l	2-D structure	layer displacement	layer distance
8.0	7	centered rectangular, $b/a = 0.63$	 <ul style="list-style-type: none"> ● 1,3,5,7 ● 2,4,6 	$d/a = 0.90$
8.5	7	hexagonal, $a/\sigma = 1.38$	 <ul style="list-style-type: none"> ● 1,4,7 ● 2,5 ● 3,6 	$d/a = 1.03$
9.0	8	centered rectangular, $b/a = 0.64$	 <ul style="list-style-type: none"> ● 1,3,5,7 ● 2,4,6,8 	$d/a = 0.85$
9.5	9	hexagonal, $a/\sigma = 1.39$	 <ul style="list-style-type: none"> ● 1,4,7 ● 2,5,8 ● 3,6 	$d/a = 0.97$
10.0	9	hexagonal, $a/\sigma = 1.36$	 <ul style="list-style-type: none"> ● 1,4,7 ● 2,5,8 ● 3,6 	$d/a = 1.05$

Table 4.10: *Structural details of the stable layered arrangements of a system with fixed bulk number density $\rho\sigma^3 = 0.5$. The wall distance is denoted by D , the number of layers by n_l , the distance between two layers by d , and the lattice parameters by a and b . All numerical values are rounded to two digits.*

4.2.4 Summary

The arrangement of the particles in the layers is influenced by the stable bulk crystal structure but not completely dominated by it. This could be due to the small difference in the free energy between the fcc and the bcc lattice in the bulk phase (see figure 4.37) and the effects of the confinement even at large wall distances. The typical sequence at low bulk densities - (n_l) layers of square

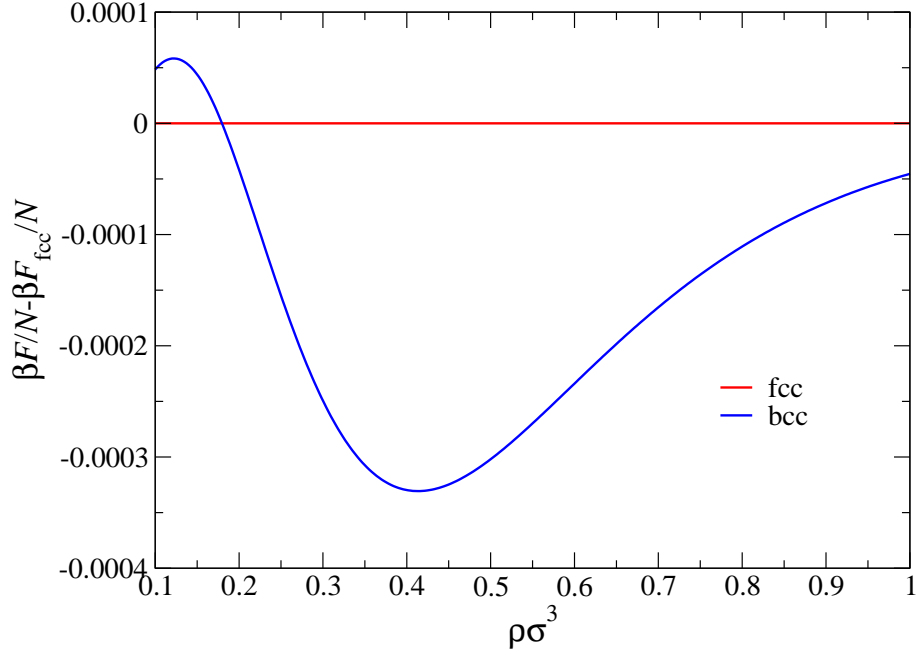


Figure 4.37: *The difference of the free energy per particle between a fcc and a bcc lattice for a system interacting via the GCM. The free energy was approximated by lattice sums.*

lattices, (n_l) layers of hexagonal lattices, and $(n_l + 1)$ layers of square lattices - was also found experimentally for a confined system of polystyrene particles [54], that freeze into a fcc crystal without confinement. The centered rectangular lattices that occur at higher densities have also been found in simulations [55, 56] and experiments [57]. The prism shaped arrays that were observed in [57] can not occur in the calculations performed here because these phases can not be described the parametrization used here, i.e. by layers that have the same two-dimensional structure.

Even though it is encouraging that the calculations yield results that have already been observed in simulations and experiments, a quantitative comparison requires the following improvements to the model used here:

- A more sophisticated model for the calculation of the free energy of the layered systems is required.

- A system where the free energy difference between a fcc and a bcc is larger will certainly lead to a more pronounced difference in the sequence of two-dimensional lattices in the bcc-region.
- A modified parametrization of the layered structures that includes also prism phases would make it possible for these phases to appear in the phase diagrams. This could be achieved by introducing basis particles that can have (small) component perpendicular to the layer.

All these improvements should lead to more specific predictions and also allow a more direct comparison to experiments.

4.3 Clustering

Soft systems can show two different scenarios upon compression [58]: re-entrant melting and clustering. A liquid that shows re-entrant melting freezes when compressed but melts again if the density reaches a certain threshold. Systems that cluster undergo a *clustering transition* where *clusters* of particles are formed in which the particles are located nearly on top of each other. This effect manifests itself in a pronounced peak at $r = 0$ in the radial distribution function $g(r)$ (see figure 4.38).

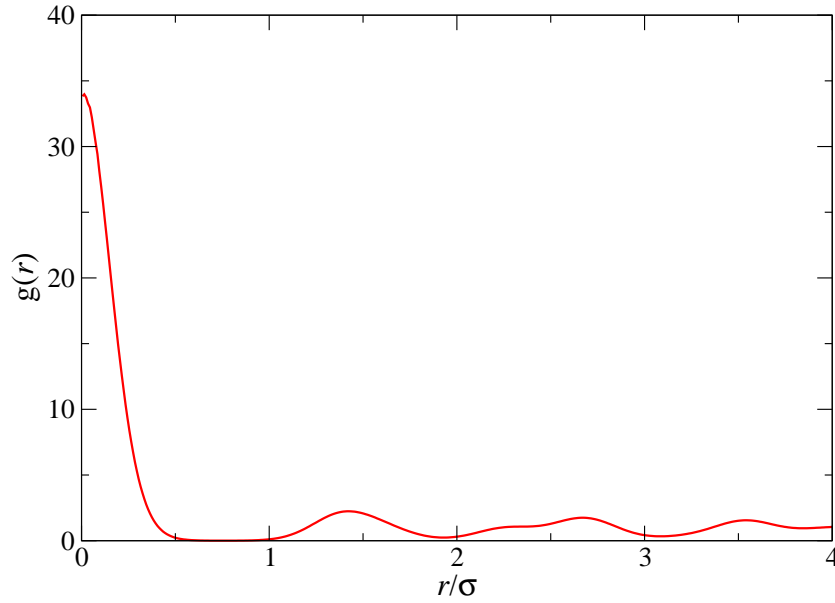


Figure 4.38: *Radial distribution function $g(r)$ of a system with $\rho\sigma^3 = 9$, and $T^* = 1$. The particles interact via the potential of the generalized Gaussian core model, equation (3.6), with index 4. The correlation functions were obtained by a canonical MC simulation with 4664 particles. The diameter of the particles is denoted by σ . The data were kindly provided by B.M. Mladek.*

Based on a mean field picture it has been shown that the Fourier transform $\tilde{\Phi}(k)$ of the interaction potential $\Phi(r)$ determines which of the two scenarios is realized [58]:

- If $\tilde{\Phi}(k)$ is positive for all k , then the system shows re-entrant melting (Q^+ -class).
- If $\tilde{\Phi}(k)$ attains negative values, then the system shows clustering (Q^\pm -class).

The number of particles in a cluster is called *cluster size* n_c and is predicted to scale linearly with the density [58]:

$$n_c = \zeta\rho.$$

In non-clustered crystals the lattice constant l scales with $1/\sqrt[3]{\rho}$, while it is independent of the density in clustered crystals:

$$l \propto \sqrt[3]{V} = \sqrt[3]{\frac{N}{\rho}} \propto \sqrt[3]{\frac{n_c}{\rho}} = \sqrt[3]{\zeta} = \text{const.}$$

The lattice constant of clustered crystals is uniquely determined by the functional form of the interaction potential alone.

According to the criterion above the generalized Gaussian core model shows re-entrant melting for $n \leq 2$ and clustering for $n > 2$ [59]. To find the ground

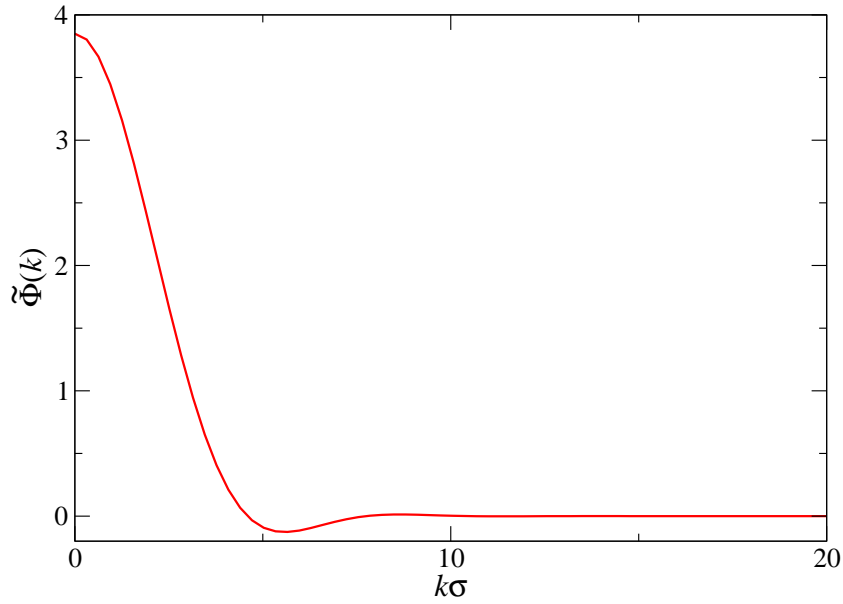


Figure 4.39: *Fourier transform of the interaction potential of the GGCM with index 4 as a function of wave vector k . The negative contributions indicate that this system should show clustering. The diameter of the particles is denoted by σ .*

state for the clustered crystal structures, calculations were done with the GA at $T = 0$. The interaction potential was that of the GGCM with varying index n . The cluster size n_c was encoded in the individual and crystal structures with one and two basis particles were considered. The free energy was calculated via lattice sums (see section 2.1.1) and fitness function (1.10) was used.

The resulting crystal structures were either bcc or fcc with the transition between those two structures occurring near index $n \cong 3$ (see figure 4.40). Similar to the star polymer and microgel case the behavior of the GA near the phase transition was rather unreliable. The GA was able to predict the expected linear dependence of the cluster size on the density ρ for all values of n (see figure 4.41). The slope of these curves decreases with increasing n .

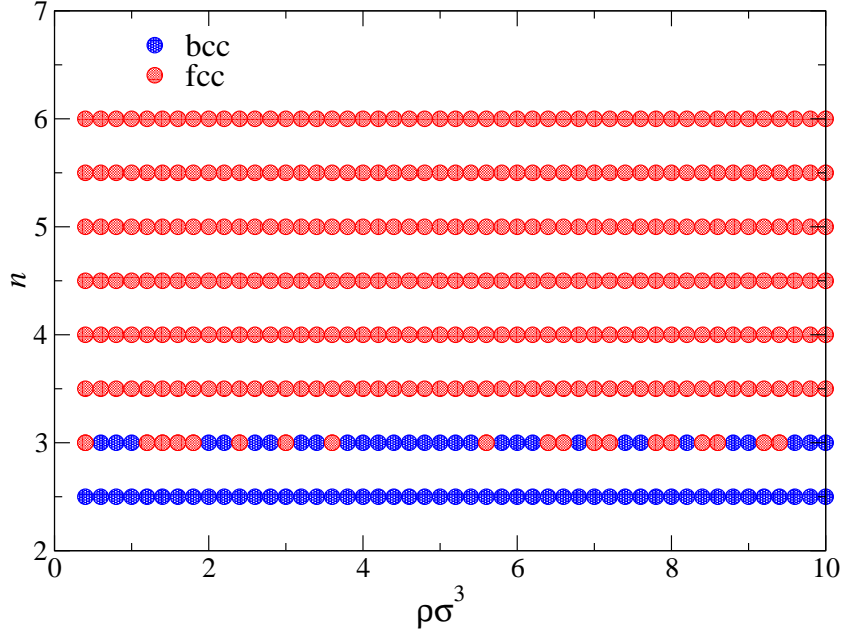


Figure 4.40: Zero-temperature phase diagram of the GGCM (index n vs. density) calculated with a genetic algorithm including clustering. The symbols denote the respective stable crystal structure.

Based on the knowledge of the ground state crystal structures, calculations at $T > 0$ can be performed using bcc and fcc structures as candidates. The free energy of the solid structures was calculated with a mean field density functional theory (DFT). The particles are assumed to be located according to a Gaussian distribution around the cluster centers, where the density of the particles has the form

$$\rho(\mathbf{r}) = n_c \left(\frac{\alpha}{\pi} \right)^{3/2} \sum_{\{\mathbf{R}\}} e^{-\alpha(\mathbf{r}-\mathbf{R})^2} = n_c \tilde{\rho}(\mathbf{r}); \quad (4.1)$$

α is the localization parameter of the Gaussian and $\{\mathbf{R}\}$ denotes the set of positions of the N_c centers of the clusters in the crystal. The excess part of the free energy is given by equation (2.12) and the ideal contribution to the free energy is obtained by evaluating

$$\begin{aligned} F^{\text{id}}/N &= \frac{1}{N} \int d\mathbf{r} \rho(\mathbf{r}) [\log \rho(\mathbf{r}) - 1] \\ &= \frac{1}{N_c n_c} \int d\mathbf{r} n_c \tilde{\rho}(\mathbf{r}) [\log(n_c \tilde{\rho}(\mathbf{r})) - 1] \\ &= \log n_c \underbrace{\frac{1}{N_c} \int d\mathbf{r} \tilde{\rho}(\mathbf{r})}_{=1} + \frac{1}{N_c} \int d\mathbf{r} [\log \tilde{\rho}(\mathbf{r}) - 1]. \end{aligned}$$

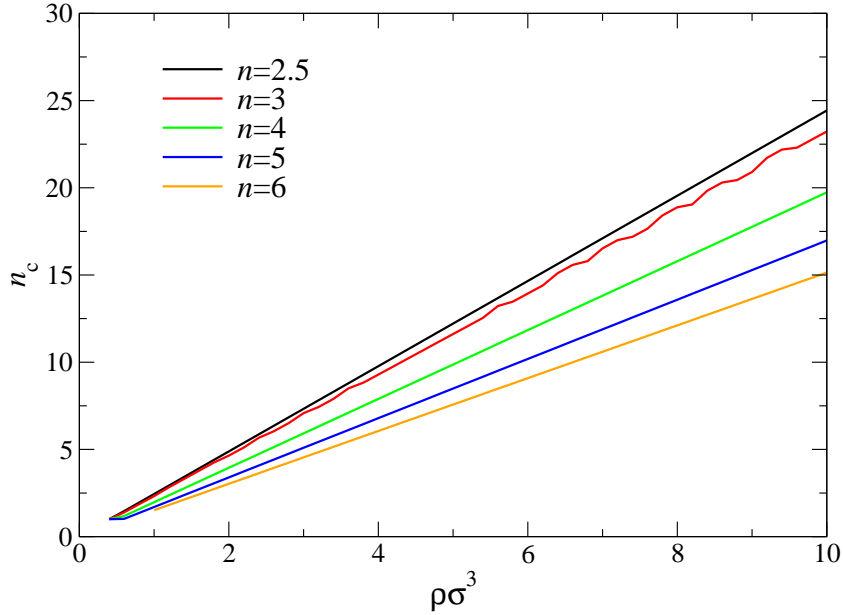


Figure 4.41: The cluster size n_c as a function of density for different n -values of the crystals in figure 4.40 predicted by the GA for the GGCM- n potential.

The last term can be approximated by

$$\frac{1}{N_c} \int d\mathbf{r} [\log \tilde{\rho}(\mathbf{r}) - 1] \cong \frac{3}{2} \log \frac{\alpha}{\pi} - \frac{3}{2}$$

if the Gaussians (4.1) do not overlap, which is fulfilled for $\alpha \gtrsim 50$. For lower values of α this expression has to be calculated numerically. The minimum of the free energy both with respect to the cluster size n_c and the localization parameter α defines the parameters of the equilibrium state at a given density and temperature (see figure 4.42). A lower bound of 1 for the cluster size was introduced due to physical reasons and a lower bound of 10 for the localization parameter α had to be used as for such a weak localization one can hardly consider the system to be solid. Some of the results are influenced by this choice as can be seen at low densities in the figures below.

To obtain an estimate of the transition density from the liquid to the clustered crystal, the free energy of the liquid was calculated with the MSA closure. Although the distribution functions can have unphysical values for high densities [59] the results in the region where the transition occurs are not affected by this deficiency. The error stems from the fact that $\tilde{h}(k)$, the Fourier transform of $h(r)$, is divergent and in the transformation into real space numerical errors occur. These numerical errors manifest themselves in large jumps in the free energy as a function of the density.

The following calculations were carried out: the free energy of a clustered fcc

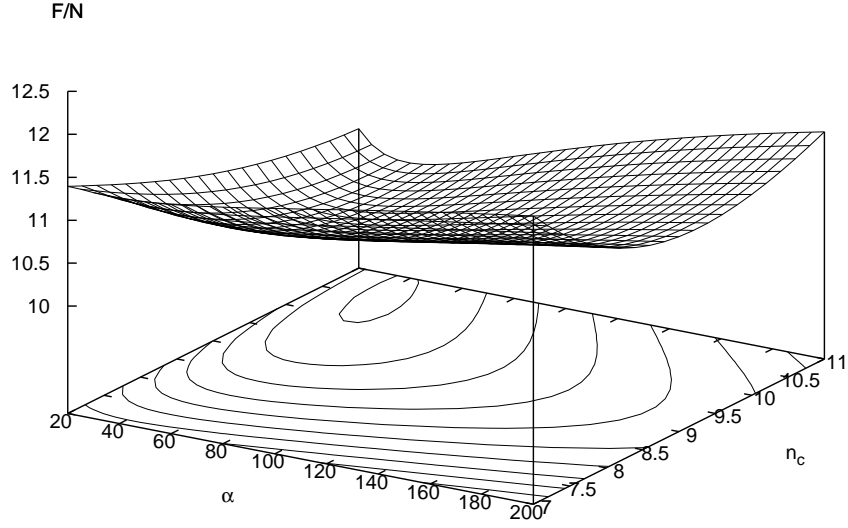


Figure 4.42: The free energy per particle F/N as a function of cluster size n_c and localization parameter α for clustered fcc crystal with density $\rho\sigma^3 = 6$. The particles interact via a GGCM with index 6 and $\varepsilon = 1$. Contour lines are indicated in the (α, n_c) -plane. The distance of the contour lines is 0.2 and the inner line refers to a free energy value of 10.1.

crystal, a clustered bcc crystal, and the liquid phase were computed, as well as the cluster size n_c and the localization parameter α of the two crystal structures. The indices $n \in \{4, 7, 10\}$ and the pre-factors $\varepsilon \in \{1, 2, 10\}$ were considered for the potential (3.6). The results are depicted in figures 4.43 to 4.57. The insets in the figures show the free energy difference of the three competing phases close to the phase transitions.

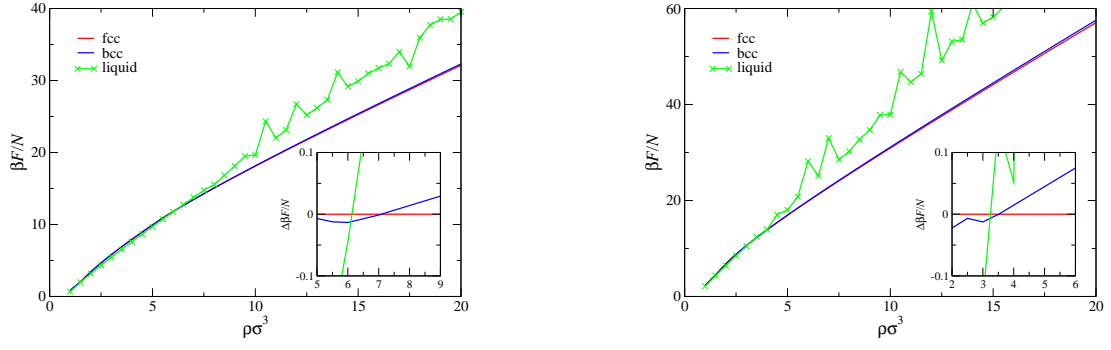


Figure 4.43: **left:** Free energy of a GGCM-system with $n = 4$ and $\varepsilon = 1$ calculated with DFT for the solid phases and the MSA closure for the liquid phase. **right:** The same for $\varepsilon = 2$.

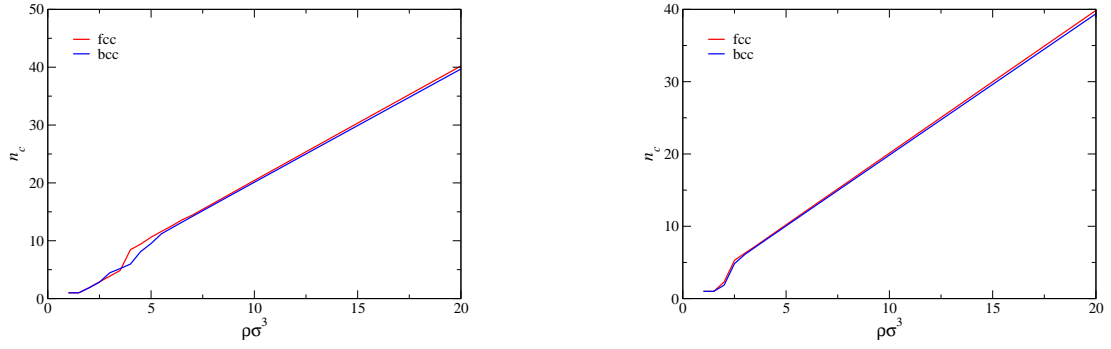


Figure 4.44: The cluster size n_c of the crystals considered in figure 4.43.

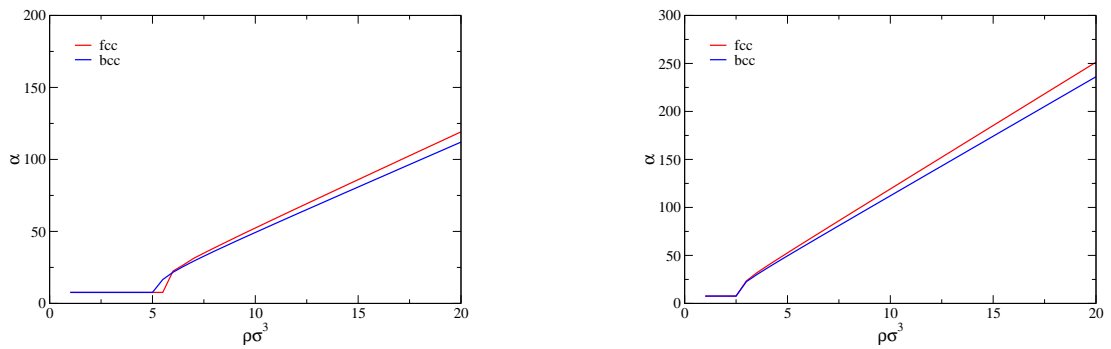


Figure 4.45: The localization parameter α of the crystals considered in figure 4.43.

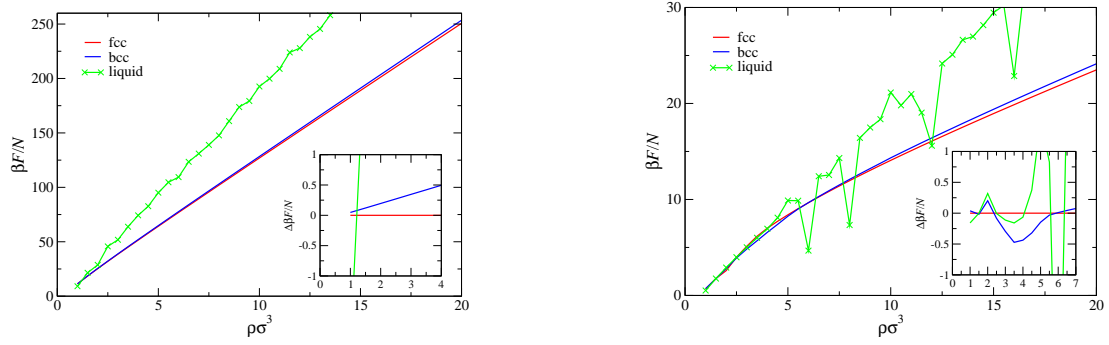


Figure 4.46: **left:** Free energy of a GGCM-system with $n = 4$ and $\varepsilon = 10$ calculated with DFT for the solid phases and the MSA closure for the liquid phase. **right:** The same for $n = 7$, $\varepsilon = 1$.

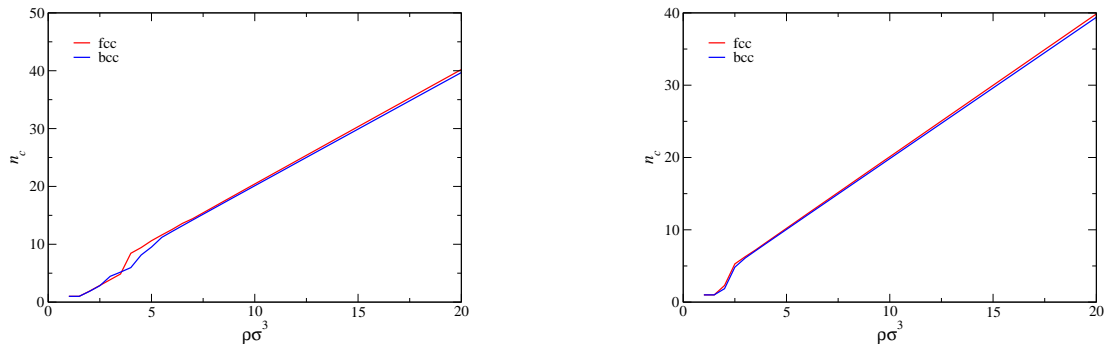


Figure 4.47: The cluster size n_c of the crystals considered in figure 4.46.

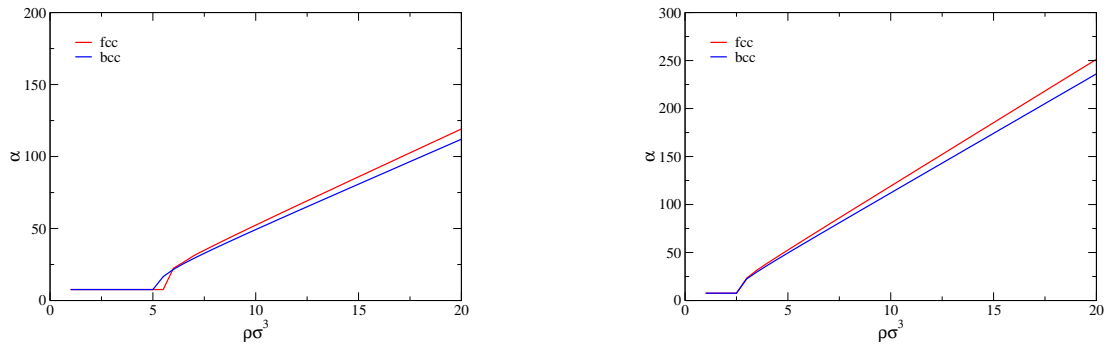


Figure 4.48: The localization parameter α of the crystals considered in figure 4.46.

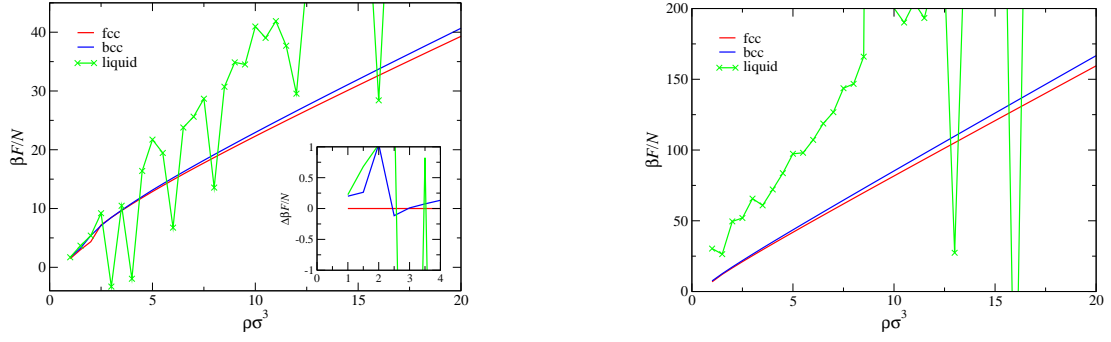


Figure 4.49: **left:** Free energy of a GGCM-system with $n = 7$ and $\varepsilon = 2$ calculated with DFT for the solid phases and the MSA closure for the liquid phase. **right:** The same for $\varepsilon = 10$.

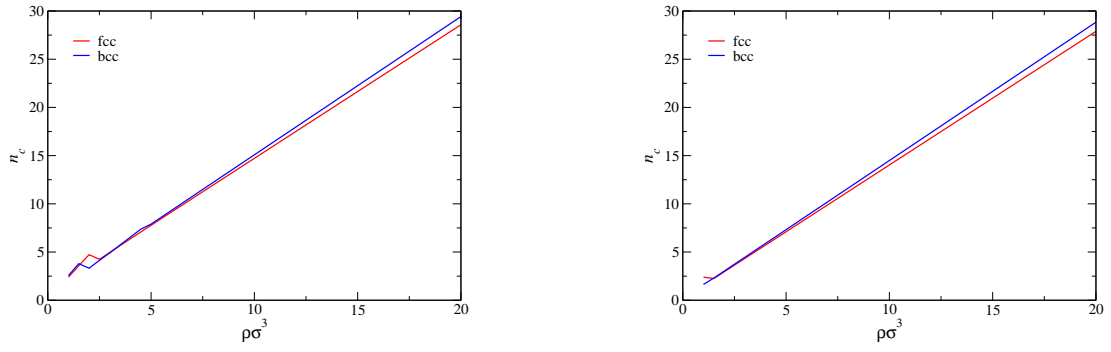


Figure 4.50: The cluster size n_c of the crystals considered in figure 4.49.

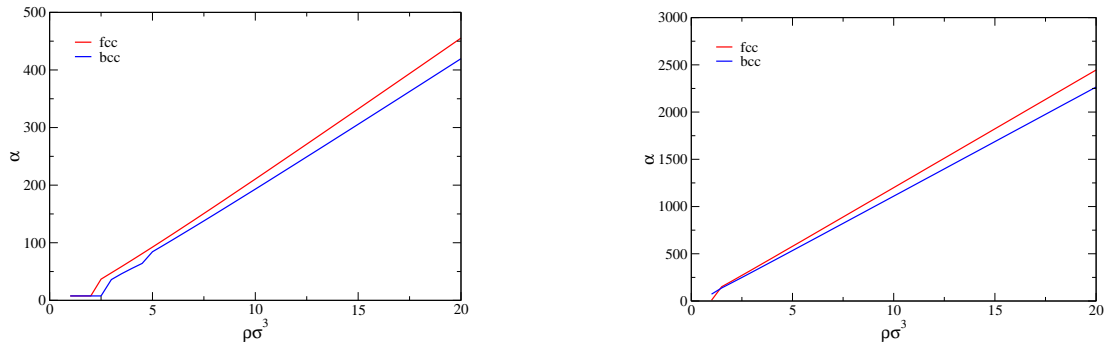


Figure 4.51: The localization parameter α of the crystals considered in figure 4.49.

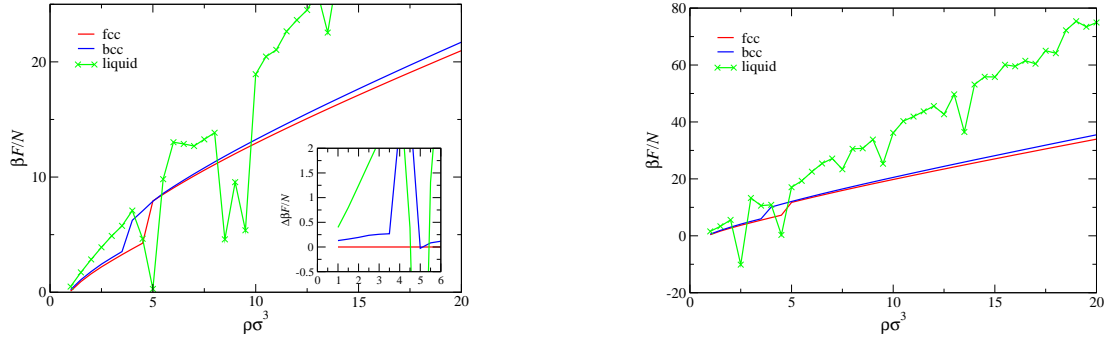


Figure 4.52: **left:** Free energy of a GGCM-system with $n = 10$ and $\varepsilon = 1$ calculated with DFT for the solid phases and the MSA closure for the liquid phase. **right:** The same for $\varepsilon = 2$.

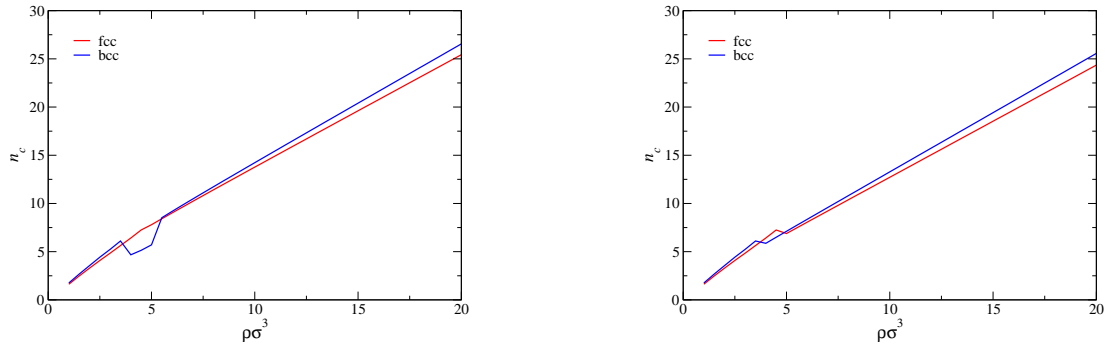


Figure 4.53: The cluster size n_c of the crystals considered in figure 4.52.

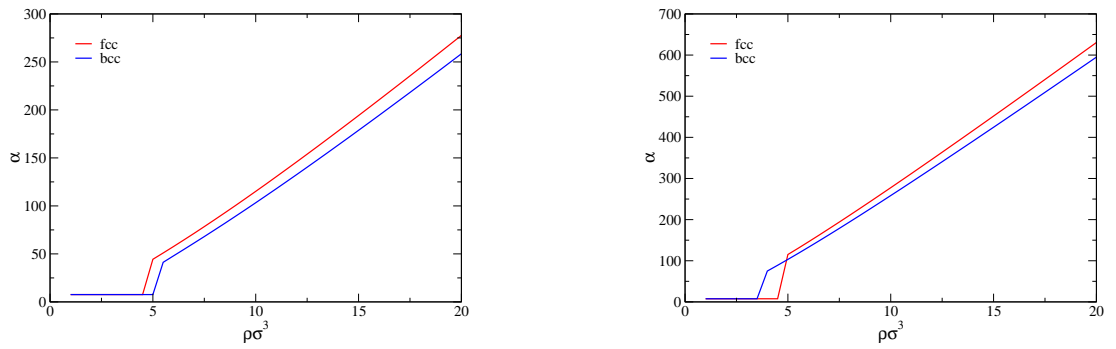


Figure 4.54: The localization parameter α of the crystals considered in figure 4.52.

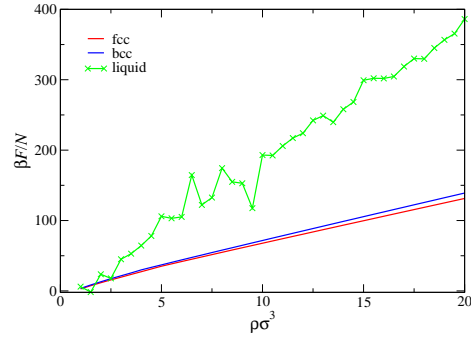


Figure 4.55: Free energy of a GGCM-system with $n = 10$ and $\varepsilon = 10$ calculated with DFT for the solid phases and the MSA closure for the liquid phase.

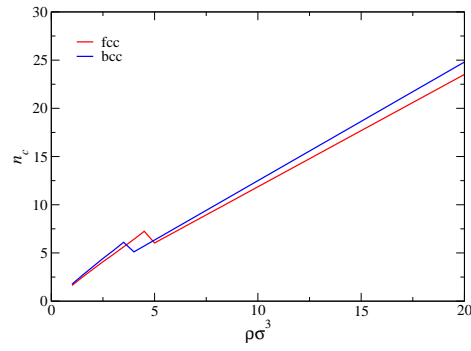


Figure 4.56: The cluster size n_c of the crystals considered in figure 4.55.

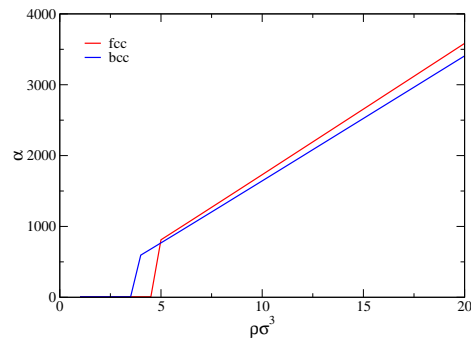


Figure 4.57: The localization parameter α of the crystals considered in figure 4.55.

The cluster size n_c and the localization parameter α seem to have a linear dependence on the density above the transition density. Therefore linear regression was applied to the data points. The slope of the line, k_{fcc} or k_{bcc} , that approximates the cluster size as a function of the density shows a very weak dependence on the pre-factor ε and a non-linear dependence on the index n (see figure 4.58), while the slope of the line that approximates the localization parameter shows a linear dependence both on the index n (see figure 4.59) and on ε (see figure 4.60).

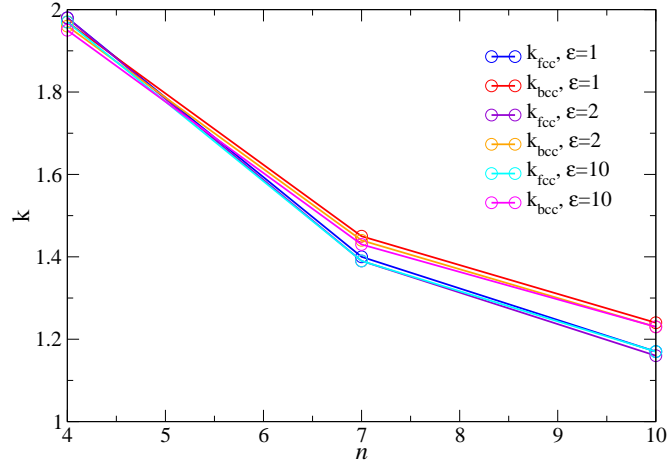


Figure 4.58: The slope k of a linear regression of the cluster size–density curve as a function of pre-factor ε .

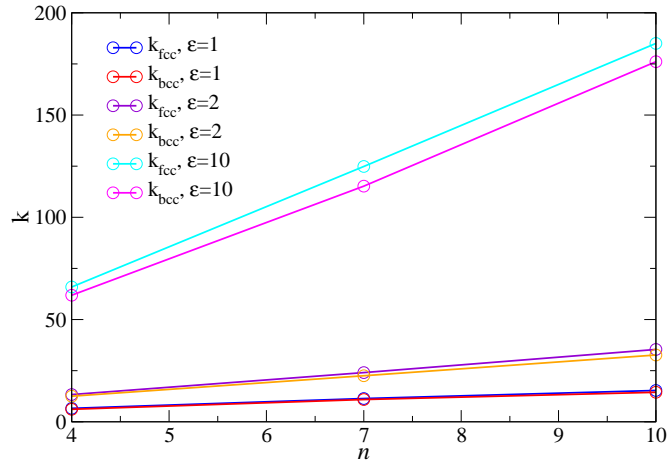


Figure 4.59: The slope k of a linear regression of the localization parameter–density curve as a function of pre-factor ε .

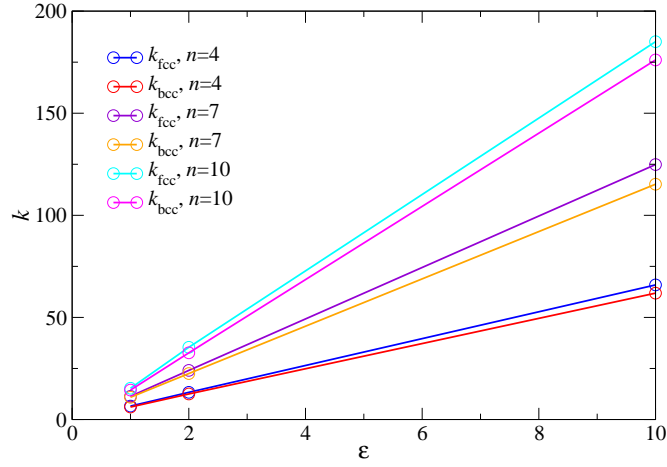


Figure 4.60: The slope k of a linear regression of the localization parameter–density curve as a function of index n .

Due to the erratic behavior of the MSA closure for densities beyond the estimated transition, the calculation of a full phase diagram was very hard to accomplish. Up to now it was successful for the index $n = 4$ (see figure 4.61). A more accurate and reliable description of the liquid phase will certainly lead to a wider range of parameters where a liquid-clustered crystal transition can be predicted.

The results obtained by this mean field density functional theory, such as cluster size, and the location of phase transitions, are in good agreement with simulations on a quantitative level [60].

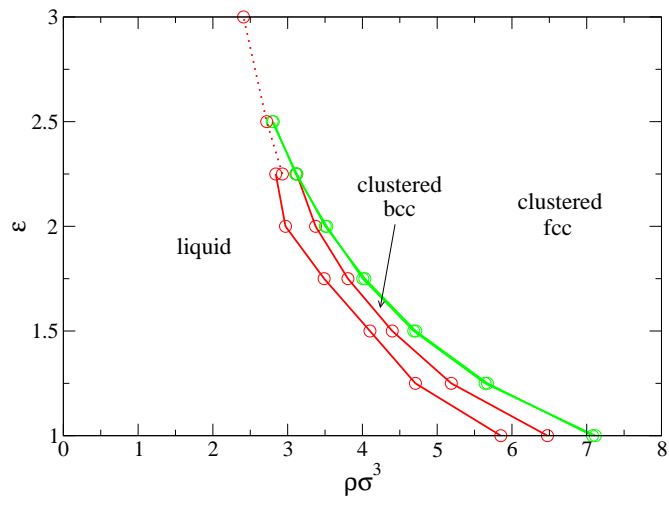


Figure 4.61: Phase diagram of a GGCM system with index $n = 4$ including the liquid phase and clustered bcc and fcc crystals. The solid lines denote the borders of the coexistence region and the dotted line denotes the point where the liquid and the solid free energy curves intersect. The calculation of a double tangent was not possible in this region.

Conclusions

In this work a new approach to predict equilibrium crystal structures in freezing transitions was introduced and applied to selected problems in soft condensed matter theory.

In this method the equilibrium crystal lattice was found via a genetic algorithm. According to the strategy of GAs, the crystal lattice was encoded in an individual in binary form. The individuals are evaluated via a fitness function that assigns a higher value to lattices with a lower free energy. Individuals with a higher fitness value propagate faster than ones with a lower fitness value. The results obtained in this way were refined with a subsequent hill climbing search algorithm to compensate the discrete representation induced by the binary representation of the individual.

This technique has demonstrated its power and versatility in a number of different problems. Considering different freezing transitions, it was possible to demonstrate that this procedure is indeed superior to the conventional approach to determine solid equilibrium structures in freezing processes, that relies on an a priori selection of possible candidate structures.

The first application was dedicated to a revision of the phase diagram of neutral star polymers that was already published in literature. Indeed the GA could find new equilibrium structures that had not been considered in the conventional approach. Secondly, the phase behavior of ionic microgels was investigated. The properties of the solid phase were calculated with the Einstein model and the localization parameter was successfully included in the individual where it was optimized together with the lattice parameters. Using the structures predicted in this way and calculating the properties of the liquid phase with integral equation theories, the full liquid-solid phase diagram was obtained. Crystal structures such as bcc, trigonal, and hexagonal lattices were found to be stable, that have been considered up to date as unusual for systems that interact via a radially symmetric pair potential. Two regions of re-entrant melting were discovered in the phase diagram, which has not been encountered before. The freezing criterion by Hansen and Verlet, as well as the melting criterion of Lindemann were able to predict the first re-entrant melting transition on a qualitative level but failed to predict the second transition which occurs at densities well above the overlap density.

However, close to the transitions between two phases the free energies and thus the fitness values of the competing phases become almost identical and due to the randomness involved in the genetic algorithm, both structures might be considered as the equilibrium structure. Therefore the exact location of the transition is impossible to compute with the GA but can be calculated separately using the structures predicted in the proximity of the transition as candidates. Furthermore, problems arose when crystal structures with a high number of basis particles (typically eight and more) were considered. With the help of a modified fitness function, convergence could be achieved for lattices with eight basis particles.

The results for systems that consist of parallel layers of two-dimensional lattices showed the same sequence of structures for increasing distance between the top and bottom layer as experiments and simulations but unfortunately the model that was used was too simple to allow a quantitative comparison. A more realistic model and an improved parametrization of the lattices should be able to remedy this shortcoming.

A system that interacts via a generalized Gaussian core model was also studied. For this system a clustering transition was predicted upon compression, where clusters of particles are formed that sit nearly on top of each other. These clusters form regular lattices, such as fcc or bcc. It was possible to confirm the predicted linear dependence of the cluster size on the density and to calculate a phase diagram that includes the liquid phase and two crystalline clustered phases. The theoretical calculations were in good agreement with data from Monte Carlo simulations.

Based on the experience gained, the GA could certainly be applied to a number of other problems in condensed matter theory, such as:

- Calculations with more sophisticated theories for the solid phase, ranging from density functional theory to ab initio calculations.
- Phase transitions under extreme conditions that are not accessible to experiments.
- The formation of clusters and the arrangement of particles in the clusters.
- Phase behavior of soft matter.

Appendix A

Three-Dimensional Bravais Lattices and Crystal Structures

A three-dimensional lattice is defined by three primitive vectors $\mathbf{a}, \mathbf{b}, \mathbf{c}$ that create all points of the lattice $\{\mathbf{R}_n\}$ via

$$\{\mathbf{R}_n\} = i\mathbf{a} + j\mathbf{b} + k\mathbf{c} \quad i, j, k \in \mathbb{Z}.$$

Depending on the symmetry transformations that transform the lattice into itself one can discern seven crystal systems. An axis is called n -fold symmetry axis, if a rotation by angle $\phi = 2\pi/n$ around the axis transforms the lattice into itself. The seven three-dimensional crystal systems have different symmetry transformations:

	2-fold axes	3-fold axes	4-fold axes	6-fold axes	Σ	Ev-
cubic	9	4	3	0	16	
hexagonal	7	1	0	1	9	
tetragonal	5	0	1	0	6	
trigonal	3	1	0	0	4	
orthorhombic	3	0	0	0	3	
monoclinic	1	0	0	0	1	
triclinic	0	0	0	0	0	

every Bravais lattice belongs exactly to one crystal system but since these symmetry properties can be fulfilled by more than one lattice there are fourteen three-dimensional Bravais lattices.

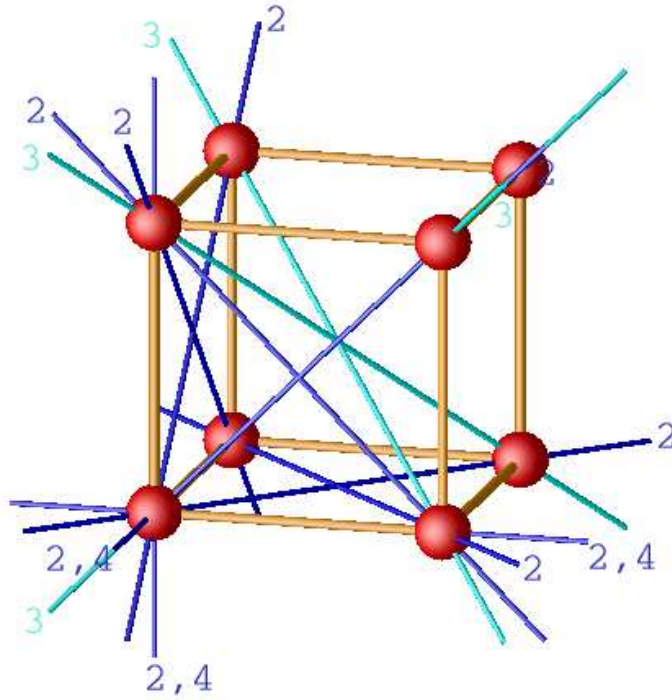


Figure A.1: *Cubic conventional cell and its symmetry axes*

A.1 Cubic Lattices

Simple Cubic (sc)

Primitive vectors of the lattice:

$$\mathbf{a} = \begin{pmatrix} a \\ 0 \\ 0 \end{pmatrix} \quad \mathbf{b} = \begin{pmatrix} 0 \\ a \\ 0 \end{pmatrix} \quad \mathbf{c} = \begin{pmatrix} 0 \\ 0 \\ a \end{pmatrix}$$

Volume of the unit cell:

$$V_c = a^3$$

Body-Centered Cubic (bcc)

Primitive vectors of the lattice:

$$\mathbf{a} = \begin{pmatrix} a \\ 0 \\ 0 \end{pmatrix} \quad \mathbf{b} = \begin{pmatrix} 0 \\ a \\ 0 \end{pmatrix} \quad \mathbf{c} = \begin{pmatrix} a/2 \\ a/2 \\ a/2 \end{pmatrix}$$

Volume of the unit cell:

$$V_c = \frac{1}{2}a^3$$

Face-Centered Cubic (fcc)

Primitive vectors of the lattice:

$$\mathbf{a} = \begin{pmatrix} a \\ 0 \\ 0 \end{pmatrix} \quad \mathbf{b} = \begin{pmatrix} a/2 \\ a/2 \\ 0 \end{pmatrix} \quad \mathbf{c} = \begin{pmatrix} a/2 \\ 0 \\ a/2 \end{pmatrix}$$

Volume of the unit cell:

$$V_c = \frac{1}{4}a^3$$

A.2 Hexagonal Lattice

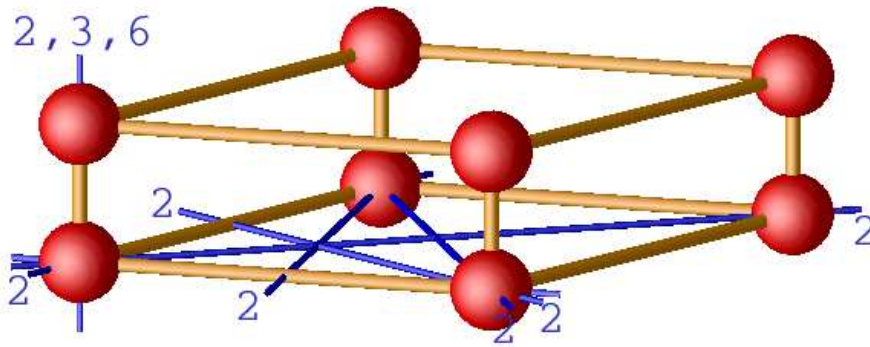


Figure A.2: *Hexagonal conventional cell and its symmetry axes*

Simple Hexagonal (hex)

Primitive vectors of the lattice:

$$\mathbf{a} = \begin{pmatrix} a \\ 0 \\ 0 \end{pmatrix} \quad \mathbf{b} = \begin{pmatrix} a/2 \\ \sqrt{3}a/2 \\ 0 \end{pmatrix} \quad \mathbf{c} = \begin{pmatrix} 0 \\ 0 \\ c \end{pmatrix}$$

Volume of the unit cell:

$$V_c = \frac{\sqrt{3}}{2}a^2c$$

A.3 Tetragonal Lattices

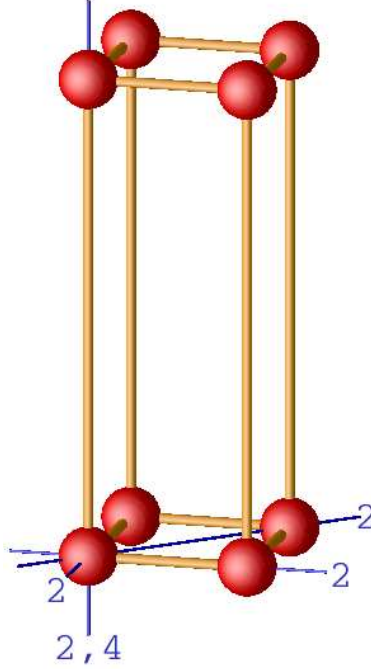


Figure A.3: *Tetragonal conventional cell and its symmetry axes*

Simple Tetragonal

Primitive vectors of the lattice:

$$\mathbf{a} = \begin{pmatrix} a \\ 0 \\ 0 \end{pmatrix} \quad \mathbf{b} = \begin{pmatrix} 0 \\ a \\ 0 \end{pmatrix} \quad \mathbf{c} = \begin{pmatrix} 0 \\ 0 \\ c \end{pmatrix}$$

Volume of the unit cell:

$$V_c = a^2 c$$

Body-Centered Tetragonal

Primitive vectors of the lattice:

$$\mathbf{a} = \begin{pmatrix} a \\ 0 \\ 0 \end{pmatrix} \quad \mathbf{b} = \begin{pmatrix} 0 \\ a \\ 0 \end{pmatrix} \quad \mathbf{c} = \begin{pmatrix} a/2 \\ a/2 \\ c/2 \end{pmatrix}$$

Volume of the unit cell:

$$V_c = \frac{1}{2}a^2c$$

A.4 Trigonal Lattice

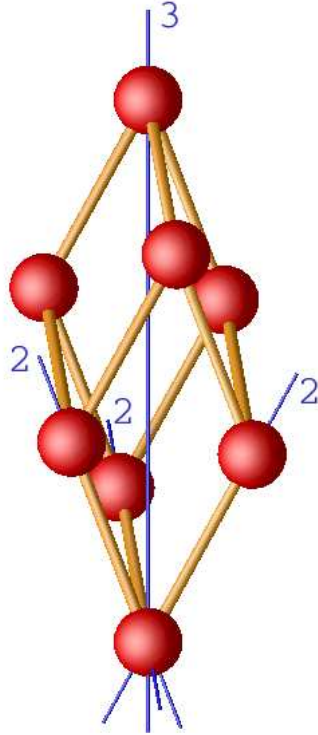


Figure A.4: *Trigonal conventional cell and its symmetry axes*

Simple Trigonal (trig)

Primitive vectors of the lattice:

$$\mathbf{a} = \begin{pmatrix} a/\sqrt{12} \\ -a/2 \\ c/3 \end{pmatrix} \quad \mathbf{b} = \begin{pmatrix} a/\sqrt{12} \\ a/2 \\ c/3 \end{pmatrix} \quad \mathbf{c} = \begin{pmatrix} -a/\sqrt{3} \\ 0 \\ c/3 \end{pmatrix}$$

Volume of the unit cell:

$$V_c = \frac{1}{\sqrt{12}}a^2c$$

A trigonal lattice with $c/a = \sqrt{6}$ is a fcc-lattice; with $c/a = \sqrt{3/8}$ it is a bcc-lattice.

A.5 Orthorhombic Lattices

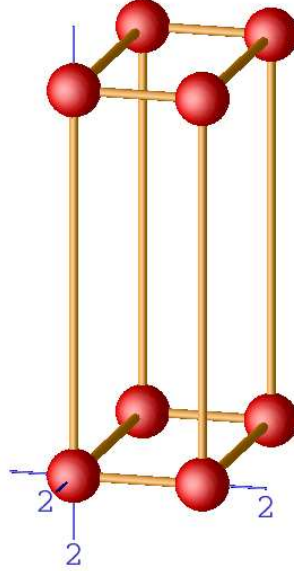


Figure A.5: *Orthorhombic conventional cell and its symmetry axes*

Simple Orthorhombic

Primitive vectors of the lattice:

$$\mathbf{a} = \begin{pmatrix} a \\ 0 \\ 0 \end{pmatrix} \quad \mathbf{b} = \begin{pmatrix} 0 \\ b \\ 0 \end{pmatrix} \quad \mathbf{c} = \begin{pmatrix} 0 \\ 0 \\ c \end{pmatrix}$$

Volume of the unit cell:

$$V_c = abc$$

Single-Face-Centered Orthorhombic

Primitive vectors of the lattice:

$$\mathbf{a} = \begin{pmatrix} a \\ 0 \\ 0 \end{pmatrix} \quad \mathbf{b} = \begin{pmatrix} a/2 \\ b/2 \\ 0 \end{pmatrix} \quad \mathbf{c} = \begin{pmatrix} 0 \\ 0 \\ c \end{pmatrix}$$

Volume of the unit cell:

$$V_c = \frac{1}{2}abc$$

Body-Centered Orthorhombic (bco)

Primitive vectors of the lattice:

$$\mathbf{a} = \begin{pmatrix} a \\ 0 \\ 0 \end{pmatrix} \quad \mathbf{b} = \begin{pmatrix} 0 \\ b \\ 0 \end{pmatrix} \quad \mathbf{c} = \begin{pmatrix} a/2 \\ b/2 \\ c/2 \end{pmatrix}$$

Volume of the unit cell:

$$V_c = \frac{1}{2}abc$$

A bco-lattice with $c/a = b/a = 1$ is a bcc-lattice; with $c/a = b/a = 1/\sqrt{2}$ is a fcc-lattice and with $c/a = \sqrt{3}/2$ is a sc-lattice.

Face-Centered Orthorhombic

Primitive vectors of the lattice:

$$\mathbf{a} = \begin{pmatrix} a \\ 0 \\ 0 \end{pmatrix} \quad \mathbf{b} = \begin{pmatrix} a/2 \\ b/2 \\ 0 \end{pmatrix} \quad \mathbf{c} = \begin{pmatrix} a/2 \\ 0 \\ c/2 \end{pmatrix}$$

Volume of the unit cell:

$$V_c = \frac{1}{4}abc$$

A.6 Monoclinic Lattices

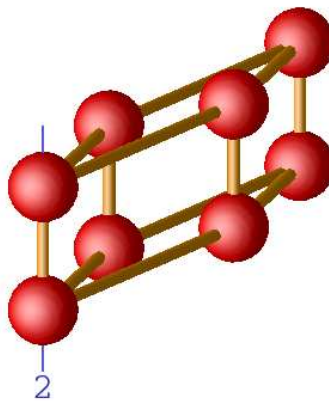


Figure A.6: *Monoclinic conventional cell and its symmetry axes*

Simple Monoclinic

Primitive vectors of the lattice:

$$\mathbf{a} = \begin{pmatrix} a \sin \gamma \\ a \cos \gamma \\ 0 \end{pmatrix} \quad \mathbf{b} = \begin{pmatrix} 0 \\ b \\ 0 \end{pmatrix} \quad \mathbf{c} = \begin{pmatrix} 0 \\ 0 \\ c \end{pmatrix}$$

Volume of the unit cell:

$$V_c = abc \sin \gamma$$

Single-Face-Centered Monoclinic

Primitive vectors of the lattice:

$$\mathbf{a} = \begin{pmatrix} (a \sin \gamma)/2 \\ (a \cos \gamma)/2 \\ -c/2 \end{pmatrix} \quad \mathbf{b} = \begin{pmatrix} 0 \\ b \\ 0 \end{pmatrix} \quad \mathbf{c} = \begin{pmatrix} (a \sin \gamma)/2 \\ (a \cos \gamma)/2 \\ c/2 \end{pmatrix}$$

Volume of the unit cell:

$$V_c = \frac{1}{2} abc \sin \gamma$$

A.7 Triclinic Lattice

Triclinic

Primitive vectors of the lattice:

$$\mathbf{a} = \begin{pmatrix} a \\ 0 \\ 0 \end{pmatrix} \quad \mathbf{b} = \begin{pmatrix} b \sin \alpha \\ b \cos \alpha \\ 0 \end{pmatrix} \quad \mathbf{c} = \begin{pmatrix} c \cos \beta \cos \gamma \\ c \cos \beta \sin \gamma \\ c \sin \beta \end{pmatrix}$$

Volume of the unit cell:

$$V_c = abc \cos \alpha \sin \beta$$

A.8 Diamond Structure

The diamond structure is built up by a fcc-lattice with the basis vectors:

$$\mathbf{b}_1 = \begin{pmatrix} 0 \\ 0 \\ 0 \end{pmatrix} \quad \mathbf{b}_2 = \begin{pmatrix} a/4 \\ a/4 \\ a/4 \end{pmatrix}$$

A.9 Hexagonal Close Packed

The hexagonal close packed structure (hcp) is built up by a simple hexagonal lattice with the basis vectors:

$$\mathbf{b}_1 = \begin{pmatrix} 0 \\ 0 \\ 0 \end{pmatrix} \quad \mathbf{b}_2 = \begin{pmatrix} a/2 \\ a/\sqrt{12} \\ c/2 \end{pmatrix}$$

A.10 A15-Structure

The A15 structure is built up by a sc-lattice with the basis vectors:

$$\begin{aligned} \mathbf{b}_1 &= \begin{pmatrix} 0 \\ 0 \\ 0 \end{pmatrix} \quad \mathbf{b}_2 = \begin{pmatrix} a/2 \\ a/2 \\ a/2 \end{pmatrix} \quad \mathbf{b}_3 = \begin{pmatrix} a/2 \\ 0 \\ a/4 \end{pmatrix} \quad \mathbf{b}_4 = \begin{pmatrix} a/2 \\ 0 \\ 3a/4 \end{pmatrix} \\ \mathbf{b}_5 &= \begin{pmatrix} a/4 \\ a/2 \\ 0 \end{pmatrix} \quad \mathbf{b}_6 = \begin{pmatrix} 3a/4 \\ a/2 \\ 0 \end{pmatrix} \quad \mathbf{b}_7 = \begin{pmatrix} 0 \\ a/4 \\ a/2 \end{pmatrix} \quad \mathbf{b}_8 = \begin{pmatrix} 0 \\ 3a/4 \\ a/2 \end{pmatrix} \end{aligned}$$

Appendix B

Two-Dimensional Bravais Lattices

Similar to the three-dimensional case there are four two-dimensional crystal systems and five two-dimensional Bravais lattices.

B.1 Hexagonal Lattice

The hexagonal lattice has a 6-fold rotation axis. Primitive vectors of the lattice:

$$\mathbf{a} = \begin{pmatrix} a \\ 0 \end{pmatrix} \quad \mathbf{b} = \begin{pmatrix} a/2 \\ \sqrt{3}a/2 \end{pmatrix}$$

Area of the unit cell:

$$A_c = \frac{\sqrt{3}a^2}{2}$$

B.2 Square Lattice

The square lattice has a 4-fold rotation axis. Primitive vectors of the lattice:

$$\mathbf{a} = \begin{pmatrix} a \\ 0 \end{pmatrix} \quad \mathbf{b} = \begin{pmatrix} 0 \\ a \end{pmatrix}$$

Area of the unit cell:

$$A_c = a^2$$

B.3 Rectangular Lattices

The rectangular lattice has two perpendicular mirror planes.

Rectangular

Primitive vectors of the lattice:

$$\mathbf{a} = \begin{pmatrix} a \\ 0 \end{pmatrix} \quad \mathbf{b} = \begin{pmatrix} 0 \\ b \end{pmatrix}$$

Area of the unit cell:

$$A_c = ab$$

Centered Rectangular (Rhombic)

Primitive vectors of the lattice:

$$\mathbf{a} = \begin{pmatrix} a \\ 0 \end{pmatrix} \quad \mathbf{b} = \begin{pmatrix} a/2 \\ b/2 \end{pmatrix}$$

Area of the unit cell:

$$A_c = \frac{ab}{2}$$

B.4 Oblique Lattice

The oblique lattice has no symmetry axes or mirror planes. Primitive vectors of the lattice:

$$\mathbf{a} = \begin{pmatrix} a \\ 0 \end{pmatrix} \quad \mathbf{b} = \begin{pmatrix} b \cos \gamma \\ b \sin \gamma \end{pmatrix}$$

Area of the unit cell:

$$A_c = ab \sin \gamma$$

Appendix C

Lattice Identification

To identify the type of lattice, the crystal system to which the primitive vectors \mathbf{a} , \mathbf{b} , and \mathbf{c} belong has to be calculated first; then the Bravais lattice can be determined.

Each crystal system has a unique number of symmetry axes (see appendix A). An n -fold symmetry can be described by a rotation matrix A which is given by

$$A = \cos \phi \begin{pmatrix} 1 & 0 & 0 \\ 0 & 1 & 0 \\ 0 & 0 & 1 \end{pmatrix} + (1 - \cos \phi) \begin{pmatrix} e_x e_x & e_x e_y & e_x e_z \\ e_y e_x & e_y e_y & e_y e_z \\ e_z e_x & e_z e_y & e_z e_z \end{pmatrix} + \sin \phi \begin{pmatrix} 0 & -e_z & e_y \\ e_z & 0 & -e_x \\ -e_y & e_x & 0 \end{pmatrix},$$

where the unit vector \mathbf{e} is parallel to the rotation axis. If the lattice is transformed into itself upon a rotation then the solutions of the equations

$$\begin{aligned} x_a(A\mathbf{a}) + y_a(A\mathbf{b}) + z_a(A\mathbf{c}) &= \mathbf{a} \\ x_b(A\mathbf{a}) + y_b(A\mathbf{b}) + z_b(A\mathbf{c}) &= \mathbf{b} \\ x_c(A\mathbf{a}) + y_c(A\mathbf{b}) + z_c(A\mathbf{c}) &= \mathbf{c} \end{aligned} \tag{C.1}$$

are integer numbers. In a crystal the direction vector \mathbf{e} that describes such a symmetry axis is always parallel to $i\mathbf{a} + j\mathbf{b} + k\mathbf{c}$, $i, j, k \in \mathbb{Z}$. The algorithm to calculate the symmetry axes thus works as follows:

1. Calculate all vectors $\mathbf{v}_{ijk} = i\mathbf{a} + j\mathbf{b} + k\mathbf{c}$ with $v_{ijk} \leq |\mathbf{a} + \mathbf{b} + \mathbf{c}|$, $i, j, k \in \mathbb{Z}$.
2. Create all unit vectors $\mathbf{e}_l \parallel \mathbf{v}_{ijk}$ that are not collinear and save the shortest vector \mathbf{v}_{ijk} that is parallel to \mathbf{e}_l as $\tilde{\mathbf{v}}_{ijk,l}$.
3. Solve the equations (C.1) for all \mathbf{e}_l and $\phi = 2\pi/n$, $n = 2, 3, 4, 6$.
4. Calculate

$$\Delta = 16 \sum_{\xi \in \{a,b,c\}} (\tilde{x}_\xi^2 (x_\xi - 1)^2 + \tilde{y}_\xi^2 (y_\xi - 1)^2 + \tilde{z}_\xi^2 (z_\xi - 1)^2)$$

for all solutions, where $\bar{x} = x - [x]$ and $[x]$ denotes the largest integer smaller or equal x . The value of Δ is zero if all solutions are integers and is a maximum if all solutions can be written as $n + 1/2$, $n \in \mathbb{Z}$. Usually the primitive vectors that were obtained by the GA and the subsequent hill climbing have errors therefore the condition $\Delta < \epsilon$ is used to determine whether the combination (\mathbf{e}_l, n) describes a symmetry axis. The parameter $\epsilon \sim 1 \times 10^{-4}$ is a fixed but small value.

5. Count the number of symmetry axes. This value determines the crystal system.

Most of the parameters of the lattice can be calculated from the vectors $\tilde{\mathbf{v}}_{ijk,l}$. The length of the vector $\tilde{\mathbf{v}}_{ijk,l}$ that is parallel to a unit vector, which describes a n -, m -, and o -fold symmetry axis is denoted by $l_{n,m,o}$.

- Cubic: $a = l_{2,4}$.
- Hexagonal: $c = l_{2,3,6}$; $a = \min\{l_2\}$.
- Tetragonal: $c = l_{2,4}$; $a = \min\{l_2\}$.
- Trigonal: $c = l_3$; $a = l_2$.
- Orthorhombic: $a = l_2^{(1)}$; $b = l_2^{(2)}$; $c = l_2^{(3)}$.
- Monoclinic: $c = l_2$. The other parameters a , b , and γ can be obtained by creating the two-dimensional sub-lattice perpendicular to the symmetry axis, finding the shortest vectors that act as primitive vectors for this sub-lattice, and calculating their length and angle.

After the crystal system is known the Bravais lattice has to be determined for those crystal systems that have more than one corresponding Bravais lattice. In most cases it can be evaluated by a relation between the lattice parameters a , b , c , γ and the volume of the cell spanned by the primitive vectors, which is denoted by $V_{abc} = \mathbf{a} \cdot (\mathbf{b} \times \mathbf{c})$.

- Cubic: The ratio V_{abc}/a^3 determines the Bravais lattice. It is 1 for a simple cubic lattice, 1/2 for a bcc-lattice, and 1/4 for a fcc-lattice.
- Tetragonal: The ratio $V_{abc}/(a^2c)$ is 1 for a simple tetragonal lattice, and 1/2 for a body-centered tetragonal lattice.
- Orthorhombic: For a simple orthorhombic lattice the ratio $V_{abc}/(abc)$ is 1 and 1/4 for a face-centered orthorhombic lattice. A ratio of 1/2 points to both body-centered and single face-centered orthorhombic accordingly in this case the equation

$$x_a \mathbf{a} + x_b \mathbf{b} + x_c \mathbf{c} = \frac{a}{2} \tilde{\mathbf{v}}_{ijk,2}^{(1)} + \frac{b}{2} \tilde{\mathbf{v}}_{ijk,2}^{(2)} + \frac{c}{2} \tilde{\mathbf{v}}_{ijk,2}^{(3)}$$

is solved for x_a , x_b , and x_c . If the solutions are integers, then the primitive vectors form a body-centered orthorhombic lattice. If not, they form a single face-centered orthorhombic lattice.

- Monoclinic: A ratio $V_{abc}/(abc \sin \gamma)$ of 1 refers to a simple monoclinic lattice, one of $1/2$ to a single face-centered monoclinic lattice.

Acknowledgments

During the time I worked on this thesis I was supported by a number of people. Without their help this work could not have been done:

- My supervisor Gerhard Kahl for his support and for having faith in my ideas.
- Christos “Herr Wolf” Likos from Düsseldorf for introducing me to the fantastic field of soft matter and for his invaluable help with numerous problems.
- Hartmut Löwen from Düsseldorf for the hospitality during my stay at the Heinrich-Heine Universität Düsseldorf, where parts of this work were completed.
- Rainer Dirl for the helpful discussions about crystal lattices.
- Bianca Mladek for the help with everything that runs under Windows, the cooking sessions and the company in Düsseldorf, and for bringing fun to everyday routine.
- Marie-José Fernaund for listening to my gibberish and for encouragement in times of need.
- Jürgen Köfinger for the hilarious discussions about movies and physics.
- Gernot Pauschenwein for creating a comfortable working atmosphere.
- Sonja Mentl for proof reading.
- Iris Brandstetter for giving me the emotional strength to endure these three years.

Bibliography

- [1] B.J. Alder and T.E. Wainwright, J. Chem. Phys. **27**, 1208 (1957).
- [2] W.W. Wood and J.D. Jacobson, J. Chem. Phys. **27**, 1207 (1957).
- [3] C.N. Likos, N. Hoffmann, H. Löwen, and A.A. Louis, J. Phys.: Condens. Matter **14**, 7681 (2002).
- [4] J.G. Kirkwood, J. Chem. Phys. **18**, 380 (1950).
- [5] W.W. Wood, J. Chem. Phys. **20**, 1334 (1952).
- [6] A. Bonissent, P. Pieranski, and P. Pieranski, Philos. Mag. A **50**, 57 (1984).
- [7] K.W. Wojciechowski, Phys. Rev. A **122**, 377 (1987).
- [8] C.F. Tejero, A. Daanoun, H.N.W. Lekkerkerker, and M. Baus, Phys. Rev. E **51**, 558 (1995).
- [9] H.R. Glyde and G.H. Keech, Ann. Phys. **127**, 330 (1980).
- [10] D. Oxtoby, in *Les Houches, Session LI, Liquids, Freezing and Glass Transition*, edited by J.-P. Hansen, D. Levesque, and J. Zinn-Justin (North-Holland, Amsterdam, 1991).
- [11] Y. Singh, Phys. Rep. **207**, 351 (1991).
- [12] A.D.J. Haymet, in *Fundamentals of Inhomogeneous Liquids*, edited by D. Henderson (Marcel-Dekker, New York, 1992).
- [13] H. Löwen, Phys. Rep. **237**, 249 (1994).
- [14] M. Schmidt, J. Phys.: Condens. Matter **15**, 101 (2003).
- [15] J.P. Hansen and I.R. McDonald, *Theory of Simple Liquids*, 2nd ed. (Academic Press, London, 1986).
- [16] C.N. Likos, Phys. Rep. **348**, 267 (2001).
- [17] M. Watzlawek, C.N. Likos, and H. Löwen, Phys. Rev. Lett. **82**, 5289 (1999).

- [18] J.H. Holland, *Adaption in Natural and Artificial Systems* (The University of Michigan Press, Ann Arbor, 1975).
- [19] D.E. Goldberg, *Genetic Algorithms in Search, Optimization and Machine Learning* (Addison-Wesley, MA, 1989).
- [20] Z. Michalewicz, *Genetic Algorithms + Data Structures = Evolution Programs* (Springer, New York, 1992).
- [21] D.H. Deaven and K.M. Ho, Phys. Rev. Lett. **75**, 288 (1995).
- [22] S. Darby, T.M. Mortimer-Jones, R.L. Johnston, and C. Roberts, J. Chem. Phys. **116**, 1536 (2002).
- [23] R.S Judson and H. Rabitz, Phys. Rev. Lett. **68**, 1500 (1992).
- [24] R.B. Hunter, *Foundations of Colloid Science* (Clarendon Press, Oxford, 1986).
- [25] S.A. Safran and N.A. Clark, *Physics of Complex and Supramolecular Fluids* (Wiley Interscience, New York, 1987).
- [26] W.B. Russel, D.A. Saville, and W.R. Schowalter, *Colloidal Dispersions* (Cambridge University Press, Cambridge, 1989).
- [27] Special Issue: *Colloidal Dispersion in External Fields*, J. Phys.: Condens. Matter, 2004, **16** , No. 38, 3769-4242.
- [28] N. Hoffmann, C.N. Likos, and H. Löwen, J. Chem. Phys. **121**, 7009 (2004).
- [29] M. Watzlawek, *Phase Behavior of Star Polymers* (Shaker, Aachen, 2000).
- [30] D. Gottwald, C.N. Likos, G. Kahl, and H. Löwen, Phys. Rev. Lett. **92**, 068301 (2004), selected for publication in the Virtual Journal of Nanoscale Science and Technology, issue of 23 February, 2004.
- [31] D. Gottwald, C.N. Likos, G. Kahl, and H. Löwen, J. Chem. Phys. **122**, 074903 (2005).
- [32] C. Darwin, *The Origin of Species by Means of Natural Selection* (John Murray, Albemarle Street, London, 1859).
- [33] H.-P. Schwefel, *Evolution and Optimum Seeking* (John Wiley, New York, 1995).
- [34] S. Kirkpatrick, C.D. Gelatt, and M.P. Vecchi, Science **220**, 671 (1983).
- [35] V. Černý, JOTA **45**, 41 (1985).

- [36] *Genetic algorithms and simulated annealing*, edited by L. Davis (Pitman, London, 1987).
- [37] A.J. Archer, Ph.D. thesis, University of Bristol, 2004, (unpublished).
- [38] F.A. Rogers and D.A. Young, Phys. Rev. A **30**, 999 (1984).
- [39] A.A. Broyles, J. Chem. Phys. **33**, 456 (1960).
- [40] C.F. Tejero and M. Baus, J. Chem. Phys. **118**, 892 (2003).
- [41] B.R. Saunders and B. Vincent, Adv. Colloid Interface Sci. **80**, 1 (1999).
- [42] T. Eckert and E. Bartsch, Phys. Rev. Lett. **89**, 125701 (2002).
- [43] H. Senff and W. Richtering, J. Chem. Phys. **111**, 1705 (1999).
- [44] A.R. Denton, Phys. Rev. E **67**, 011804 (2003); **68**, 049904(E) (2003).
- [45] P.J. Flory, *Principles of Polymer Chemistry* (Cornell University Press, Ithaca, 1953).
- [46] C.N. Likos, H. Löwen, M. Watzlawek, B. Abbas, O. Jucknischke, J. Allgaier, and D. Richter, Phys. Rev. Lett. **80**, 4450 (1998).
- [47] A. Jusufi, M. Watzlawek, and H. Löwen, Macromolecules **32**, 4470 (1999).
- [48] P.J. Flory and W.R. Krigbaum, J. Chem. Phys. **18**, 1086 (1950).
- [49] A. Lang, C.N. Likos, M. Watzlawek, and H. Löwen, J. Phys.: Condens. Matter **12**, 5087 (2000).
- [50] A.A. Louis, P.G. Bolhuis, and J.P. Hansen, Phys. Rev. E **62**, 7961 (2000).
- [51] B.M. Mladek, M.J. Feraud, G. Kahl, and M. Neumann, Condens. Matter Phys. **8**, 135 (2005).
- [52] J.-P. Hansen and L. Verlet, Phys. Rev. **184**, 151 (1969).
- [53] F.A. Lindemann, Phys. Z. **11**, 609 (1910).
- [54] P. Pieranski, L. Strzelecki, and B. Pansu, Phys. Rev. Lett. **50**, 900 (1983).
- [55] M. Schmidt and H. Löwen, Phys. Rev. Lett. **76**, 4552 (1996).
- [56] M. Schmidt and H. Löwen, Phys. Rev. E **55**, 7228 (1997).
- [57] S. Naser, C. Bechinger, P. Leiderer, and T. Palberg, Phys. Rev. Lett. **79**, 2348 (1997).

- [58] C.N. Likos, A. Lang, M. Watzlawek, and H. Löwen, Phys. Rev. E **63**, 31206 (2001).
- [59] B.M. Mladek, Diploma thesis, Universität Wien, 2003, (unpublished).
- [60] B.M. Mladek, D. Gottwald, G. Kahl, C.N. Likos, G. Kahl, and M. Neumann, (to be published).

Curriculum Vitae

Name: Dieter Gottwald

Birth Date: June 2nd, 1975

Birth Place: Vienna, Austria

Citizenship: Austria

Address: Murlingengasse 17/418, 1120 Wien

1981 - 1985	Volkschule Einsiedlergasse, Vienna
1985 - 1993	Bundesrealgymnasium V, Reinprechtsdorferstraße, Vienna
10/1993 - 06/2001	Studies of Technical Physics at the Vienna University of Technology
06/2001 - 05/2002	Alternative civilian service at MA 47
06/2002 - 06/2005	PhD in Technical Physics at the Vienna University of Technology